Towards Quantum Gas Microscopy of Ultracold Molecules

MORTLOCK, JONATHAN,MAXWELL

Towards Quantum Gas Microscopy of Ultracold Molecules

Jonathan M. Mortlock

A thesis submitted in partial fulfilment
of the requirements for the degree of
Doctor of Philosophy

Department of Physics
Durham University

2024

Towards Quantum Gas Microscopy of Ultracold Molecules

Jonathan M. Mortlock

Abstract

Ultracold atoms in optical lattices allow the study of large ensembles of strongly interacting quantum particles in an isolated environment. They are widely used as analogue quantum simulators to study phenomena from many areas of physics in a setting with high tunability and versatile detection methods. Many experiments now detect and control the atoms with single-site resolution in what are known as quantum gas microscopes. By extending these techniques to ultracold molecules it will be possible to extend the range of interparticle interactions and increase the diversity of types of quantum systems which can be studied in optical lattices.

This thesis reports on the construction of a new apparatus which is designed to realise a quantum gas microscope for ultracold ^{87}Rb^{133}Cs molecules. The apparatus consists of two trapping regions to provide sufficient optical access for the high numerical aperture lens and three-dimensional optical lattice required for quantum gas microscopy. By using degenerate Raman sideband cooling and fast moving-lattice optical transport followed by evaporation in an optical dipole trap we are able to cool both species to quantum degeneracy while maintaining a relatively fast repetition rate.

Using a three-dimensional optical lattice we observe the superfluid to Mott insulator transition in ^{133}Cs, demonstrating the ability to reach the strongly correlated regime. The final section of this thesis reports on preliminary experiments on fluorescence imaging of ^{133}Cs atoms pinned to lattice sites, which will pave the way for the implementation of quantum gas microscopy of molecules.

Declaration

I confirm that no part of the material offered has previously been submitted by myself for a degree in this or any other University. Where material has been generated through joint work, the work of others has been indicated.

Jonathan Maxwell Mortlock
Durham, April 8, 2024

Contents

List of Figures

List of Tables

Acknowledgements

I would like to thank the many people who have enabled this thesis work, whether as co-workers labouring together to build our army of lasers, mirrors and cables, teachers who have patiently taught me and tried to form me into a better physicist or friends and family who have encouraged me and given their support and love.

First, I am thankful to my supervisor, Simon Cornish, for his warm welcome to Durham and his dedication to making sure we have the guidance, motivation and funding (and swift email replies) needed for our research. He admirably blends a passion for efficiency and getting things right with patience in teaching students like myself who are still working out how to.

I am also very indebted to many others I have worked with in the microscope lab. Especially Sarah Bromley who has not only built most of the experiment but found the time to patiently teach me how to tame the machine and persevere to solve technical problems. I'm also thankful to the other postdocs I worked with: Lewis McArd who laid the technical foundations with a lot of foresight, Phil Gregory whose depth of molecule knowledge has been a great help, and Alex, Ana and Dani who worked on the initial building. I thank my fellow PhD students: Mew, Andrew, and especially Alex who taught me a lot in our first months working together to make a Cs BEC, and since then in the quest to make another one 37.2 cm away. Finally, Adarsh has been a fine addition to the lab, bringing along puns, cricket and memes. It's been a blessing to share with these people the happy moments after we've solved a technical problem and get to see physics working as we expected all along.

One of the best things about doing a PhD in the Cornish group and QLM has been

the abundance of competent yet friendly PIs, post-docs and students to learn from and go through the PhD journey with. I'm especially thankful to Alex Guttridge for letting me make good use of the door between our labs to ask for guidance and to the tweezer students Vincent, Stefan and Dan who have kindly solved many technical problems first so we didn't have to. I'm also thankful for QLM's company over some good cakes and on fun conferences and visits once we were allowed out again post-COVID.

This PhD project has particularly relied on support from Durham Physics' technical staff, and I am thankful to the many skilled technicians for their good humour in dealing with my many requests. We have also required a lot of help from the finance office, and I thank them for their efficient and friendly service.

More widely than Durham, I wish to thank Andreas Schindewolf and his colleagues for their excellent hospitality on our trip to MPQ, and especially Till Klostermann for his advice on optical transport. I also thank my all teachers and mentors in Cambridge, especially Ulrich Schneider, Ed Carter, Tijmen Euser and Omid Siddiqui.

I thank Simon and Phil for reading the early drafts of this thesis and providing helpful feedback.

Outside of physics, I wish to thank my former housemates, especially Leo for many sanity-preserving lockdown walks and for sharing his passion for New Testament Greek. I have also been abundantly blessed during my time in Durham by the people of Christchurch, who have been a source of friendship, encouragement, and reminders that in Christ we can find joy in all seasons.

I thank my family for their love and support in all the ups and downs of the last four years, and for instilling in me a love of learning.

Finally, I thank my wonderful wife Vicky. Thank you for walking through this time with me, sympathising with its trials, giving comfort when I needed it and for patient encouragement in thesis writing.

Great are the works of the Lord,
studied by all who delight in them.

Psalm 111:2

Chapter 1

Introduction: Ultracold Molecules

This chapter aims to motivate the work described in this thesis towards a new machine for studying ultracold molecules in optical lattices with single-site resolution. The broader field of ultracold atoms is introduced, and then we consider ultracold molecules, focusing on their use as well-controlled many-body quantum systems. Finally, we review the field of ultracold molecule research at the time of writing.

1.1 Ultracold matter

In the late 20th century atomic physicists began to use laser technology to cool gases to previously unattainable μK temperatures [233, 55, 53]. This, combined with advances in magnetic and optical trapping, led to the realisation of a new *ultracold* regime characterised by low densities and exceptionally low temperatures combining to give high phase space density, $\rho = n\left(\frac{h}{\sqrt{2\pi m k_B T}}\right)^3$. Under these dilute conditions interactions between particles are very simple, dominated by two body s-wave elastic collisions characterised by a single parameter known as the scattering length a_s. However, the high phase space densities lead to exotic quantum effects, notably as the celebrated Bose-Einstein condensation phase transition [57, 154]. The macroscopic occupation of a single quantum state in the BEC phase leads to remarkable phenomena such as quantized vortices and interference between different condensates. The results of many early experiments can be understood using mean field theories due to the weakly interacting

nature of the atoms, and BEC physics was initially interpreted through the lens of "atom optics".

Since then two technical developments have allowed ultracold experiments to access the much more theoretically demanding "strongly correlated" regime [26]. First, the ability to tune the interaction parameter a_s using Feshbach resonances. These resonances occur when a bound molecular state crosses the state of a colliding atom pair, and can be controlled by changing the magnetic field applied to the atoms. This new control parameter allowed for the study of the BEC-BCS cross-over in fermionic gases [31] and phenomena such as bright solitons in bosonic gases [276]. Second was the introduction of optical lattices: periodic conservative potentials for ultracold atoms formed by interfering laser beams. The confinement of the lattice increases the relative strength of interactions compared to kinetic energy and allows the realisation of a quantum phase transition between a superfluid state and an incompressible Mott-insulating state [114]. Both of these experimental developments have led to ultracold gases being used as a radically different platform for studying condensed matter physics, and ultracold experiments are often referred to as "quantum simulators" in the sense that the atoms act as a tunable and/or programmable analogue for models of condensed matter.

Following these experiments, which probed the bulk properties of quantum gases, techniques have been developed to study ultracold atoms at a single particle level. For example, the development of single-site resolved imaging of atoms in Hubbard regime lattices [10, 265], also known as "quantum gas microscopy", has led to studies with access to unprecedented detail of the many-body quantum state of strongly correlated systems [118]. By using the same microscope it is possible to manipulate the atoms in the lattice, allowing researchers to set up carefully controlled out-of-equilibrium initial conditions for experiments. A parallel development has been the deterministic preparation of ordered arrays of atoms using optical tweezers. The ability to rearrange atoms is the ultimate way to remove entropy, resembling Maxwell's proverbial demon [85]. Most tweezer experiments use Rydberg excitation to mediate interactions, however, a few experiments have realised tunnelling between tweezers [148, 310]. Recently lattices and tweezers have been combined, realising an experimental platform with the advantages of both techniques [286, 316].

Exciting atoms to high-lying Rydberg states [35] is just one example of a trend towards pursuing ultracold systems with long-range interactions, beyond the usual short-range *s*-wave contact interactions. Generally speaking, long-range interactions allow for faster propagation of entanglement in quantum systems and can dramatically change the many-body physics. For a review of the theoretical motivation for experiments on long-range interacting systems see [71]. Very long-range interactions with "all to all" connectivity can be realised by placing atoms within optical cavities where the cavity field mediates controllable long-range interactions and the realisation of novel dispersive regimes [241]. Dipolar systems, such as Rydberg atoms [35], strongly magnetic atoms [51] and polar molecules [171], are another set of candidates for realising long-range interacting systems, as in these systems the interaction decays as $1/r^3$, where r is the interparticle distance.

1.2 Ultracold Molecules

Realising strong dipolar interactions is one of many motivations for cooling molecules into the ultracold regime.

Additionally, the rotational and vibrational structure of molecules (Figure 1.1 (a)) gives a new set of degrees of freedom that can be coherently controlled and put to use in experiments. For a full account of the details of the internal level structure of diatomic molecules and how they can be controlled in ultracold experiments see e.g. [24, 14]. Current research using cold and ultracold molecules is directed towards three overarching goals: precision measurement, ultracold chemistry and quantum simulation/ computation. These are illustrated in Figure 1.2, and discussed below.

1.2.1 Precision Measurement

The standard model of high energy physics gives incredibly accurate predictions of the properties of sub-atomic particles, but it fails to explain cosmic questions such as the relative abundance of matter over antimatter, or the nature of astronomical phenomena attributed to dark matter or dark energy. To explain these observations physicists

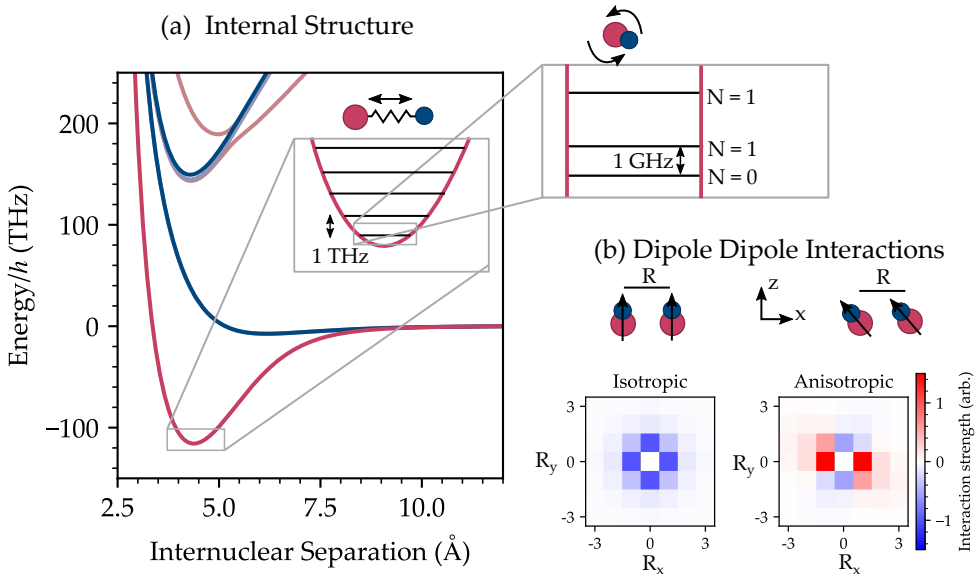

Figure 1.1: (a) The internal structure of ultracold molecules. Shown in the figure are the electronic, vibrational and rotational levels; the latter are particularly useful in quantum science applications. Hyperfine structure is also an important consideration when working with molecules. (b) Polar molecules possess a long-range dipole-dipole interaction, which can be tuned by orienting the dipoles. Shown are the relative interaction strengths between the two lowest rotational states of molecules described by the spin Hamiltonian given in Equation 1.2, plotted in the x-y plane. Tilting the molecular quantisation axis away from the z-axis tunes the x-y plane interactions from isotropic to anisotropic.

hypothesise new forces and particles within the framework of quantum field theory. Certain atoms and molecules contain transitions which are especially sensitive to hypothetical particles [74, 252]. For example, many beyond-standard-model theories predict a larger value for the electron electric dipole moment, but still on a very small $10^{-30}e$ cm scale. This can be measured very precisely using heavy molecules such as YbF [136], HfF^+ [244] and ThO [7]. In these experiments, the internal effective electric fields reach up to 100 GV/cm, probing energy scales well beyond the current range of particle accelerators. Although much progress has been made in these searches using cold mK molecules, bringing them into the ultracold μK regime is predicted to greatly enhance sensitivity [3].

Another example of molecules being used to measure physical constants is in mea-

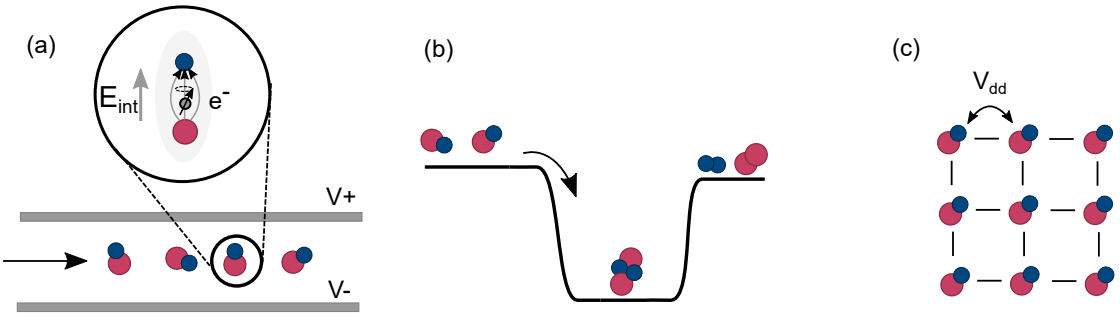

Figure 1.2: Exemplary applications of cold and ultracold molecules. (a) Precision measurement. The internal structure of molecules offers many opportunities to measure quantities relevant to fundamental physics. For example, large effective electric fields inside polar molecules make them sensitive to the electron electric dipole moment. (b) Ultracold chemistry. By preparing ultracold molecules researchers can measure and control chemical reactions at the level of individual quantum states. (c) Quantum simulations. Arrays of molecules have been proposed as highly versatile and tunable model systems for the study of quantum dynamics and/ or quantum computation.

suring the proton to electron mass ratio, specifically looking for variation in this over time [73, 317]. This application can be realised with the bialkali species similar to those studied in this thesis work, as reported in [161].

1.2.2 Ultracold Chemistry

An important application for ultracold molecules is in physical chemistry, where they provide access to the simplest theoretical scenarios with unprecedented experimental control. Although the collision of two diatomic molecules sounds simple, it is in fact still complicated enough to throw up surprises when comparing experiments to theory [176]. As an example, one can consider the recent case of understanding the rapid collisional loss seen in ultracold bialkali molecules [17]. Experiments determined that one important cause of loss was photo-excitation of four-body complexes formed when molecules collide [107, 186], which is particularly strong if the complex is long-lived and hence more likely to be excited. It is possible to probe this complex lifetime indirectly by comparing lifetimes with and without the trapping light [107] or directly using mass spectrometry methods [186]. So far no single theory has managed to adequately account for the variety of lifetimes observed, and this “sticky collision” puzzle is an

ongoing topic of interest in quantum chemistry, a review can be found in [17].

Ultracold molecules offer a unique experimental perspective on reactions generally, enabling control over the reaction outcome via manipulation of the quantum state [225] and recording the full quantum state distribution of a chemical reaction by using a combination of ultracold state preparation techniques with measurement via mass spectrometry [187]. Understanding and controlling molecular collisions is necessary to enable the evaporative cooling of molecules, where much progress has been made experimentally in the past few years [17].

1.2.3 Quantum Simulation and Computation

A third avenue of application for ultracold molecules is in the realisation of highly tunable and quantum-coherent systems for quantum simulation and computation. Since this is the motivation for the experimental work described in this thesis it is worth explaining these applications in more detail.

1.3 Quantum simulation with ultracold molecules

Quantum computing is an umbrella term for any attempt to apply the coherent control available in certain physical systems to solve computationally hard problems; however, it is often used to refer to gate-based or digital quantum computing where universal computation is achieved through discrete unitary operations on a quantum system. Molecules have been proposed as a physical platform for quantum computation [72], and high-fidelity quantum gates that can be implemented with current hardware have been envisaged [221, 137]. These protocols make use of the rich internal structure of molecules using the hyperfine states as a long-lived robust storage qubit and using rotational excitation to introduce entanglement between molecules via the dipole-dipole interaction while avoiding problems such as spontaneous decay associated with Rydberg excitation. These proposals are most relevant to tweezer array experiments where molecules can be rearranged to perform arbitrary operations.

Lattice and bulk samples of polar molecules are more suited to analogue quantum

simulation. A quantum simulator is a well-controlled physical system which is well-described by a model Hamiltonian which is interesting but hard to solve. By studying the physical system it is possible to learn more about the physics of the hard-to-solve model [38]. This is similar to how wind tunnel analogues were used to study fluid dynamics before digital computers could provide accurate simulations. Analogue quantum simulation is essentially a more formal and generalised way of describing the way in which systems like ultracold atoms can realise a different experimental angle on condensed matter physics or other quantum many-body phenomena. Examples of systems that are currently used as quantum simulators include trapped ions, superconducting circuits, ultracold atoms and photons [64].

Lewenstien *et al.* [175] offer a working definition for an analogue quantum simulator:

- A quantum simulator is an experimental system that accurately realises a model Hamiltonian from another field of physics.
- The system must be highly tunable, i.e. able to realise a large portion of the parameter space of the model.
- The system must have a sufficiently long decoherence time to observe the true dynamics of the model.
- Ideally the model and parameter regime realised should be difficult for classical computation. However, there is still value in observing novel phenomena in a real system.

As classical algorithms are refined, the requirements for a quantum simulator to offer a practical advantage are constantly changing, but a good review of the current relative strength of the classical and quantum approaches is given in [64]. The basic argument for "quantum advantage" in physics simulation is the exponential scaling of the number of basis states needed to completely describe a many-body quantum system, as noted 40 years ago by Feynman [90]. There are however many classical algorithms

which either sample from or compress this exponentially large Hilbert space, most notably quantum Monte Carlo methods [96] for finding ground states and tensor network methods [292] for evaluating time evolution. Quantum Monte Carlo methods work very well for all Hamiltonians that don't suffer from the sampling "sign-problem", which is known to be an NP-Hard problem [287]. Models that show the sign problem include the fermionic Hubbard model and spin models with geometric frustration. Computing the out-of-equilibrium dynamics of quantum systems is generally difficult if the dynamics are strongly entangling, leading to the system exploring many basis states. According to [92] many out-of-equilibrium quantum simulators already operate in a regime beyond current classical computation, and [264] offers a detailed characterisation of the degree of entanglement in a quantum simulator.

1.3.1 Dipole-Dipole interactions

As mentioned earlier, ultracold molecules belong to a wider class of well-controlled quantum systems which share a dipole-dipole type interaction between particles. If the dipoles are aligned along the same quantisation axis this interaction takes the form,

$$V_{\mathrm{dd}}(r,\theta) = \frac{d^2}{4\pi\varepsilon_0 r^3}(1-3\cos^2\theta), \tag{1.1}$$

where d is the strength of the electric dipole moment, $r = |\mathbf{r}|$ is the distance between the dipoles and the angle θ is the angle between $\mathbf{r}$ and the molecule quantisation axis. This geometry is illustrated in Figure 1.3. A similar formula exists for magnetic interactions. Dipolar interactions are useful for quantum simulation as they are long-range, anisotropic, and highly tunable.

Ultracold systems with dipolar interactions include Rydberg atoms, heteronuclear molecules and highly magnetic ultracold atoms. Dipolar physics can be studied in certain solid-state systems such as NV-centres [167], which are by nature strongly disordered but are also strongly interacting compared to the timescale of coupling to the environment. The relative strengths and weaknesses of the three ultracold platforms are described in Table 1.1. Molecules have an intermediate strength dipole interaction, which is stronger than the magnetic interaction found in highly magnetic atoms such as

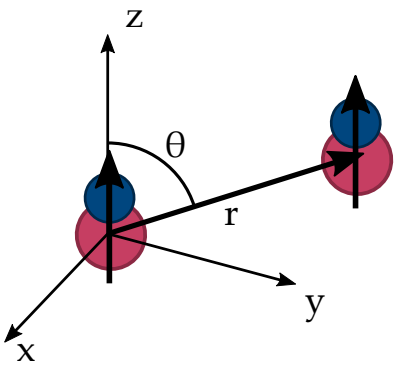

Figure 1.3: Illustration of the dipole-dipole interaction between two molecules with quantization axis along z, as described in Equation (1.1)

Platform	Rydberg Atoms [40]	Ultracold Molecules [52, 135]	Dipolar atoms [277]
Typical V_{dd}/h	1 MHz at 5 μm	500 Hz at 0.7 μm (lattices) 40 Hz at 2 μm (tweezers)	30 Hz at 0.25 μm
Limiting timescale	100 μs effective lifetime	1 s rotational coherence	5 s Lattice lifetime
Current challenges	Trapping of Ry state	Entropy in lattices, coherence times in tweezers	Lattice uniformity

Table 1.1: Comparison of ultracold experimental platforms with dipolar interactions, with values taken from recent publications.

Er or Dy yet significantly weaker than that found in Rydberg atoms. However, unlike Rydberg atoms, molecules don't have any issue with spontaneous decay to lower-lying states, or strong differences in polarisibility between the Rydberg state and the ground state. This means that molecules can be used to study both fixed spin models using their long-range interaction while pinning the molecules to sites of an array and itinerant models when the molecules are allowed to move around [105].

For pinned dipoles, such as polar molecules in a deep optical lattice or tweezer array, dipolar interactions can be used to study lattice models where a spin is encoded in two

internal states coupled by V_{dd}, such as rotational states of molecules [202]. For example, consider an array of molecules initialised in the rotational state $|N = 0\rangle = |\downarrow\rangle$. If some molecules are excited to the $|N = 1\rangle = |\uparrow\rangle$ state, the dipole-dipole interaction leads to an exchange Hamiltonian of the form [104]

$$H_{\mathrm{XXZ}} = \sum_{i \neq j} \left[\frac{J_X}{2} \left(S_i^+ S_j^- + S_i^- S_j^+ \right) + J_Z S_i^z S_j^z \right], \tag{1.2}$$

where the coupling terms are given by the dipole matrix elements between the two states,

$$\begin{aligned} J_X &= \frac{1 - 3\cos^2\theta_{ij}}{4\pi\epsilon_0 r_{ij}^3} d_{\uparrow\downarrow}^2, \\ J_Z &= \frac{1 - 3\cos^2\theta_{ij}}{4\pi\epsilon_0 r_{ij}^3} \left(d_{\uparrow\uparrow} - d_{\downarrow\downarrow} \right), \end{aligned} \tag{1.3}$$

with $d_{s_i s_j} = \langle s_i | \boldsymbol{d} | s_j \rangle$ for $|s\rangle \in \{|\uparrow\rangle, |\downarrow\rangle\}$. Figure 1.1 b shows the spatial structure of this Hamiltonian for two different orientations of the dipole axis relative to the plane of a molecular array. The relative strength of these two terms can be tuned freely by applying a static electric field, and with no electric field, the model reduces to the XY spin model. Any empty sites in the lattice appear as defects, which can be limiting in some applications but can also be used to study the role of disorder in many-body physics [315].

If a third internal state is accessible in the experiment, then the system can be interpreted as the hopping of a particle with an internal spin-half degree of freedom. In this case, the dipole-dipole interaction naturally leads to a model with spin-orbit coupling [279], which can lead to topologically non-trivial band structures [231]. A minimal demonstration of this has been realised in Rydberg tweezer arrays [182]. If more states are included using microwave couplings the internal states can be thought of as a synthetic dimension where the flexibility offered allows implementation of models which are otherwise difficult to realise in experiments [278].

A different type of system can be studied if the dipolar particles are confined in a lattice which allows tunnelling between sites. In this case, the system can be described by an extended Hubbard model (the standard Hubbard model is discussed in detail in

Chapter 5)

$$H = -t \sum_{\langle i,j \rangle} \left(\hat{a}_i^\dagger \hat{a}_j + \hat{a}_j^\dagger \hat{a}_i \right) - \sum_i \mu_i \hat{n}_i + \sum_{i<j} V_{i,j} \hat{n}_i \hat{n}_j. \tag{1.4}$$

Here, $\hat{a}_i^\dagger \hat{a}_j$ describes the tunneling of hard-core bosons (i.e. bosons with infinite on site interactions), $\hat{n}_i$ counts the number of particles on site i and μ_i is the chemical potential, $V_{i,j}$ is the dipole interaction as given in Equation 1.1. The notation $\langle i, j \rangle$ indicates that this sum should be performed only over i and j which correspond to nearest neighbour sites. This model is predicted to have a rich phase diagram at fractional filling [39], which has recently been observed with microscopic resolution in dipolar atoms [277]. Of course there are many more possibilities for quantum simulation with dipolar systems, and a review of the molecular proposals and experimental considerations can be found in [58].

1.4 How are Ultracold Molecules Made?

Having considered the wealth of motivation for experiments on ultracold molecules, this section introduces the methods used to produce them. A detailed history of how these techniques emerged can be found in [14].

Direct Cooling

Perhaps the most obvious way to cool molecules would be to use the same laser cooling techniques used for atoms. The laser cooling of atoms relies on scattering around 1×10^4 photons per atom [95], facilitated by closed transitions between two levels where other states are only populated by rare off-resonant excitation. Atoms that leave the cooling cycle by falling into these "dark" states can be *repumped* back into the cycle to allow cooling to continue. For most alkali atoms only one repump frequency is required.

In molecules, closed laser cooling transitions don't exist because there are no strict selection rules on changes in vibrational quantum number during an electronic transition. In the Franck-Condon approximation, the relative strength of decay into different states is governed by the overlap between the wavefunction of the oscillating nuclei in the excited state with that in the ground state, characterised by a matrix

$M_{v''v'} = \langle \psi_{v''} | \psi_{v'} \rangle$. These overlap integrals are known as Franck-Condon factors. For laser cooling to be feasible, the matrix of overlap integrals $M_{v''v'}$ must be nearly diagonal. Physically this means that the shape of the vibrational potential must be minimally affected by exciting the electronic transition used for laser cooling. This condition is met in free-radical species that have a valence electron which plays almost no part in the chemical bond. For example, in CaF only 2 repump lasers (with appropriate sidebands from radio-frequency modulation) are required to make a Magneto-Optical Trap (MOT) [5]. Great progress has been made in this field recently, including the loading of tweezer arrays [4] and the realisation of a MOT of polyatomic free radicals [295]. Even so, the laser cooling of molecules will always be much more complicated compared to atoms and reaching the quantum degenerate regime in this way is not yet possible.

Indirect formation

An alternative way of making ultracold molecules is to combine pre-cooled atoms, as first demonstrated by a pioneering experiment at JILA [220]. ^{40}K and ^{87}Rb atoms were associated using an interspecies magnetic Feshbach resonance into a weakly-bound state and then transferred using a coherent two-photon process known as Stimulated Raman Adiabatic Passage (STIRAP) to the rovibrational ground state, forming a sample at 350nK and phase space density $\rho = 0.02$. In the following 15 years, this technique has been investigated for most bi-alkali combinations, with the successful creation of ground state heteronuclear ^{23}Na^{6}Li [248][1], ^{23}Na^{40}K [227], ^{23}Na^{39}K [297], ^{23}Na^{87}Rb [122], ^{23}Na^{133}Cs [275], ^{40}K^{87}Rb [220], ^{41}K^{87}Rb [1] and the molecule which this thesis is focused on, ^{87}Rb^{133}Cs [280, 212].

The first step of the association method is to use a magnetic Feshbach resonance to transfer atoms into a weakly-bound state. Magnetic Feshbach resonances [47] occur when there is an avoided crossing between the state of two colliding atoms and a bound molecular state in a potential with a higher energy atom-pair state, as shown in Figure 1.4. The presence of the avoided crossing dramatically changes the scattering behaviour of the atoms and is widely used to control atomic interactions using an applied magnetic field. As already mentioned, controlling interactions between atoms in this

[1] This species was formed in the ground state of the triplet potential

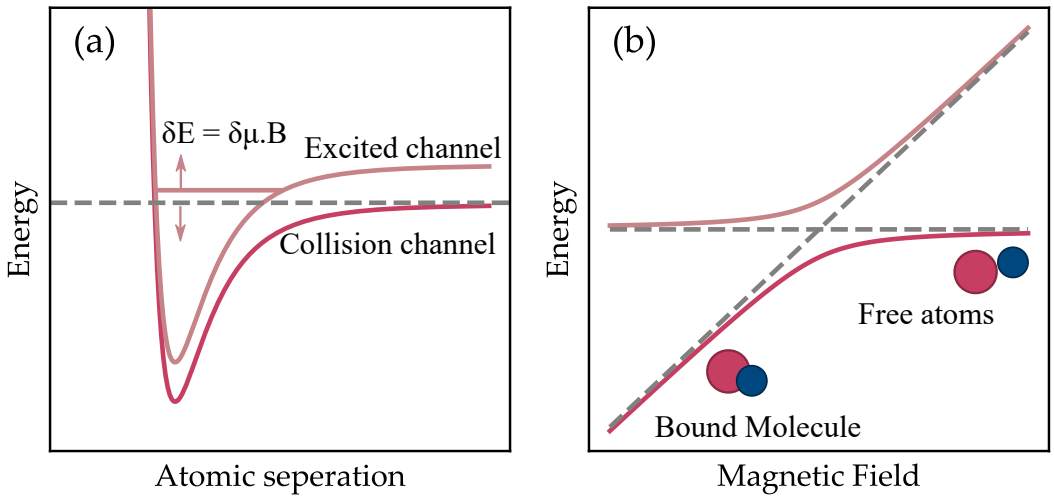

Figure 1.4: Magneto-association of atoms using an atomic Feshbach resonance. (a) shows the potential energy curves for two different atomic pair states. Ultracold atoms colliding with energy just above the threshold energy of the lower channel (dark red) can resonantly couple to a bound state of an excited state potential (light red). If there is a differential magnetic moment, $\delta\mu$, between these channels, then the energy difference between this bound state and the state of the colliding atom can be manipulated with the magnetic field with the energy difference $\delta E = \delta\mu B$. This forms an avoiding crossing as illustrated in (b). Adiabatically traversing the avoided crossing via sweeping the field colliding pairs of atoms can be converted to weakly bound Feschbach molecules, which have a well-defined molecular quantum state.

way has become a key technique in the field, allowing the condensation of species with otherwise unfavourable collisional properties such as ^{85}Rb [59] and ^{133}Cs [301]. Tunable interactions can also be used to realise exotic quantum states such as bright solitons [156], negative temperatures [32] and supersolids in atoms with strong magnetic dipolar interactions [30, 282, 50].

To make molecules, the magnetic field is swept to adiabatically follow this avoided crossing, as illustrated in Figure 1.4, or an RF pulse is used to transfer the population from one branch to another [163]. The resulting "Feshbach molecule" is very delicate, being bound by only a few MHz and has a negligible electric dipole moment. The many-body physics of magneto-association is quite subtle, and is related to the physics

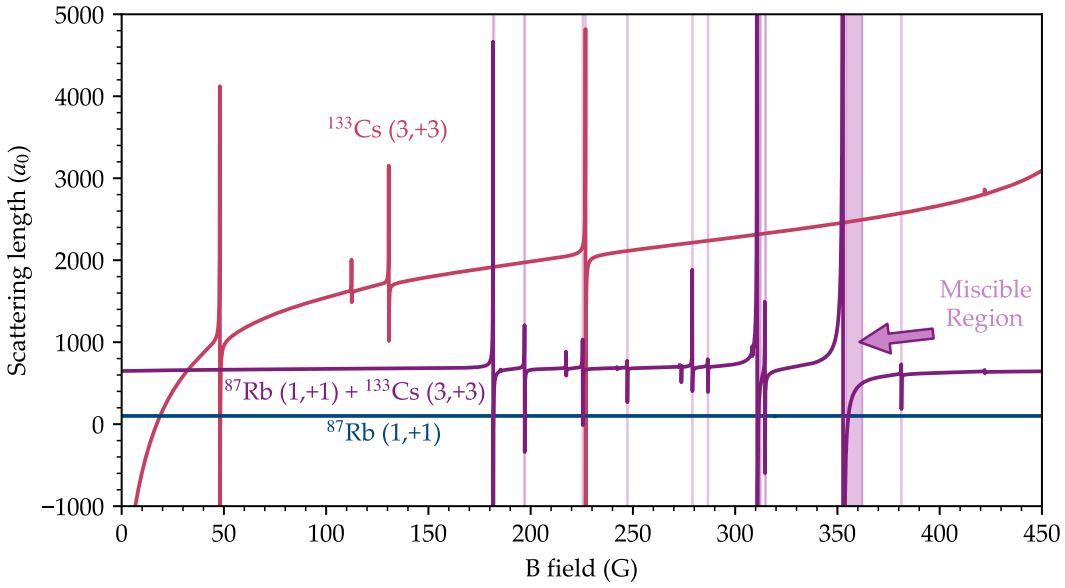

Figure 1.5: Feshbach spectra of $^{87}Rb_2$, $^{133}Cs_2$, and the $^{87}Rb^{133}Cs$, shown for the hyperfine ground states. Molecules have been made using the interspecies resonances at 180 G and 350 G. Due to the large ^{133}Cs scattering length the BECs are only miscible in narrow windows near these resonances, as indicated by the purple shading. Calculations were performed by Jeremy Hutson's group.

of "polarons", quasiparticles consisting of an impurity particle dressed by a cloud of majority particles [80]. For a long time, it has been imagined that a good way to ensure efficient magnetoassociation and therefore high phase space density molecular samples would be to use an optical lattice to prepare a dual-species Mott or band insulating state [144], where interactions would naturally prepare a state with a single particle of each species per site. This has been studied experimentally [216, 240], and it was found that the process is strongly dependent on the adiabatic loading into the lattice[2] and interspecies interactions [251].

The magneto-association of $^{87}Rb^{133}Cs$ is complicated compared to other bialkali combinations as the interspecies background scattering length is unusually large, as shown in Figure 1.5. This means that the two species are immiscible at high phase

[2]See Chapter 5 for a discussion of this in the single species case

space density, and separate within the trap [197, 173]. In Figure 1.5 the narrow miscible regions where $a_{\mathrm{RbCs}} < \sqrt{a_{\mathrm{Cs}} a_{\mathrm{Rb}}}$ are shaded in purple. This miscibility problem has been overcome by performing association just above the BEC transition when the species are still miscible. This method has been used both in the older Durham RbCs experiment [212] and the first iteration of the Innsbruck experiment [280]. In later iterations of the Innsbruck experiment, a more complicated but ultimately more efficient method was developed using movable optical traps and the Mott insulator phase of ^{133}Cs in an optical lattice [239]. It should be noted that in tightly confining traps the large interspecies interaction makes it possible to cross into a weakly bound molecular state without the need for a Feshbach resonance by merging two traps together, a process termed "mergoassociation" [247].

Once a weakly bound molecule is formed it is possible to efficiently transfer to the ro-vibrational ground state using STIRAP [19]. The process is easy to describe formally, but has no classical analogue and so can be counter-intuitive to understand. The basic idea can be illustrated with the ^{87}Rb^{133}Cs STIRAP scheme shown in Figure 1.6. We isolate a three-level system formed by the Feshbach molecule state $|F\rangle$, an excited state $|E\rangle$ and the ground state $|G\rangle$, which are coupled by lasers into a Λ arrangement. To transfer from $|F\rangle$ to $|G\rangle$ the laser couplings are pulsed so that the system begins in the dark state which is then adiabatically transformed from $|F\rangle$ to $|G\rangle$ without ever populating $|E\rangle$, as shown in Figure 1.6 (b). The beauty of this process is that the phase-space density and well-defined initial molecular state of the atoms in $|F\rangle$ are preserved, allowing the creation of very cold samples of molecules in a single quantum state.

The technical factors affecting the efficiency of STIRAP of molecules are discussed in [110]. To summarise, efficient STIRAP requires picking a good excited state and using high-intensity, narrow line-width coupling beams. A good excited state for STIRAP combines strong coupling to the $|F\rangle$ and $|G\rangle$ states with a long lifetime [2]. Since gas phase references are not available for these molecular transitions, temperature-stabilized high finesse cavities are used as frequency standards. This also allows the implementation of a Pound–Drever–Hall lock [78] to narrow the linewidth of the laser. To improve the phase noise offset from the carrier at the Rabi frequency filter cavities are often used [14]. An alternative method for improving the laser phase noise is to use feedforward

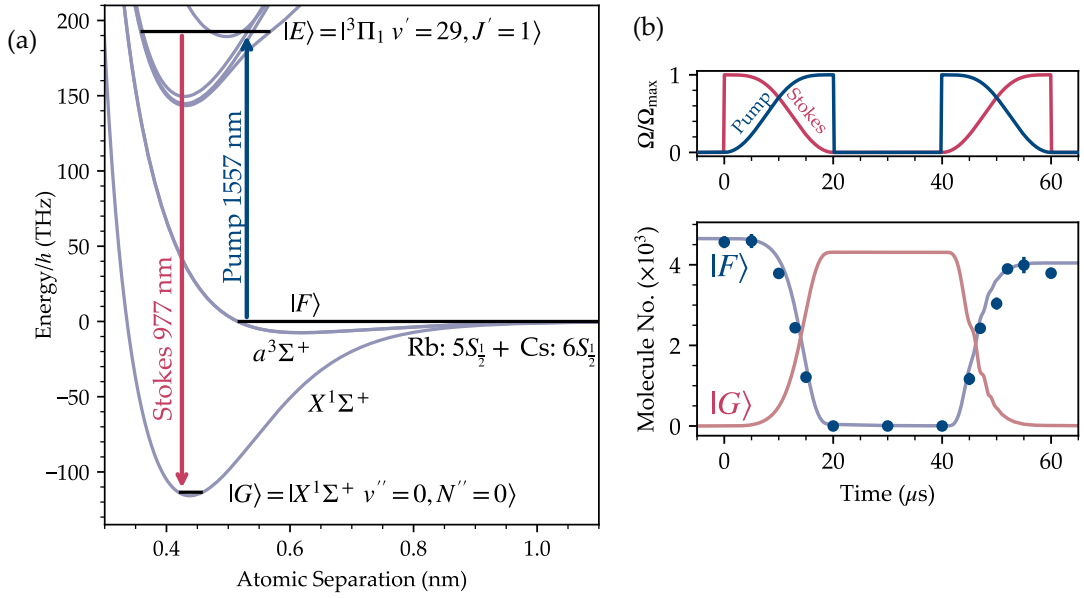

Figure 1.6: ^{87}Rb^{133}Cs STIRAP sequence as used in the older RbCs experiment [24]. (a) The level scheme used. (b) The experimental pulse sequence, and observation of coherent transfer between the states. The solid lines in the lower figure show an optical Bloch equation simulation, and molecule number data is from imaging of the $|F\rangle$ state via magnetic dissociation into atoms.

techniques [179]. Typical one way STIRAP efficiencies for ^{87}Rb^{133}Cs are currently around 92% [213].

To detect the molecules, the whole association process must be reversed to give atoms that can be imaged using their cycling transitions. Thus the efficiency of STIRAP is very important for applications that require high-fidelity readout like quantum simulation or computation.

1.5 State of the art of polar molecule experiments

To understand the context of this thesis it is helpful to review the present status of ultracold molecule research. There are perhaps four trends that stand out as areas of interest: controlling collisions, producing molecular arrays, generating entanglement with dipolar interactions and controlling decoherence. More detailed reviews of the

field at the time of writing of this thesis can be found in the following articles [171, 58].

1.5.1 Controlled Collisions and Evaporation

First, much progress has been made recently in understanding and controlling collisions of ultracold molecules. Initially, it was expected that inelastic molecular collisions could be avoided by choosing chemically inert species. However, experiments found that near-universal inelastic loss was a feature of all species, temporarily dashing hopes for evaporative cooling of molecules[3]. In some species the cause of inelastic loss was determined to be laser excitation of the long-lived collision complex [107, 186], but this is not the case in all species [15].

Fortunately, inelastic collisions can be prevented by adding a repulsive barrier between the long-range dipolar potential and the complicated short-range potential. This can be achieved through control of the dimensionality of the trap [75], resonant electric fields [194] and microwave dressing [309, 259, 183, 20]. Recently many groups have reported evaporative cooling of molecules using these methods, reaching degeneracy in fermions [290, 259] and bosons [21].

In addition to these developments in shielding, molecular collisions can be coherently controlled using resonances. Atom-molecule [313] and even molecule-molecule [229] magnetic Feshbach resonances have been recently observed, opening up the opportunity to build up polyatomic molecules via association [312]. Remarkably the microwave shielding technique also produces "field-linked" resonances [41], which can be swept over by controlling the microwave ellipticity to "electroassociate" ultracold tetratomic molecules [42].

1.5.2 Generating Arrays of Single Molecules

Second, many groups are working towards implementing arrays of molecules for quantum science applications. In the ultracold atom community, recent years have seen many exciting developments in microscopic control and readout of arrays of atoms as discussed earlier.

[3]The evaporative cooling technique as used for atoms is discussed in chapter 4

Recently these techniques have been applied to molecules. Using CaF, researchers have been able to prepare molecules in rearrangeable optical tweezers [4]. Recent technical progress has included the demonstration of efficient cooling inside the tweezers [189], a necessary step for long rotational coherence times. Tweezer arrays are also being pursued for associated molecules, via merging of tweezers of each individual species, [33] and these have recently been demonstrated for NaCs [320] and RbCs [125]. In optical lattices, single-site resolved imaging of molecules has been demonstrated in associated NaRb [243]. Quantum gas microscopy of RbCs is the goal of the experiment developed in this thesis, and microscopy of other bialkali species is being actively pursued in other groups [99, 61].

1.5.3 Generating entanglement using the dipole interaction

For almost 15 years ultracold molecules have been pursued with the goal of utilising the dipole-dipole interaction and rotational states for quantum science. Apart from the pioneering KRb experiment [308], observing the dipole-dipole interaction was beyond the reach of other experiments.

Recently however the dipole-dipole spin exchange physics has been observed in new experiments with microscopic resolution. The first of the new generation of experiments to observe the dipole-dipole interaction was the NaRb quantum gas microscope [52], where the pioneering JILA experiment [308] was repeated with single-site resolution of correlations between sites revealing the anisotropic dipole-dipole interaction exactly as it was predicted to be. Shortly after this, two groups were able to show entanglement between molecules produced by the dipole interaction between CaF molecules in tweezers [135, 11]. The original KRb experiment has also recently investigated the many-body spin dynamics of dipoles free to move around in a trap [177]. The field is eagerly awaiting the publication of similar results from the bi-alkali tweezer experiments, and the advent of near degenerate molecules in experiments with evaporative cooling will provide the perfect starting point for large-scale quantum simulation.

Another avenue being pursued to generate entanglement between molecules is to interface molecules and Rydberg atoms [300, 318], with the first observation of Rydberg

blockade induced by a polar molecule being observed in RbCs [125]. This approach also offers the exciting possibility of readout of the molecular state without the need for dissociating the molecule.

1.5.4 Control of decoherence

Effective quantum technology with molecules relies on coherence between the molecular states used. Understanding and controlling coherence has been a major focus of recent work. Molecular hyperfine states have emerged as one of the most long-lived ways to store quantum information, with second-scale coherence demonstrated in NaK [228] and an exceptionally long >5.6 s coherence time reported between carefully chosen states of RbCs [108]. Long hyperfine coherence times have also been recorded in an optical lattice with NaRb [184].

Although hyperfine states make for excellent storage qubits, they are hard to entangle, so rotational coherence is the relevant quantity for most quantum simulation experiments. For most experiments with optically trapped molecules differential light shifts are the dominant source of dephasing. Since the differential light shift is a single particle dephasing effect, it can be removed to a certain extent by sequences of global single qubit operations developed in NMR and solid-state physics, such as the XY8 pulse protocol [177]. There are also many methods to reduce the strength of the differential light shift. The large variety of these methods demonstrates the richness of the internal structure of molecules. The scalar light shift between $|N = 0\rangle$ and $|N = 1\rangle$ rotational states can be cancelled by orienting the polarisation of the light at a specific "magic" angle to the molecular quantization axis [219]. This leaves a residual tensor light shift, which means the "magic" angle is intensity dependant, ruling out perfect cancellation. This tensor component can be minimised by applying a DC electric field to manipulate the hyperfine structure of the rotational state [23, 263]. Similarly, magnetic fields can be used [23, 52]. A more radical solution is to change the wavelength of the optical trap. In bialkali molecules trapping near the narrow line $X^1\Sigma^+ \rightarrow b^3\Pi$ transition provides a magic wavelength, which has been investigated in NaK [16], NaRb [130] and RbCs, where a second scale rotational coherence time was reported [109], long enough to ob-

serve the decoherence effect of dipole-dipole interactions in a dilute thermal gas. This magic wavelength condition is predicted to hold for multiple rotational states at once [121].

1.6 This Work

This thesis documents the construction of a new apparatus for ultracold molecules, designed to allow single-site resolved imaging of ^{87}Rb^{133}Cs molecules. The new machine is planned to allow investigation of the dipolar physics of lattice confined molecules with full rotational state-resolved readout via detection of both Rb and Cs [62].

Chapter 2 gives a high-level overview of the experiment, and a summary of the initial stages of cooling of ^{87}Rb and ^{133}Cs. Chapter 3 details our implementation of moving lattice optical transport to allow for increased optical access for our quantum gas microscope. Chapter 4 describes the final cooling stages and our observation of BECs of both species. Chapter 5 gives a detailed introduction to the physics of ultracold atoms in optical lattices, detailing the implementation of a 3D high-power optical lattice for quantum gas microscopy and reports on the observation of the superfluid to Mott-insulator phase transition. Chapter 6 gives an introduction to the quantum gas microscopy technique, details the design and implementation of our high-resolution imaging system, and gives preliminary results on fluorescence imaging of ^{133}Cs. Finally, Chapter 7 offers an outlook for the future completion of the machine, possible solutions to the current challenges and opportunities for future experiments.

1.7 Contributions of the Author

All cold atom experiments are a team effort, so it is helpful to acknowledge the specific contributions of various people to the work described in this thesis and clarify which parts I worked on. The lab work was led by Sarah Bromley, and the project was overseen by Simon Cornish. Several Post-docs contributed to the experiment, including Philip Gregory, Lewis McArd, Alex Alampounti, Liz Bridge and Danielle Pizzy. Mew Ratkata, Andrew Innes, Alex Matthies and Adarsh Ragurham worked in the lab as PhD

students. Alfie Renn also contributed as a Master's student. In the following, I provide a rough overview of how our time in the lab was spent, and which parts people contributed to.

The experimental apparatus was designed by Ana, Phil, Vincent Brooks and Lewis. When I arrived much of the initial vacuum and laser cooling work had been completed by Sarah, Alex Alampounti, Liz, Dani, Lewis, Mew and Andrew. Alex Matthies and I oversaw the design and implementation of the first 1064 nm dimple trap used for Cs BEC production in the MOT chamber, as used in [238]. During COVID-19 I worked on the design and testing of our high-resolution imaging system, and the development of a codebase for image reconstruction. After lockdown restrictions were lifted I worked with Sarah and Alex Matthies to implement optical transport based on calculations Alex had done, where my work was particularly focused on the electronics for frequency control. Alex Matthies performed a detailed characterisation of optical transport, which is reported in their thesis [195] and [196].

After Adarsh and I set up absorption imaging in the science cell, Sarah and Alex Matthies led the set-up of the magnetic field coils around the science cell and I oversaw the work to put the objective in place. The mechanical design for the objective and coil mounting was done by Lewis, who also designed the high-power shutters and beam dumps. Around this time I developed the fast waveplate rotation mount which was characterised by Adarsh and described in [237].

Following this I designed the dipole traps described in Chapter 4 and Sarah and I implemented them. Sarah and I optimised the sequences for forming BEC for both species. This work is reported in the final section of [196]. Similarly, I designed and Sarah and I implemented the 3D optical lattice described in Chapter 5, with initial help in the alignment from Alex Matthies. I performed the measurements on the superfluid to Mott insulator transition. Sarah and I worked on fluorescence imaging of Cs and attempts at layer selection during the final months of my thesis work.

1.8 List of Publications

As mentioned in the previous section, the work presented in this thesis has led to the following publications. The final publication has been submitted for peer review.

- Apichayaporn Ratkata, Philip D. Gregory, Andrew D. Innes, Jonas A. Matthies, Lewis A. McArd, Jonathan M. Mortlock, M. S. Safronova, Sarah L. Bromley, and Simon L. Cornish. "Measurement of the Tune-out Wavelength for ^{133}Cs at 880 nm". In: *Physical Review A* 104.5 (Nov. 22, 2021), p. 052813. DOI: 10.1103/PhysRevA.104.052813

- Adarsh P. Raghuram, Jonathan M. Mortlock, Sarah L. Bromley, and Simon L. Cornish. "A Motorized Rotation Mount for the Switching of an Optical Beam Path in under 20 ms Using Polarization Control". In: *Review of Scientific Instruments* 94.6 (June 1, 2023), p. 063201. ISSN: 0034-6748. DOI: 10.1063/5.0139647

- Alex J. Matthies, Jonathan M. Mortlock, Lewis A. McArd, Adarsh P. Raghuram, Andrew D. Innes, Philip D. Gregory, Sarah L. Bromley, and Simon L. Cornish. *Long Distance Optical Conveyor-Belt Transport of Ultracold ^{133}Cs and ^{87}Rb Atoms*. July 25, 2023. DOI: 10.48550/arXiv.2307.13382. arXiv: 2307.13382 [cond-mat, physics:physics]. preprint

Chapter 2

A New Apparatus for Rb and Cs

2.1 Introduction

This shorter chapter aims to describe the design of our ultracold molecule machine, especially the vacuum and laser cooling systems. Much of this work was done before the author arrived, but it is important to understand as it impacts all the work described in this thesis. Since our experiment incorporates many of the design features of the older Durham CsYb mixtures experiment, a large amount of reference is made to [124], and to a certain extent the older RbCs experiment [198]. The apparatus was also described briefly in [238]. This chapter (and the rest of the thesis) is written assuming familiarity with concepts such as Doppler cooling, the Magneto-Optical Trap and trapping of atoms in off-resonant laser fields. An introduction to these can be found in e.g. [95, 54, 115]

As discussed in Chapter 1, to create ultracold bialkali molecules, we must first prepare a dual-species near-degenerate mixture. Our further goal of single-site resolved imaging requires optical access for a 3D optical lattice and a high-NA lens. Additionally, many experiments with molecules rely on the ability to apply well-controlled large electric fields. These three objectives must be held in mind in the design of our quantum gas microscope for molecules.

The apparatus was also designed to improve upon the older Durham RbCs experiment [197, 211] in three ways. First, by using the powerful Degenerate Raman Sideband

Cooling (DRSC) technique [299, 150] we can avoid the need for a magnetic trap which should significantly reduce the cycle time. Second, the experiment is designed with an additional Ultra-high vacuum "science cell" to provide the improved optical access required for microscopy. Finally, the cell is equipped with in-vacuum electrodes to allow for better control of the electric field at the molecules. The experiment was also designed with the possibility of investigating ^{41}KCs mixtures, which are predicted to have a rich low-field Feshbach structure which could allow easier association of molecules [117].

2.2 Vacuum System

Our vacuum apparatus is illustrated in Figure 2.1, and consists of four distinct regions. Atoms are captured from two 2D$^+$ MOT vapour cells on either side of the chamber. These cells supply beams of cold ^{133}Cs and ^{87}Rb to a dodecagonal stainless steel 3D MOT chamber (MC), where atoms are initially captured and cooled using the ubiquitous MOT technique then further cooled using DRSC. This allows the atoms to be captured in a conservative optical trap. The full details of the laser cooling methods we use are discussed in Section 2.4. Finally, optical transport is used to transfer the ultracold mixture to a glass science cell (SC) with optical access for a 3D lattice, high-NA lens and in-vacuum electrodes.

2D$^+$ MOTs [77] use transverse cooling to realise a simple and compact atomic beam source, compared to the alternative of a Zeeman slower. They are easiest to realise for the heavy alkali species such as ^{87}Rb and ^{133}Cs which have comparatively high vapour pressure at room temperature. An illustration of our 2D$^+$ MOT design is shown in Figure 2.2. We use two 2D MOTs, one for ^{133}Cs and one which can supply ^{87}Rb and the bosonic K isotopes[1], for possible future experiments investigating KCs molecules.

In addition to the beams and coils needed for transverse cooling, the key features are: (i) a differential pumping section with a small aperture which allows the vapour pressure in the source cell to be much higher than the UHV conditions in the rest of the

[1]The K dispensers are natural abundance and so cannot provide significant ^{40}K pressure. The Rb dispensers are also natural abundance, but our laser system is not set up to cool ^{85}Rb.

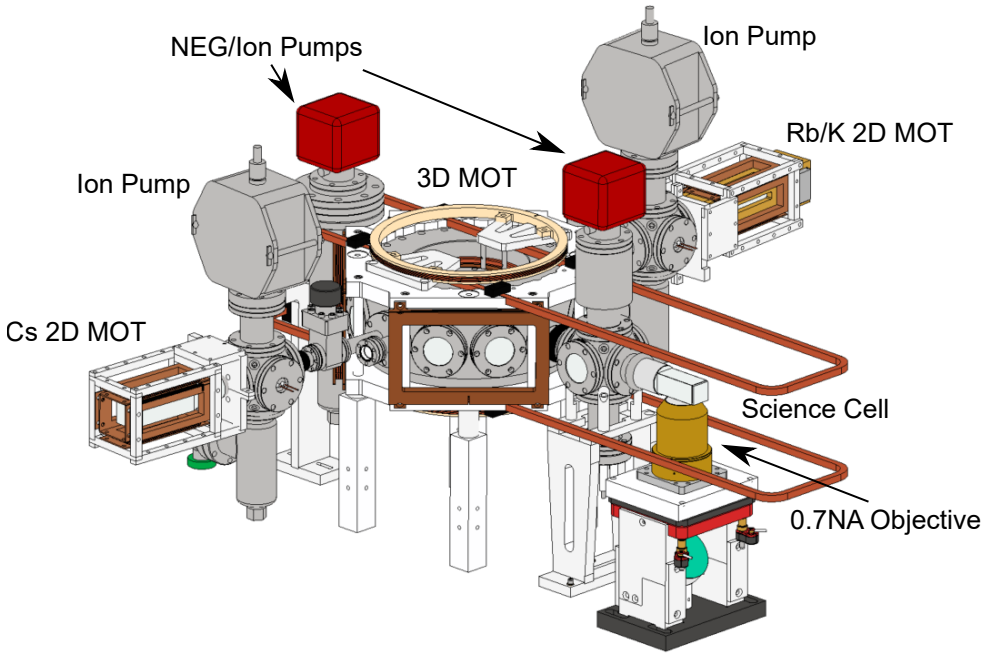

Figure 2.1: Schematic of the vacuum system. The coils around the Science Cell are omitted for clarity.

chamber; (ii) a push/retarding beam pair which allow us to control the velocity of the atomic beam to optimise capture into the 3D MOT; (iii) dispensers, which give a simple way to control the pressure of the relevant species and (iv) for the ^{87}Rb/K 2D^{+} MOT, a heater array to increase the alkali pressure. The vacuum in each 2D MOT vapour cell is maintained by a 10 L/s ion pump[2].

In the rest of the vacuum chamber, maintaining ultrahigh vacuum (UHV) conditions is key to ensuring background collisions are not a limiting factor in our experiments. The main section has two pumps which combine a non-evaporable getter (NEG) and an ion pump[3] to maintain UHV conditions and is connected to the 2D MOT vapour cells by a differential pumping section of 1 mm diameter and 13.25 mm length which enables a pressure difference between the two parts of the vacuum system.

In a differential pumping section, the ratio of the pressures on either side is deter-

[2]Agilent VacIon 10
[3]NEXTorr

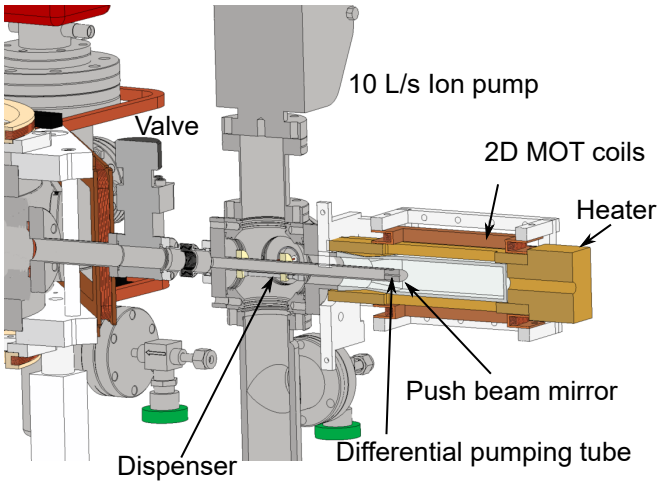

Figure 2.2: Annotated cut-away schematic of the Rb/K 2D$^+$ MOT vacuum system.

mined by the ratio of the pumping rate on the low-pressure side to the vacuum conductance. Assuming molecular flow, where the ratio of the mean free path of the gas to the size of the chamber is large, the pressure differential can be calculated using the vacuum electrical circuit analogy [100] as

$$P_1/P_2 = S/C \tag{2.1}$$

where S is the pumping rate in the UHV region in l^{-1} and C is the vacuum conductance. In the case of a pipe of radius r, length L [302]

$$C = \frac{4}{3}\sqrt{\frac{2\pi k_B T}{m}}\frac{r^3}{L} \tag{2.2}$$

i.e. around 5.8×10^{-3} L/s for ^{87}Rb at 350 K in the heated 2D MOT or 4.3×10^{-3} L/s for the ^{133}Cs room temperature 2D MOT. Hence the differential pumping can maintain a pressure ratio of about 3000 for a conservative estimate of an effective pumping rate of 20 l/s in the UHV section.

To get as much optical power into the chamber as possible we use anti-reflection (AR) coated viewports and an AR-coated glass science cell. Although AR coatings improve performance at the target wavelengths, they can make the surfaces highly reflective at other wavelengths which can be a problem if an unforeseen wavelength is required.

2.2.1 Science Cell

One of the key upgrades of our experiment compared to the previous Durham Rb-Cs experiment is the glass cell[4] which allows high optical access and in-vacuum electrodes. The cell was manufactured to have very flat windows which facilitates high-resolution imaging by reducing aberrations. The flatness is specified to $< \lambda/2$ per cm.

To fully realise the potential of ultracold molecules for quantum simulation requires large stable electric fields. In ultracold molecule experiments which have tried to use electrodes outside the vacuum cell, the electrical polarisation of the cell has been a major problem [110]. Stray fields are particularly problematic for molecule experiments as they shift the STIRAP resonance. Although the charge build-up can be removed with UV light [24], the process is slow and not very reliable. We hope to avoid this problem by using in-vacuum electrodes. The electrodes consist of four 2 mm diameter metal rods arranged in a rectangular geometry, with centre-to-centre spacings of 9.6 mm and 5.6 mm. The electrodes are visible in the cross-sectional drawing in Figure 2.3. The electrodes are the same design as used in the Durham RbCs tweezer experiment [273, 34] where using the stark shift of a Rydberg state they measured a peak electric field vs applied voltage of 0.74 (V/cm)/V.

2.3 Magnetic field Control

Many aspects of the experimental sequence rely on careful control of the magnetic field experienced by the atoms, which is achieved by running current through copper coils around the vacuum chamber.

2.3.1 2D MOTs

The 2D MOT cells are both surrounded by two pairs of racetrack-shaped coils, one for each horizontal axis. Each coil pair consists of 36 windings of 1 mm diameter copper wire arranged in a quadrupole configuration to provide a 4 G cm^{-1} A^{-1} gradient and 6 windings in a Helmholtz configuration to provide a 0.9 G A^{-1} offset to allow fine control

[4] Cold Quanta

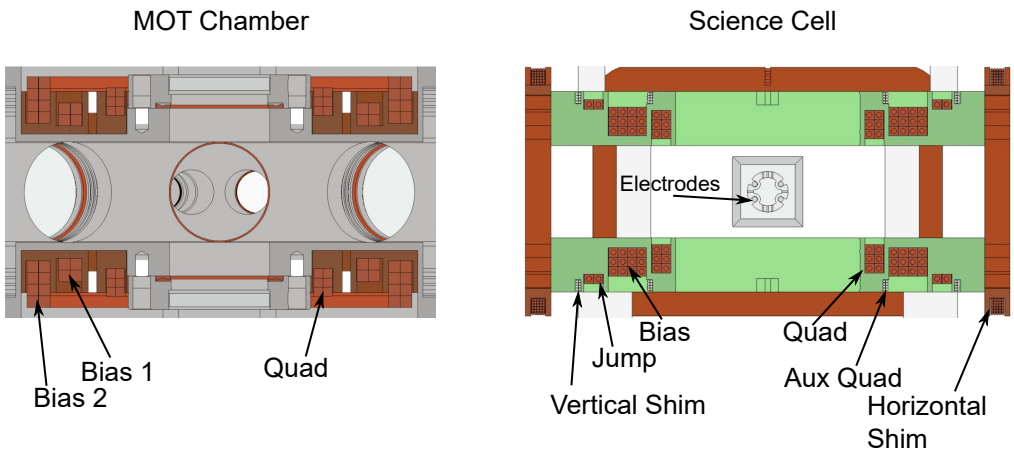

Figure 2.3: Cross-section of the coils around the two trapping regions. Apart from the horizontal shim coils, all other coils are circular. The four rods used as in-vacuum electrodes are also shown, housed in a ceramic mount.

of the atomic beam position. The heat from the resistance of these coils is beneficial in raising the temperature of the vapour cell to increase the partial pressure of the alkali species.

2.3.2 High Current Coils

In the MC and SC regions, we require magnetic fields up to strengths of 400 G to address interspecies Feshbach resonances and field gradients of ≈50 G cm^{-1} for magnetic levitation[5]. Applications such as magnetoassociation require the field to be set with high precision. To achieve these fields we use a tried and tested design based on running high currents (50-300 A) through water-cooled copper tubing.

The design of the coils around each chamber is shown in Figure 2.3. The Helmholtz configuration "bias" coils are arranged to approximately fulfil the requirement for maximal uniformity. For radius R and separation s this is simply $R = s$. Similarly, the anti-Helmholtz gradient coils are arranged so that $s \approx \sqrt{3}R$ to achieve uniform field gradients. The field strengths of the coils are listed in Table 2.1. To assist with fast sweeps of the magnetic field required for magnetoassociation we have two pairs of bias

[5]Note this is significantly lower than the gradients required for a magnetic trap, typically around 200 G cm^{-1}

Coil Name	Field ($G\,A^{-1}$)	Field Gradient ($G\,cm^{-1}\,A^{-1}$)	Total Coil Resistance ($m\Omega$)
MC Quad		0.31	5.6
MC Feshbach	1.04		8.8
MC Jump	0.61		3.6
Racetrack	0.26		30
SC Quad		0.47	4.3
SC Feshbach	2.07		11.4
SC Jump	0.28		2.37

Table 2.1: High current coil parameters. The resistance of the coils can be used to estimate the cooling requirements. The field and field gradient values are those at the position of the atoms.

coils, with the idea that the larger coil is used to reach the Feshbach resonance, and the smaller coil is used to sweep the field. To control the bias field over the transport distance we have a racetrack-shaped coil, which is visible in Figure 2.1.

We use a control system which has its origins in the ^{85}Rb experiment at JILA [242], where a closed loop hall sensor measures the current through the coil, and feedback is provided by a parallel MOSFET[6] array. A PI servo is implemented using analogue electronics and is designed and tuned to give maximal low-frequency loop gain without causing instability around the 90-degree phase lag frequency, which usually occurs between 1-10 kHz. The integral component of the feedback loop can be bypassed to perform fast jumps of the coil. For applications which require the field to be set precisely, there is a circuit which provides a highly stable voltage reference, which allows < 10 ppm current stability. Full details of this circuit can be found in other theses [242, 226].

2.3.3 Shim coils

Around both of the UHV regions, we also have three Helmholtz pairs to provide smaller bias fields in any direction, up to around 5 G. These are used for adjusting the location

[6]IXYS IXFN 180N15P

of the MOT, nulling the background field during optical molasses and setting a quantization axis during steps which require optical pumping such as DRSC and absorption imaging.

2.4 Laser cooling

This section gives an overview of the laser cooling of ^{133}Cs and ^{87}Rb, which are very similar species until collisions between the atoms are considered, as is seen in Figure 2.4, which shows the transitions relevant to our laser cooling. Although it is not the focus of this thesis, our machine is also set up to laser cool the bosonic K isotopes. The laser cooling of K is slightly different and this setup will be discussed in more detail in Andrew Innes' thesis.

For both ^{87}Rb and ^{133}Cs we use the same laser cooling techniques, first a standard MOT based on the D_2 cycling transition, after compressing the MOT we apply a stage of optical molasses to reduce the temperature. After this, we perform DRSC using a near-resonant optical lattice. All of this laser cooling can be done simultaneously for both species but requires care to find conditions which are optimal for both. Alternatively, the species can be cooled sequentially, as in our current plan for achieving high phase-space density mixtures in the science cell, which is discussed in Chapter 7.

2.4.1 MOT and Molasses

The MOTs are formed in the standard way using light red-detuned of the D_2 cycling transition ($|F = 4\rangle \rightarrow |F' = 5\rangle$ for ^{133}Cs and $|F = 2\rangle \rightarrow |F' = 3\rangle$ for ^{87}Rb). Off resonant scattering into the next lowest excited hyperfine state ($|F' = 4\rangle$ or $|F' = 1\rangle$) leads to a decay path to the lower hyperfine ground state, and so repump light is required to eject atoms from this state back into the cooling cycle. The typical 2D and 3D MOT parameters for each species are given in Table 2.2. The only compromise that must be established when loading both species is the field gradient of the 3D MOT. We use retro-reflected MOT beams to realise a simple optical design.

In our case of a two-species MOT, it is important to displace the centre positions of

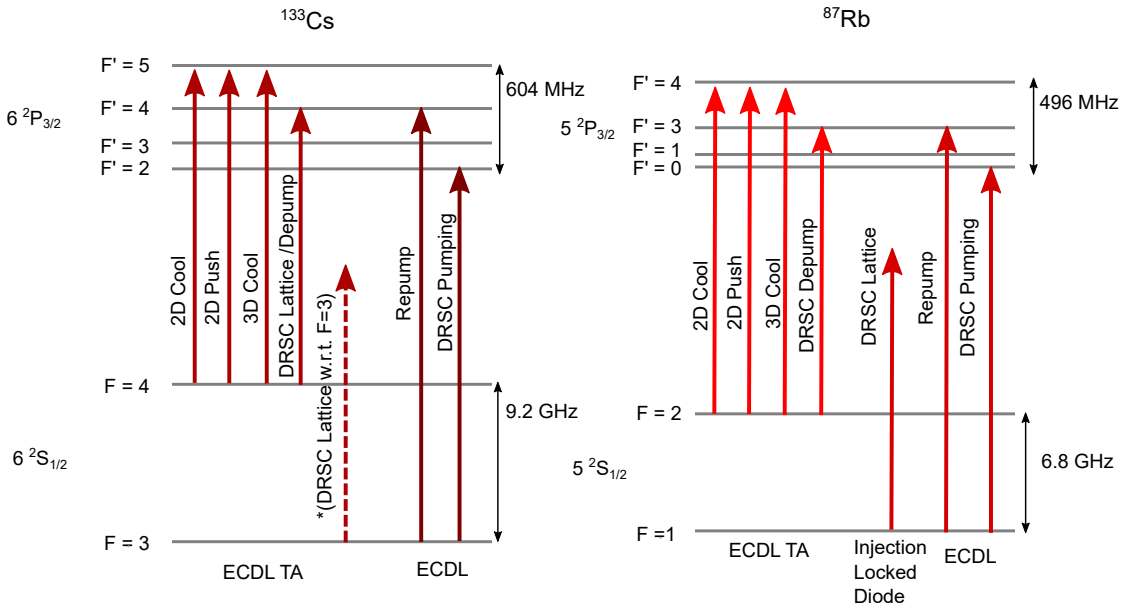

Figure 2.4: Overview of the laser cooling system. Each arrow represents an independent AOM-controlled beam. Within each manifold, the frequency splittings are to scale.

MOT Parameter	^{87}Rb Value	^{133}Cs Value
Total 2D Cooling Power (mW)	180	320
Total 3D Cooling Power (mW)	200.4	300
2D Cooling Detuning (MHz)	-21.7	-13.4
3D Cooling Detuning (MHz)	-12.9	-8.8
2D Push Power (mW)	40	4.5
2D Repump Power (mW)	21	7.2
3D Repump Power (mW)	14.1	11.1
2D Quad Field (G cm^{-1})	20	20
3D Quad Field (G cm^{-1})	7.6	12.6

Table 2.2: MOT Parameters

the two MOTs to avoid light-assisted collisions [128]. To achieve this we have separate control of the cooling beams for the two species.

Loading enough atoms into the 3D MOTs to saturate the later stages of cooling takes around 1 s for ^{133}Cs and 6 s for ^{87}Rb with the dispensers active. We monitor the MOT loading via measuring the fluorescence on two photodiodes one for each species. It is also possible to load the Cs MOT from the background vapour to preserve the dispensers, which takes around 10 s. After loading, we apply a short compressed MOT (cMOT) stage, where the field gradient is increased to 28 G cm^{-1}. This is required to improve the mode matching into the DRSC lattice. To reduce photon rescattering so that the atomic density can be increased, the detuning of the cooling light is increased simultaneously with the quad field ramp, to -2.7 Γ (-4.2Γ) for ^{133}Cs (^{87}Rb). During this step, we use the shim coils to move the cloud to the centre of the DRSC lattice. Recently we have investigated ways to further increase the density in the cMOT. By using a temporal dark MOT [152], where the repump power is ramped off during the cMOT, we gained a factor of 1.5 in the final atom number in the reservoir dipole trap for both species. The dark spot MOT is another technique that could help improve loading into the DRSC lattice [155].

After the cMOT phase, we null the magnetic field and perform optical molasses [65] as our first stage of sub-Dopplerr cooling. During the molasses, the detuning of the cooling light is ramped from the cMOT value to -11.7 Γ (-14Γ) for ^{133}Cs (^{87}Rb) to gradually reduce the molasses temperature. The final temperatures of the optical molasses are around 6 μK for ^{133}Cs and 10 μK for ^{87}Rb. We are not especially sensitive to this temperature as we perform additional sub-Doppler cooling, but the atomic density at this stage is crucial to realising high phase space density in the dipole trap.

2.4.2 DRSC

Degenerate Raman sideband cooling (DRSC) is a sub-Doppler cooling technique which is used to load the species into optical dipole traps by rapidly increasing the phase space density from the molasses value. This method is particularly attractive for two reasons. First, it naturally prepares the sample in the absolute hyperfine ground state, preventing

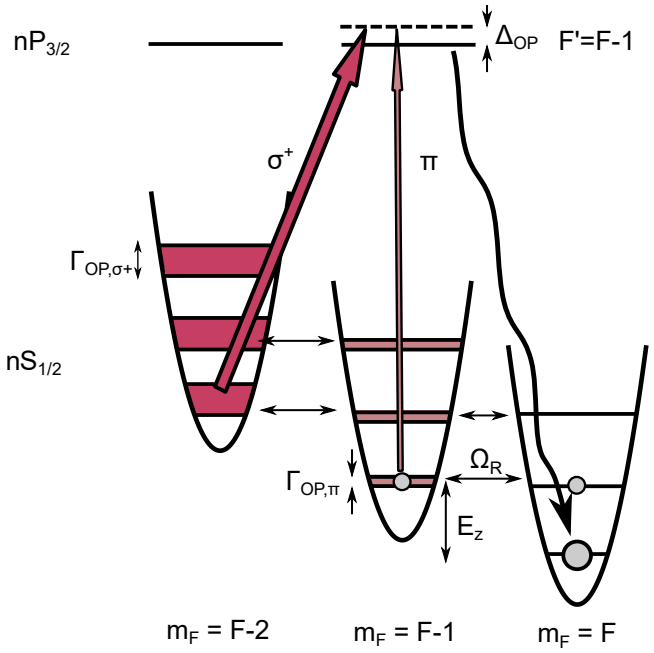

Figure 2.5: DRSC mechanism [152]. Atoms are trapped in a deep optical lattice where there are discrete harmonic oscillator levels, and a Zeeman shift E_z is applied so that different vibrational levels of the m_F states are degenerate. This allows for two-photon Raman transitions which coherently transfer population between these states at Ω_R. An optical pumping beam on the $F \rightarrow F-1$ transition is set up with polarisation so that it strongly pumps $m_F = F-2$ and weakly pumps $m_F = F-1$. Cooling is achieved as the atoms are progressively pumped into lower vibrational states, eventually into the dark state of $m_F = F$ and lowest vibrational level.

losses from spin-changing collisions in the dipole trap, which are especially strong in ^{133}Cs[7]. Second, the dipole trap loading is especially fast when compared to evaporation in a magnetic trap, which makes it attractive for quantum gas microscopy experiments which benefit from fast cycle times. In ^{133}Cs it is particularly straightforward to implement DRSC due to the large hyperfine ground state splitting compared to the D2 linewidth. This allows us to form the optical lattice with light resonant with the $F = 4$ hyperfine state, which prevents atoms from accumulating in the wrong state and uses a laser already required for the MOT stages.

The working principle of DRSC is illustrated in Figure 2.5, and consists of five key

[7]These inelastic collisions are discussed in more detail in Chapter 4

ingredients [152, 150]. (i) Atoms are trapped in a strong optical lattice, ideally strong enough that the harmonic level splitting is much larger than the recoil energy as expressed by the Lamb Dicke parameter $\eta = \frac{\hbar^2 k_{\text{cool}}^2}{2m}/\hbar\omega_{\text{trap}} \ll 1$. In this limit, spontaneous emission tends not to change the vibrational state of the atom. (ii) A small magnetic field is applied so that the Zeeman splitting between m_F sublevels matches the harmonic oscillator spacing. (iii) This degeneracy allows two-photon Raman transitions to change the vibrational level when they change the m_F state. These Raman transitions can be provided by the lattice if it has a finite helicity. (iv) An optical pumping beam can then be used to push the population into the lowest m_F state without changing the vibrational level (this beam is sometimes referred to as the polariser). This sets up a cooling cycle achieved via the combination of Raman transitions that change the motional state and the m_F optical pumping. It is the spontaneous emission from the optical pumping which carries away the entropy. (v) Finally as in the case of the MOT, we need to ensure that atoms don't accumulate in the other hyperfine F state, which in this case is the upper state. To achieve the required depumping we use light resonant with this level, e.g. $|F = 4\rangle \rightarrow |F' = 4\rangle$ for ^{133}Cs.

It is important that the optical pumping is performed on a $F \rightarrow F - 1$ transition. This allows two-stage cooling where the pumping beam polarization is set so that atoms in $m_F < F - 1$ experience a much faster optical pumping rate than $m_F = F - 1$. This allows us to have very strong cooling to rapidly capture atoms into the lattice, whilst simultaneously having weak coupling to allow clearly resolved sidebands in the final cooling steps and to reduce off-resonant coupling of the final dark state to other higher energy states. Another advantage is that the $F' = F - 1$ state cannot decay to the excited hyperfine ground state, and so the upper hyperfine state is only populated by off-resonant excitation.

The setup and optimisation of our DRSC was implemented closely following previous work in the Durham CsYb experiment [124]. Our lattice is generated by three orthogonal, linearly-polarised beams, one of which is retroreflected. Four interfering beams are required so that phase shifts between the beams only lead to global translation of the lattice without affecting the trap frequencies on the individual sites [120]. Each species has its own lattice, detuned around 10 GHz red of the lower hyperfine

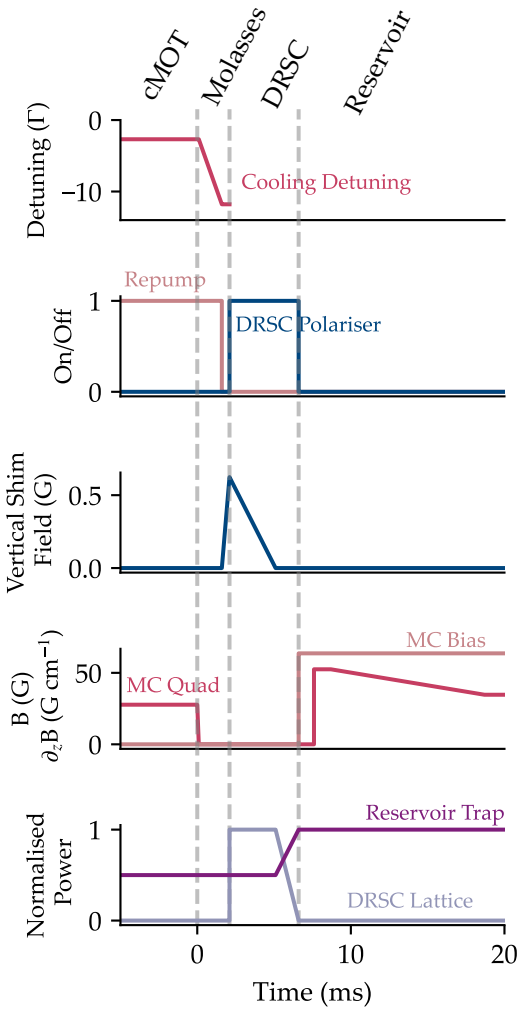

Figure 2.6: Sub-Doppler cooling timing sequence, illustrated for ^{133}Cs. (The ^{87}Rb and the dual-species sequences have a similar form.)

state D_2 line. By using near-detuned lattice beams it is straightforward to achieve the required Raman couplings [152].

We set the relative powers of the lattice beams to approximately balance the trap frequency anisotropy. The beams are delivered to the experiment with three fibres, each carrying both lattice wavelengths.

The optical pumping beam is circularly polarised and propagates downward through the chamber. To achieve the small π component the magnetic field is slightly tilted away from the beam axis.

The sequence for DRSC and the surrounding steps is illustrated in Figure 2.6. At the end of molasses, to prepare the atoms in the lower hyperfine state, the MOT repump light is turned off for 0.5 ms. The cooling process is started by extinguishing the molasses cooling light and quickly turning on the lattice and optical pumping beams. To take advantage of the free-space Raman cooling effect [152] we initially start the cooling with the magnetic field around twice the nominal value, before ramping the field to zero over 3 ms for ^{133}Cs or 10 ms for ^{87}Rb. Ramping the field during the cooling is observed to be optimal, presumably as it allows all the different lattice sites to be cooled despite their different resonance conditions. The difference in optimal times between the two species is probably due to differences in lattice trap frequency and is consistent with observations in other experiments [152].

At the end of DRSC, it is important to ramp the lattice off so that the atoms are adiabatically released, typically around 1.5 ms is required. The loading of the reservoir trap requires a short period of strong over-levitation to counteract the atoms falling during this ramp. This is discussed more in Section 2.6.

2.4.3 Laser system

The near-resonant laser system required for the laser cooling described above is fundamental to our experiment. Fortunately, over the two decades since the first BEC experiments, the basic laser cooling methods have become well established with commercial companies catering to the specific needs of most alkali experiments, and now many divalent atoms too. There is a trend towards simpler and more compact systems

such as 3D-printed distribution boards [191] and rack-mounted optical breadboards.

Our system is built in the more traditional way with a separate laser table for frequency and intensity control for all the near-resonant light and optical fibre connections to the main experiment table. The main complications arise from optical paths which require combinations of different wavelengths for two or more species.

For both species, we use one high-power laser to address the upper hyperfine ground state and another lower-power laser to address the lower hyperfine state. The high-power lasers are commercial extended cavity diode (ECDL) seeded tapered amplifiers[8], and the lower-power lasers are ECDLs[9]. We use a system of AOMs to reach the frequencies required for laser cooling, Figure 2.4 gives an overview of the system with each AOM path represented as an arrow. Additionally to what is currently used, the laser table is designed with space for a beam resonant at high fields around the ^{87}Rb-^{133}Cs Feshbach resonance near 180 G. Intensity control during the sequence is achieved via the AOMs and shutters[10].

The cooling lasers are frequency stabilised using saturated absorption spectroscopy [95] and a commercial digital PID laser controller[11]. This has proved to be a simple and robust method, it is rare that a laser unlocks over the course of a day's experiments.

2.5 Absorption imaging

Before discussing the trapping of atoms in the reservoir, I will make a brief aside to discuss how we detect the atoms once they have been cooled. Almost all the measurements in this thesis are performed using absorption imaging, which allows us to measure the number of atoms and momentum distribution of the cloud, which can be used to calculate the temperature of the gas. A full account of the method can be found in [153]. In our experiment, we image the shadow of the atomic cloud caused by resonant absorption of a short (65 µs) probe pulse on the D_2 cycling transition. To ensure that the

[8] Toptica TA Pro
[9] Toptica DL Pro
[10] SRS SR474, and homemade ones based on [319]
[11] Toptica DLC Pro

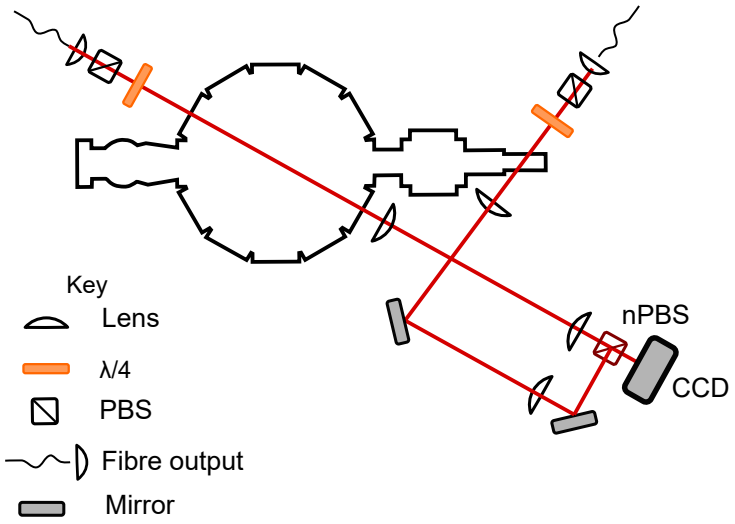

Figure 2.7: Optical layout for absorption imaging. A non-polarising beam splitter (nPBS) is used to combine the two imaging paths.

probe pulse drives σ^+ transitions we use circularly polarised light and apply a magnetic field along the beam using the shim coils. To prepare the atoms in the upper hyperfine manifold we use a 500 µs pulse of repump light. By taking a further two exposures, one with the probe and one with no probe to estimate the background we can extract the optical depth of the cloud. To calculate the atom number and cloud size from the optical depth the pixel size is calibrated by observing the atoms fall under gravity.

The optical setup used for absorption imaging is shown in Figure 2.7. To allow for imaging in both chambers without needing to make adjustments on the table we use a non-polarising beam splitter (nPBS) to combine two imaging paths. Each path uses a polarising beam splitter (PBS) and quarter waveplate to achieve circularly polarised probe light, and each imaging fibre carries light for both ^{87}Rb and ^{133}Cs. The atomic absorption is imaged by a lens pair, where the first lens is f away from the atoms and the second lens is f away from the CCD. Since the shadow is collimated in the space between these lenses the imaging is not especially sensitive to the distance between the lenses.

In many situations it is beneficial to apply a period of free expansion before imaging the atoms, this period is known as the time-of-flight (TOF) [153]. Varying the TOF

allows us to determine the temperature of the cloud, and can also be used to reduce the optical depth of the cloud to a value around 1 where absorption imaging is most reliable. To image with long TOF it is often necessary to apply a magnetic levitation field (as discussed in Section 2.6) to stop the cloud from falling out of the imaging field of view. This inflates the horizontal cloud size but the vertical cloud size is unaffected and can still be used to extract the temperature of the cloud. To ensure that any stray fields from eddy currents in the high current coils have decayed away we always turn off the levitation field at least 5 ms before imaging.

2.6 Reservoir Trap

After DRSC the atoms are cold enough to be captured in an optical dipole trap, an essential requirement for reaching BEC with ^{133}Cs, and for implementing optical transport. We follow previous experiments with ^{133}Cs [301, 165] and ^{87}Rb-^{133}Cs mixtures [173] and first load a large volume "reservoir" trap, formed by two beams with $1/e^2$ waist of 500 μm. The relatively large volume of this trap enables efficient capture of atoms from the DRSC lattice.

Due to its large volume, the reservoir trap is particularly susceptible to gravitational tilting, and so the atoms must be levitated using the magnetic field to keep them in the trap. Generally speaking, the conservative potential for an atom in a magnetic field $\mathbf{B}(\mathbf{r})$ and far off-resonant laser field $I_\lambda(\mathbf{r})$ can be written as [115]

$$U(\mathbf{r}) = -\mu \cdot \mathbf{B}(\mathbf{r}) - \frac{1}{2}\alpha_\lambda I_\lambda(\mathbf{r}) - mgz, \tag{2.3}$$

where μ denotes the magnetic moment of the atom and α_λ the real part of the polarisability at wavelength of the laser λ. A vertically offset quadrupole characterised by a vertical magnetic field with magnitude B_0 and gradient $\partial_z B$ creates a magnetic potential of the following form [124]

$$U_{\mathrm{mag}}(\mathbf{r}) = -(m_F g_F \mu_{\mathrm{B}} \partial_z B)z - \frac{1}{2}m\omega_{\mathrm{anti}}^2(x^2 + y^2), \tag{2.4}$$

where the anti-confining term arises from the requirement that $\nabla \cdot \mathbf{B} = 0$. In the case that the first term balances gravity $\omega_{\text{anti}} = g\sqrt{\frac{m}{3\mu_B B_0}}$, and so applying a large bias field is crucial to levitating the atoms. A fortunate feature of the ^{87}Rb-^{133}Cs mixture is that the field gradients required to levitate the species are almost identical (31.1 G cm^{-1} for ^{133}Cs and 30.5 G cm^{-1} for ^{87}Rb [145]).

The reservoir trap is formed from a 50W 1064nm fibre laser[12]. Thanks to the short coherence length of this laser we can form the cross trap in a bow-tie configuration where the same laser beam is directed through the chamber onto the atoms twice. This allows us to "recycle" the optical power.

The reservoir trap is loaded from the DRSC-cooled atoms by first over-levitating the atoms to counteract the acceleration of the atoms during the time the coils are turning on and the lattice is ramping off. We do this by initially ramping the quad field to 52 G cm^{-1}, before reducing the field to a value close to the levitation gradient (34 G cm^{-1}. We apply a large 60 G bias field to prevent magnetic anti-confinement reducing the trap depth in the horizontal plane. This also increases the collision rate for ^{133}Cs which enhances plain evaporation, as discussed in more detail in the context of the science cell evaporative cooling in chapter 4.

Typically with the species loaded individually, we trap around 1×10^7 atoms of either species after 750 ms of plain evaporation, at temperatures of 3 μK for ^{133}Cs and 6 μK for ^{87}Rb. Currently with both species loading at the same time we load around 6×10^6 of each species. The atom number reduction is mainly due to the mismatched DRSC times and the selective evaporation of ^{87}Rb, which is discussed in more detail in Chapter 4, Given the difficulties of the dual-species laser cooling, we are currently planning to take advantage of our optical transport method to temporally separate the loading of the two species. This is explained in more detail in Chapter 7.

[12] IPG YLR-50-LP

Chapter 3

Optical Transport Using a Moving Lattice

3.1 Introduction

As experiments on ultracold gases have become more advanced the requirements for optical and mechanical access around the atoms have increased. This is especially the case for quantum gas microscope experiments, which require a high-NA objective lens that takes up a significant solid angle around the cloud. Arranging all the necessary optics, coils and electrodes while maintaining the required vacuum and controlled electromagnetic environment can become a difficult task.

One way to solve the engineering challenge is to divide and conquer by spatially separating different parts of the sequence. Separation of the laser cooling stages from the final experiment and imaging system is an approach used in many labs and is achieved by moving ultracold atoms in a conservative potential. Around the time of the second generation of BEC experiments, the most common methods of ultracold atom transport were developed: a moving quadrupole coil pair [174], overlapping quadrupole coils [113] and translating the focus of a single beam dipole trap [123]. All of these methods require long transport times of order seconds, which can reduce the repetition rate of the experiment significantly. An alternative method, which has recently become more widely used, is to use a moving optical lattice [260, 203, 159, 12, 286], which allows

for faster atom transport.

In this chapter, I will detail the precise nature of our transport requirement and the solution we implemented based on a moving lattice formed by Gaussian beams with displaced foci. Our particular implementation of this method is novel in its simplicity and in its application to a dual-species mixture.

3.2 Methods for Transporting Ultracold Atoms

There are many established techniques for transporting atoms in the ultracold regime, each with its own pros and cons. Perhaps the most relevant considerations are: *simplicity*, the method should be easy to implement and maintain; *efficiency*, there should be minimal loss of phase space density due to transport and *speed*, transport should not hinder the experimental repetition rate.

Many experiments use a moving magnetic trap, achieved either with a sequence of overlapping coils [113] or simply by mounting a coil pair on a translation stage [174]. We did not seriously consider these options because the experiment was designed from the outset to use optical traps which are required for reaching BEC in ^{133}Cs. Our last sub-Doppler cooling method, Degenerate Raman Sideband Cooling (DRSC), naturally leaves the samples in the high field seeking stretched state. This means a separate stage of optical pumping would be required to use a magnetic trap. This combined with poor mode matching would lead to a significant loss in phase space density. It is also worth noting that the moving coil pair method is difficult to integrate with our plan for microscopy as we require an objective lens placed as close to the cell as possible to get the required resolution[1].

This leaves optical transport methods as the most viable options for our experiment. Here we can divide the existing methods into two sub-categories: dipole trap methods and lattice methods. In dipole trap methods the transport is achieved by moving the focus position of a tightly focused single laser beam, either using a translation stage[2]

[1] See chapter 6 for more details

[2] The vibration stability requirements on the stage for a moving optical trap are more stringent than for the moving quadrupole trap method. Air-bearing stages are commonly used.

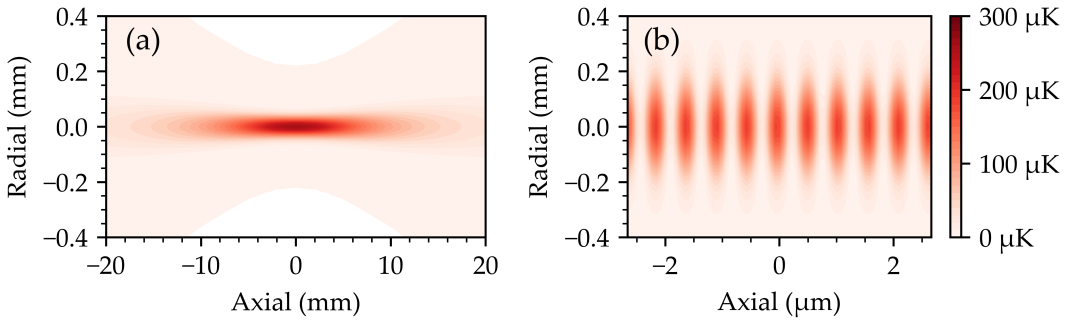

Figure 3.1: Optical potential for ^{133}Cs (a) a moving dipole trap (b) a moving lattice, the colour scale is the same on both plots and indicates -$U(\mathbf{r})$, where U is the potential. Note the very different axial confinement length scales, and hence different axial trapping frequencies. (a) shows a 4 W 50 μm 1064 nm beam, as used in focus tunable lens transport [172], (b) shows a lattice formed by two 20 W 200 μm 1064 nm beams, with 20cm offset foci, similar to what was used in our work.

[123, 284, 303, 60, 37] or in more recent iterations a focus tunable lens [172, 200, 288]. In the moving lattice method, two beams form an optical standing wave, and transport is achieved by shifting the standing wave via control over a frequency difference between the two beams [260]. The envelope of the standing wave determines the optical potential and is chosen such that the optical potential holds the atoms against gravity over the whole duration of the transport. Transport is achieved by slowly ramping on and off a frequency difference between the beams. The key difference between the two methods is the confinement of the cloud in the transport or axial direction. This is illustrated in Figure 3.1. In a moving focused beam, the trap is very elongated along the direction of transport, and typical trap frequencies are around 1 Hz. This leads to very long transport times, and poor mode-matching into crossed dipole traps which are used for evaporation. We anticipated that the long transport times at moderately high densities could cause large inelastic loss in ^{133}Cs and ^{87}Rb - ^{133}Cs mixtures, For example, for 1×10^7 ^{133}Cs atoms in a dipole trap similar to that used in [172], with $\omega_r = 1$ kHz and $\omega_z = 1$ Hz at a temperature of around 10 μK we would expect three-body loss lifetimes on the order of 2 s, which is similar to the transport time[3]. The ^{23}Na^{40}K experiment at MPQ has

[3]For more details on 3-body loss and how this lifetime is calculated, see Chapter 4

observed significant three-body loss in their moving dipole trap transport setup [79]. In moving lattice transport the axial trap frequency is considerably higher. This enables much faster transport, and at similar densities to our reservoir traps, and so lower three-body loss would be expected.

For our machine, we chose to use moving lattice transport, attracted by the possibility of fast transport times and lower three-body loss. Using this technique integrated well into our overall plan as the fibre amplifiers used for generating the quantum gas microscope lattices are the ideal tool for generating coherent lattice beams with a tuneable relative frequency. Another advantage of using a moving lattice is that we can avoid the technical complications of moving the focus of a beam: uncontrolled vibrations in the case of a translation stage or thermal lensing effects in a tunable lens.

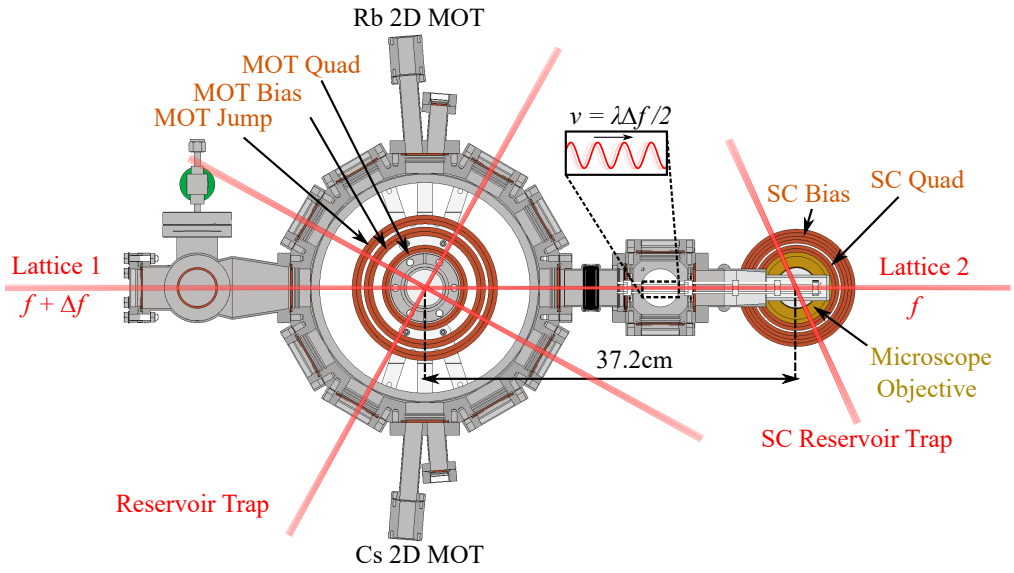

Figure 3.2: Vacuum schematic illustrating our transport requirement. Atoms are prepared in the reservoir trap in the MOT region and must be transported 37.2 cm to another trap in the science cell (SC) region within the field of view of our microscope objective. Coils which can be used to generate a magnetic levitation field are shown to scale.

3.3 Design of a Moving Lattice for Optical Transport

Moving lattice optical transport consists of two distinct technical challenges. First, the beams used must hold the atoms against gravity for the whole duration of transport, ideally with as little change to the trap geometry as possible and with good mode matching into the initial and final traps. Second, a scheme for smooth and fast frequency control of the lasers must be implemented.

3.3.1 Design Brief

Our optical transport problem is specific to the vacuum apparatus and atomic species used and is constrained by the laser systems available and control over the applied magnetic field which we have over the transport distance. Figure 3.2 shows a schematic of the vacuum system. The two regions of interest are separated by 37.2 cm. Magnetic levitation is possible in both regions using the coils shown. Atoms need to be transported between two optical "reservoir" traps, which are illustrated schematically.

The maximum trap volume of our transport trap is limited by available laser power. For quantum gas microscopy, we have a high power narrow linewidth 1064 nm laser system consisting of a 2 W NPRO[4] laser[5] and three 30 W low noise single frequency fibre amplifiers[6]. By using optical switches based on waveplates in motorised rotation mounts these amplifiers can be used for both the transport and the microscope lattices. It should be noted that the optical potentials will trap ^{133}Cs more strongly than ^{87}Rb, as the atomic polarisibilities at 1064 nm are different for the two species: $\alpha_{\mathrm{Cs,1064nm}}/\alpha_{\mathrm{Rb,1064nm}} = 1.69$.

3.3.2 Radial Trapping along Gaussian Beams

The main concern in designing a moving lattice for transport is ensuring that the lattice traps the cloud for the whole duration of the transport. In particular, we require the trapping force to be sufficient to hold the atoms against gravity.

[4]Non-planar Ring Oscillator, a form of crystal-based laser.
[5]Coherent Mephisto NPRO
[6]ALS-IR-1064-30-A-SF, Azurlight Systems

To design our lattice we first need an understanding of the trapping potential it will produce. In general, the optical potential for an atom is proportional to the wavelength-dependent polarisability α_λ and the intensity distribution $I_\lambda(\mathbf{r})$, specifically [115]

$$U(\mathbf{r}) = \frac{1}{2\varepsilon_0 c} Re\{\alpha_\lambda\} I_\lambda(\mathbf{r}). \tag{3.1}$$

The simplest optical lattices are formed by interfering the focused output of an optical fibre or laser known as a Gaussian beam[7] with either its retro-reflection or another Gaussian beam. The intensity distribution for a Gaussian beam propagating along a direction z is [115]

$$I(r,z) = I_0 \left(\frac{w_0}{w(z)}\right)^2 \exp\left(\frac{-2r^2}{w(z)^2}\right), \tag{3.2}$$

where the position dependent beam waist $w(z) = w_0\sqrt{1 + z/z_\mathrm{R}}$ with $z_\mathrm{R} = \pi w_0^2/\lambda$ and the peak intensity $I_0 = 2P/\pi w_0^2$ for a beam of power P and wavelength λ. All of this is assuming the beam is propagating through a material with refractive index $n = 1$. Note that the beam profile can be made elliptical rather than circular, but this is not considered in the following analysis for simplicity.

We can gain some insight into how to support atoms against gravity using our lattice beams by considering simply the case of a single Gaussian beam [285]. We can determine if the beam traps the atoms by comparing the maximum radial force from the trap to the gravitational force mg. By differentiating Eq. (3.1) for the case of a Gaussian beam given by Eq. (3.2) we find

$$F_r(z) = -8I_0 \left(\frac{w_0}{w(z)^3}\right)^2 \frac{\alpha r}{\varepsilon_0 c} \exp\left(-\frac{2r^2}{w(z)^2}\right). \tag{3.3}$$

The restoring force is maximal at $r = w(z)/2$ where

$$F_{r,\max} = -\frac{4}{\sqrt{e}c\varepsilon_0} \frac{w_0}{w(z)^2} \alpha \frac{2P}{\pi w_0^2}. \tag{3.4}$$

By comparing $F_{r,\max}$ to the gravitational force we can find the range of z for which the beam is able to hold atoms against gravity, as illustrated in Figure 3.3. The key message

[7] Technically, the intensity distribution of the TEM00 mode of the electric field in the laser cavity or fibre

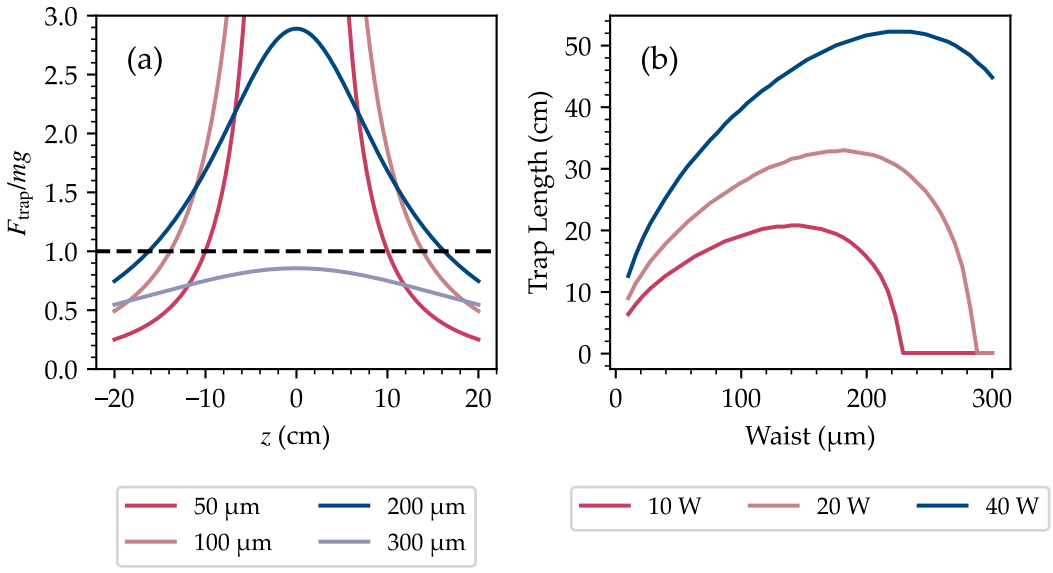

Figure 3.3: Range over which a Gaussian beam holds atoms against gravity. In (a) the ratio of the trapping force to the gravitational force is plotted for ^{87}Rb trapped in 20 W 1064 nm beams of various waists. For large waists, the trapping force is always too weak to counteract gravity, but for tightly focused beams the spreading of the beam at large propagation distances becomes significant. (b) shows the length over which $F_{\text{trap}}/mg > 1$ for ^{87}Rb trapped in 1064 nm beams of variable power and waist, demonstrating that the optimum waist for maximal trap length is weakly dependent on power in the beam.

of this toy model is that the beam waist, w_0, must be carefully chosen to balance between needing sufficiently tight confinement to trap against gravity, whilst not being so tightly focused that the beam diverges over the transport distance.

3.3.3 Optimised Lattice Trapping Potential

A more complete model is required to establish the viability of lattice transport. For this, we need to include the effect of applied magnetic levitation fields (which can be used to counteract the gravitational force at the two ends of the transport path) and calculate the optical lattice potential by including interference between the two lasers. We simulate the potential for the scenario illustrated in Figure 3.4 (a), where magnetic

levitation is applied in both regions, and we transport using a lattice formed by two Gaussian beams. For simplicity, we assume that the coils are kept on at the gradient which levitates the atoms in the centre of the coils for the duration of transport. The beam waist, w_0, and positions of the beam focus positions, z_0, are symmetric about the midpoint of the transport. The optimal w_0 and z_0 are found by brute force searching for the configuration with the highest minimum trap depth over the whole transport path. More details of these simulations can be found in Alex Matthies' thesis [195].

Figure 3.4 (b) shows the calculated trap depth and trap frequencies along the transport direction for the optimal parameters of $w_0 = 195\,\mu\text{m}$ and $z_0 = 7.2\,\text{cm}$ with 18W of power in each beam. We see that the trap depth is high for the whole duration of the transport, and so we expect to be able to transport atoms without them falling out of the trap.

Offsetting the beams along the transport direction is a novel technique and allows for trapping along the whole direction of the transport at achievable optical powers, without the need for the added complexity of Bessel beams used in [260, 159] or moving focus beams as used in [12].

3.3.4 Capturing transported atoms

An important aspect of optical transport is the loading and unloading of the transport trap to allow efficient evaporative cooling of the atoms. As discussed in Chapter 2 we first capture the atoms into a conservative optical trap after DRSC where the atoms are cold but dilute using a large volume reservoir trap.

Loading the lattice from the reservoir trap compresses the cloud radially but the cloud remains elongated in the axial direction and remains so during transport due to the lattice. To effectively transfer the transported atoms into a dipole trap we mode match the cloud by forming a trap from the transport beam focused closer to the science cell and a second beam from the 50 W fibre laser. This beam is focused onto the atoms with a cylindrical lens, producing a waist of 200 µm vertically and 500 µm horizontally. A rotation mount [237] is used to switch the fibre laser light between the paths, and the laser internal control can be used to ramp off the power during evaporation.

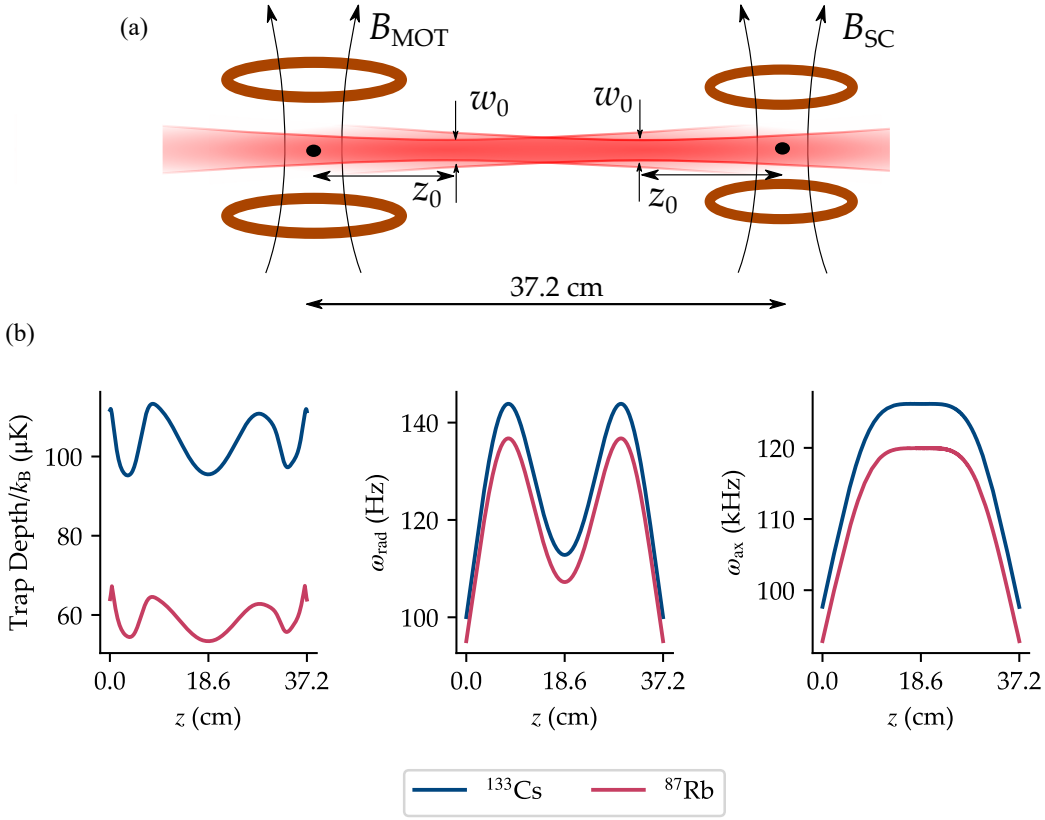

Figure 3.4: Calculated trap parameters for optimal transport lattice beam configuration. (a) shows an illustration of the beams and coils which contribute to the potential. The parameters w_0 and z_0 are optimised for the highest minimum trap depth, with the coils providing levitation at both ends of the chamber. (b) shows the calculated trap depth and frequencies for both species with $w_0 = 195\,\mu\mathrm{m}$ and $z_0 = 7.2\,\mathrm{cm}$ with 18W of power in each beam. The somewhat irregular shape of the trap depth-distance curve arises from changing magnetic force away from the centre of the coil pairs.

By using a beam with a horizontal waist similar to that used in the MOT chamber reservoir we can effectively transfer atoms into a dipole trap when the lattice is ramped off. Having a smaller vertical waist allows us to increase the depth and trap frequency of the trap which is helpful for ^{87}Rb. Similar techniques were used at LMU to transfer ^{133}Cs out of a moving lattice [158].

3.3.5 Frequency synthesis for optical transport

The second important aspect of the optical transport system is the frequency control of the two beams. It is crucial that care is taken to understand any relative phase noise between the two lattice beams, as this becomes shaking of the lattice when the beams interfere, as illustrated in Figure 3.5 (a). To understand this recall that the relative phase between the two beams determines the position of the lattice potential minima. In the harmonic approximation, the heating rate due to position noise in a trap of trap frequency ω is [256, 188]

$$\langle \dot{E} \rangle = \frac{\pi}{2} m\omega^4 S_x(\omega), \tag{3.5}$$

where $S_x(\omega)$ is the one-sided power spectrum of the position fluctuations caused by phase noise, i.e. $\int_0^\infty d\omega S_x(\omega) = \epsilon_x^2$ is the mean square variation in the lattice site position. For our high lattice trap frequencies this rate can become very high if there is large laser phase noise around 100 kHz offset from the carrier, which could come either from the laser itself or more likely from the RF modulation used to shift the lattice frequency. A secondary concern is achieving frequency modulation without any loss of power on the atoms.

Starting at the beginning of the signal chain, the first step to low relative phase noise of the transport beams is to derive them from the same narrow-linewidth laser. The seed laser we use[8] has very low phase noise, specified to be around 1 Hz/ $\sqrt{\text{Hz}}$ at 10 kHz offset from the carrier. We also use fibre amplifiers specifically chosen for their single-frequency performance.

To get the most power possible on the atoms we perform frequency modulation on the seed light before it is amplified by two separate fibre amplifiers, as illustrated in

[8] Coherent Mephisto NPRO.

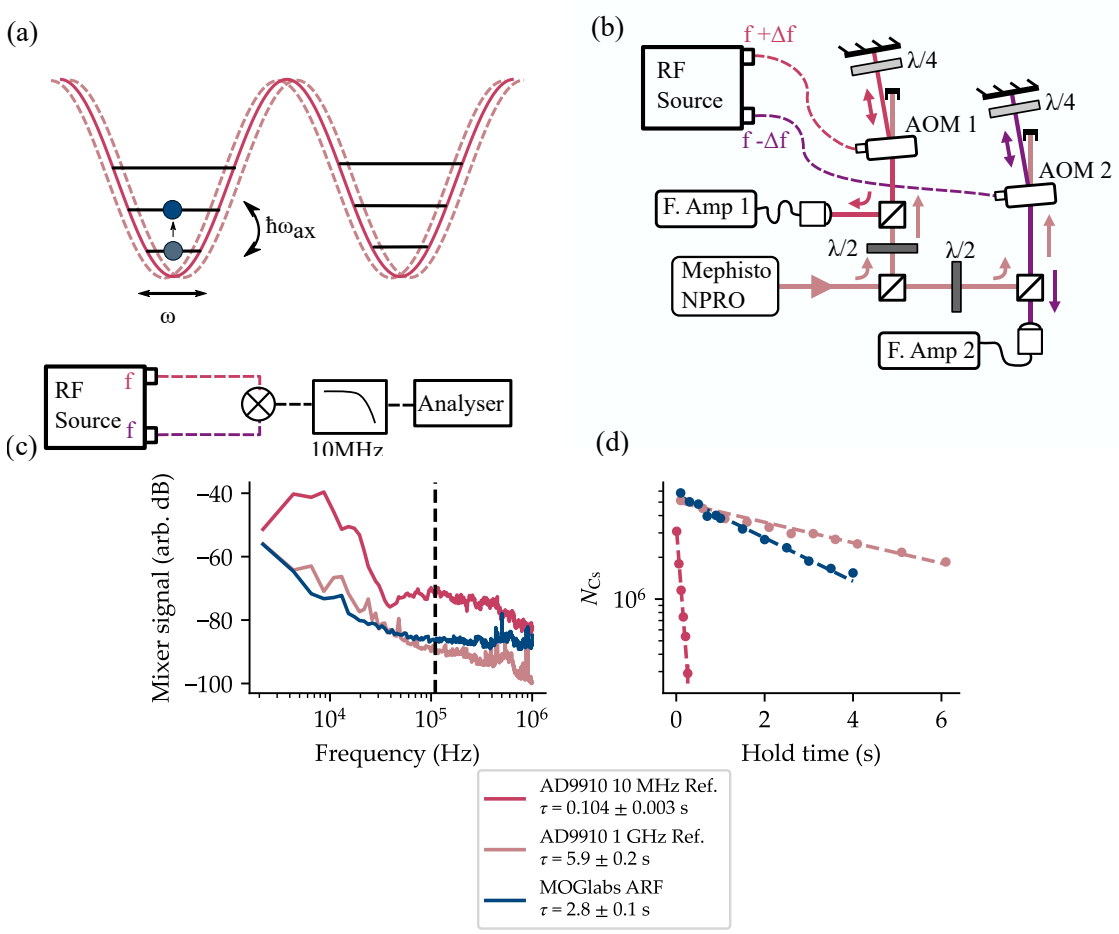

Figure 3.5: Frequency synthesis for moving lattice transport. (a) Phase noise between the two RF sources can lead to parametric heating in the lattice. (b) A schematic of the laser frequency modulation setup. The Mephisto seed laser is split using PBS cubes and then sent to two double-passed AOMs and coupled into optical fibres which seed two 30 W fibre amplifiers. (c) and (d) Comparing RF sources: (i) a pair of AD9910 DDS chips using the internal PLL reference multiplier, (ii) The same but bypassing the reference multiplier and supplying a 1 GHz clock externally, (iii) the MOGLabs ARF, where the outputs are phase synchronised. (c) A measurement of the relative phase noise of the two RF tones using a mixer. The y-axis is in arbitrary logarithmic units and the approximate axial trap frequency is highlighted with a dashed line. (d) Atom number decay in the transport lattice for the different RF sources. Lifetimes extracted from fitting to an exponential decay function, $N = N_0 \exp(-t/\tau)$, are shown in the legend.

Figure 3.5 (b). We use AOMs as these allow spatial separation of the modulated light from the carrier. The AOMs are arranged in a double pass configuration to maximise the available bandwidth of modulation, which sets the maximum speed of the moving lattice. The AOMs we use[9] have a bandwidth of 30 MHz. We found that by carefully setting the AOM angle it was possible to still seed the amplifiers with the seeds mutually detuned by 100 MHz, corresponding to a peak velocity of $\lambda\Delta f/2 = 53\,\mathrm{m/s}$. The fibre amplifiers are operated in a saturated regime and are therefore insensitive to variation in seed power. In practice, the minimum seed power, and hence maximum detuning, is limited by an inbuilt shut-off mechanism which activates if the seed power is approaching a value too low to saturate the gain process. The fibre amplifier also requires the seed light to be continuously on during operation, so the system cannot tolerate even micro-second scale dropouts in the RF used to drive the frequency control AOMs.

As well as phase noise, another concern is the agility with which the RF modulation can be performed. If the modulation is performed in discrete steps, it is important that the digitisation frequency is much higher than the lattice trap frequencies [132] to avoid parametric heating due to aliasing. Our high lattice frequencies require the digitisation frequency to be at least 150 kHz, which rules out many frequency generators. Typically in optical transport trajectories are chosen where the acceleration on the atoms is ramped on with no discontinuities, for example, sinusoidal [132] or "minimum jerk" trajectories [185]. This requires arbitrary frequency modulation, typically achieved by loading data for the frequency generator from a look-up table. If the ramp is loaded from memory, as in most arbitrary waveform generators, then the memory size limits the maximum digitisation frequency for a given ramp profile and hence sets a minimum speed at which we can transport atoms.

Initially, a homemade RF synthesiser was developed, based on a pair of direct digital synthesis (DDS) chips[10] with arbitrary modulation controlled by an FPGA[11]. Using a DDS based frequency synthesiser allows for changing the relative detuning of the lattice beams in steps that are faster than the axial trap frequency, which is essential

[9] ISOMET M1080-T80L-1.5
[10] AD9910
[11] DE0 Nano Cyclone IV Development Board

to avoid heating. Using an FPGA to deliver data to the DDS allows longer arbitrary frequency ramps, as the FPGA board's 32 MB RAM chip is larger than the AD9910's 4MB onboard memory.

During development, there were two issues with this system. First, the internal reference multiplier of the AD9910 chip introduces a large amount of phase noise which was very detrimental to the lifetime in the lattice[12]. The AD9910 DDS operates on a 1 GHz clock, which can be supplied by either an internal reference multiplier working from e.g. 10 MHz GPS signal or an external 1 GHz signal. So the solution is simply to bypass the internal clock and provide the same good 1 GHz clock signal[13] to both DDS chips. This is illustrated in Figure 3.5. In (c) we make a comparative measurement of the relative phase noise of our synthesiser with the two clock options, and commercial synthesiser for comparison. In (d) the lifetime in the static lattice is demonstrated by loading atoms from the reservoir and holding them for a variable amount of time with the double-passed AOMs provided with RF from the various sources. We see a clear correlation between the relative phase noise at the axial trap frequency and the atomic lifetime. Supplying an external 1GHz clock signal significantly improved the relative phase noise.

A more involved problem was that the transport performance with the homemade synthesiser was very variable from shot to shot. We assumed this was due to additional phase noise during the modulation, perhaps associated with asynchronous data transfer between the FPGA and the DDS. To make progress we switched to using a commercial MOGLabs ARF frequency generator. The basic design of the MOGLabs ARF is very similar to the homemade synthesiser, bar a few improvements to the digital architecture to synchronise the DDS outputs. The only technical disadvantage of the MOGLabs ARF is the lower modulation memory of 8191 instructions. Another option would be to use the DDS internal ramp generator [12], however, this only allows for linear frequency ramps.

[12] Similar behaviour has been seen in other groups using this DDS [160].
[13] e.g. AD9520 VCO or a crystal oscillator

3.4 Characterisation and optimisation

Having discussed the design of the transport lattice and how we implement the frequency control this next section details the implementation and the characterisation of the transport technique.

3.4.1 Optical Setup

The optical layout for the transport laser system is illustrated in Figure 3.6. Both fibre amplifiers are mounted level with the vacuum system to avoid the use of periscopes with the high-power beams. High-power tolerant Faraday isolators[14] are used to ensure that the counter-propagating lattice beam doesn't cause damage to the opposing laser output. To allow optical access for the co-propagating microscope lattice beam we use PBS cubes close to the chamber.

The power in the transport beams is controlled using motorised $\lambda/2$ waveplates based on a hollow stepper motor [237, 254]. These allow the lattice power to be ramped on smoothly, with a minimum ramp time of around 20 ms. Avoiding the use of AOMs in the lattice path allows us to get around 15% more power to the atoms, and avoids thermal lensing from the AOM crystal [268].

To turn off the lattice completely we use homemade shutters. These consist of a small mirror attached to a spring-loaded solenoid that diverts the beam down to a water-cooled beam dump. These block the beam with an 80-20 fall time of less than 1 ms, with a somewhat variable $\approx$ 10 ms delay from the trigger. The shutters are mounted on vibration-isolating rubber to avoid disturbance to the experiment. A technical drawback of using the moving waveplates and shutters to control the lattice is that we cannot perform TOF imaging with precise timing, which makes measuring the temperature of the cloud in the lattice difficult.

To set the beam size and position in the chamber, each beam has lenses which were designed to give the desired waists and positions determined by the simulation of the trapping potential. By using a beam profiling camera on the monitoring path we were

[14] EOT Pavos

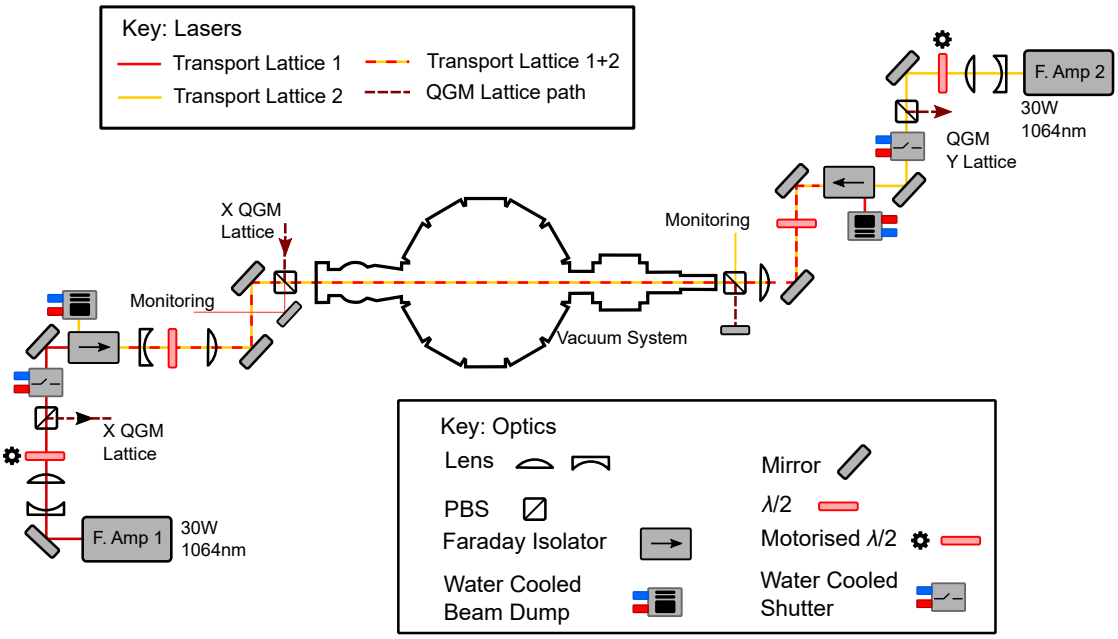

Figure 3.6: Optical layout for the transport lattice. Control over the beams is provided by motorised waveplates and shutters. Water cooling is used on beam dumps and shutters to avoid thermal transients on the table. To allow optical access for the co-propagating microscope lattice beam we have PBS cubes close to the chamber. Monitoring of the beam positions is done via a low-intensity reflection off these PBS cubes.

able to set these to an accuracy of around 10%. The angular alignment of the two transport beams is very sensitive, as the beams need to be co-propagating to within around 100 µm over a distance of 37.2 cm. For ease of realignment, we monitor the position of the lattice beams using inexpensive cameras[15].

Initial optimisation of transport was done by moving the atoms a small distance away and then back into the MOT chamber for imaging. Once the beams were overlapped enough to transport the full distance, final optimisation was achieved via maximising the atom number in the lattice measured by absorption imaging in the science cell. This process is reported in detail in [195].

[15] Raspberry Pi Camera Module V2.1

3.4.2 Sequence for loading and transport

We load the lattice from the main chamber reservoir trap described in Chapter 2. First, the Transport 1 beam is ramped on in 50 ms to compress the cloud before the lattice is adiabatically ramped on by increasing the power in the Transport 2 beam over 100 ms. We found that ramping on the lattice in times less than 100 ms caused significant heating.

To transport the atoms we upload a frequency lookup table to the MOGLabs ARF. The synthesiser steps through the table when triggered by the experiment control system using a TTL. We compared velocity ramp shapes of various kinds, the two compared in the data shown are the "linear" and "minimum jerk" trajectories, given as

$$v_{\text{linear}}(t) = \begin{cases} \frac{d}{T}\left(2\left(\frac{t}{T}\right)\right) & t < T/2 \\ \frac{d}{T}\left(2\left(1-\frac{t}{T}\right)\right) & t \geq T/2 \end{cases} \tag{3.6}$$

$$v_{\text{MinJerk}}(t) = \frac{d}{T}\left(30\left(\frac{t}{T}\right)^2 - 60\left(\frac{t}{T}\right)^3 + 30\left(\frac{t}{T}\right)^4\right). \tag{3.7}$$

where d is the transport distance and T is the total duration of the tramp. These are illustrated for $d = 37.2$ cm (the distance used in our experiment) and $T = 30$ ms in Figure

The linear trajectory is the most common in moving lattice transport due to its technical simplicity [262, 159, 12], however, smoothed transport trajectories have been found to be more effective in some cases [132, 185], and we found significant improvement when using the minimum jerk trajectory. We also investigated other forms of smoothed trajectory, but found little practical difference between them, for more details see [195].

3.4.3 Characterisation

The key results of our characterisation are shown in Figure 3.8. In these measurements to measure the effectiveness of transport we simply measure the number of atoms in the lattice in the science cell. For both species, the number of atoms loaded into the lattice

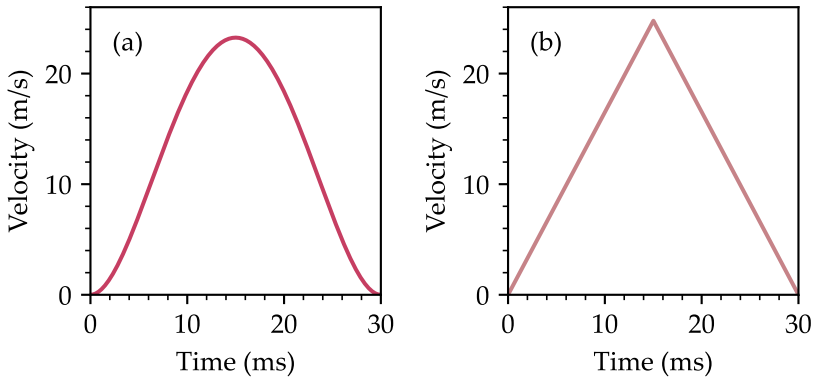

Figure 3.7: Transport velocity trajectories, as defined in Eq. (3.6) and Eq. (3.7) (a) Minimum Jerk Trajectory (b) Linear trajectory.

was around 9×10^6. It should be noted that the lattice beam alignment was re-optimised between data sets (a) vs. (b) and (c) due to a change in the beam shape of one of the fibre amplifiers, and hence the data sets have different peak efficiencies.

First, we compare different frequency ramp shapes and timescales. We vary both the time scale of the ramp, which we plot as the peak acceleration, and also the shape of the profile. The data show that for both ramp types there is an approximately linear reduction in transported atom number with increasing peak acceleration beyond a critical peak acceleration. There is also a significant improvement in transport efficiency with the smooth ramp compared to the linear velocity ramp, especially at large peak accelerations. This leads us to propose that the drop in efficiency at large accelerations is associated with the force on the cloud being too sudden. An alternative explanation may be that at short ramp times, there is a parametric heating resonance as the radial trap frequency, ω_{rad}, varies along the beams as is shown in Figure 3.4. Practically speaking we simply perform transport at low peak accelerations, less than $5\,\mathrm{km/s^2}$, corresponding to around 25 ms transport time.

As mentioned earlier, the digitisation of the frequency modulation is expected to cause heating when the frequency is less than the axial trap frequency, ω_{ax}. This is clearly seen in the data plotted in (b), where we vary the digitisation frequency for minimum jerk ramps of different durations. Increased loss is observed for all ramps with

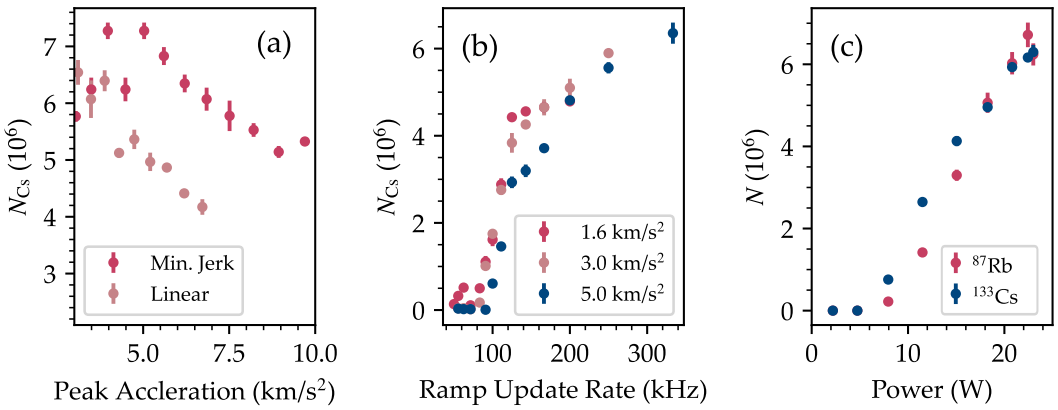

Figure 3.8: Characterisation of moving lattice transport: the atom number as measured in the transport lattice in the Science cell is plotted to give a metric of the effectiveness of transport. Typically we loaded around 1×10^7 atoms into the lattice in the main chamber for either species in these measurements. (a) Different ramp types and varying speeds, plotted as peak acceleration. (b) Changing the frequency ramp digitisation frequency or DDS update rate for minimum-jerk ramps of various speeds. (c) Changing the power in the lattice beams, plotted for both species. For a full discussion of these results see the main text.

digitisation frequencies below 100 kHz, roughly as expected from our simulations of the trap frequency and previous experiments which have investigated this effect [132]. Beyond 250 kHz we see little further improvement in transport efficiency with increasing digitisation frequency, indicating that this is no longer a cause for concern. Working at a minimum digitisation frequency of 250 kHz limits efficient transport to ramps which have a maximum duration of 33 ms. The competition of the loss at large transport accelerations with the limit on update rate at long ramp durations leads to an optimal range of ramp durations between 23 ms and 28 ms.

The data in (c) show the effect of simultaneously varying the power in the lattice beams. As expected we find that high optical trap depth from high laser power is crucial to transport, especially for ^{87}Rb with its lower polarisibility. Extrapolating the trend in the data implies that more power in the laser beams would lead to an improvement in transport efficiency.

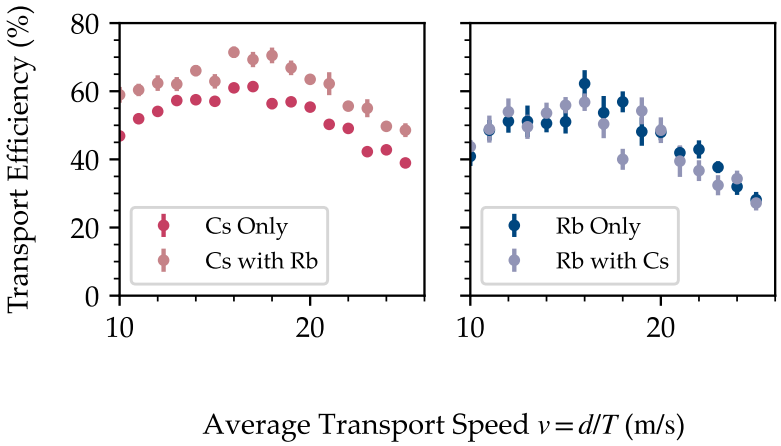

Figure 3.9: Dual species transport. These data compare the transport efficiency of each species with and without the other species.

Since in moving lattice transport the densities are relatively low and the duration of transport is fast, we expect that the role of collisions during transport should be negligible. We tested this hypothesis by transporting both species in the same sequence. The results are shown in Figure 3.9. We use a dual-species sequence optimised in favour of ^{87}Rb. To isolate the effect of the transport part of the sequence, we compare transport efficiency defined as the ratio of atom numbers in the lattice in the MC and SC. Also plotted for comparison are data from the single species sequences used in the characterisation measurements above.

As expected, we find minimal difference in the atomic loss during the transport part of the sequence. The increased transport efficiency of Cs in the presence of Rb could be due to sympathetic cooling in the reservoir trap or the smaller atom numbers loaded in the dual-species sequence. It is worth noting however that the effectiveness of transport as a whole requires good loading into and out of the lattice into the dipole trap in the science cell. Both of these steps are made inefficient by interspecies collisions, as is discussed in detail below.

3.4.4 Transfer to the SC reservoir

To load the SC reservoir we follow a sequence which is approximately the reverse of that used to load the transport lattice.

First, the SC reservoir beam (shown schematically in Figure 3.2) is ramped up in 50 ms to 20 W. The atoms are released from the lattice by ramping off the Transport 1 beam in 100 ms, leaving them in a cross trap formed by the Transport 2 beam and the SC reservoir beam. As in the MC reservoir, a magnetic levitation field is applied, and to reduce magnetic anti-confinement a 40 G bias field is used. This has the added benefit of increasing the ^{133}Cs scattering length which improves the rate of thermalisation into the new trap. This trap has a depth of around $U_0 = 40\,\mu\text{K}$ and mean trap frequency of $\bar{\omega} = 70\,\text{Hz}$ for ^{133}Cs. After 500 ms thermalisation time around 2.5×10^6 atoms of ^{133}Cs and 1×10^6 ^{87}Rb remain in the trap. The lower numbers compared to the MC reservoir (around 1×10^7 for both) and the number loaded into the lattice (around 9×10^6 for both) imply that there is still some heating involved in the transport and/or inefficient transfer of atoms.

The loading of the SC reservoir with ^{87}Rb is particularly hampered by the combination of low polarisability and low scattering length leading to very inefficient evaporation of atoms (the process of evaporation is discussed in detail in Chapter 4). The situation is even worse in the dual-species sequence where ^{87}Rb acts as a sympathetic coolant for ^{133}Cs [173, 197]. We propose to avoid this interspecies loss by implementing a sequential loading scheme where ^{87}Rb is cooled and transported first, then moved out of the transport path using a moving dipole trap. ^{133}Cs can then be cooled and transported while ^{87}Rb evaporates in the science cell, ready to be merged following the method described in [173]. This idea is discussed in more detail in Chapter 7. To improve the transfer out of the trap we are planning to compress the ^{87}Rb cloud further using an additional beam in the main chamber, which should increase the density and hence collision rate when loading out of the lattice in the science cell.

Despite these challenges, the current transport setup has enabled us to make use of the science cell for further progress towards quantum gas microscopy of atoms and ultimately molecules. After establishing optical transport we worked on further cooling

of the atoms towards quantum degeneracy, as is detailed in the following chapter.

Chapter 4

Bose-Einstein Condensates of ^{133}Cs and ^{87}Rb in the Science Cell

4.1 Introduction

To prepare low entropy samples of atoms or molecules for microscopy experiments it is crucial to cool them as much as possible before loading them into the optical lattice. To be exact, we need to reduce temperature while maintaining a high density of particles. In experiments with bosonic atoms, crossing the Bose-Einstein Condensate (BEC) phase transition is the key benchmark of success. Producing a pure BEC is as close as these experiments can get to realising the theoretical concept of a T = 0 state. By implementing adiabatic transformations of the system Hamiltonian, these cold samples can be used as a starting point for the study of quantum phase transitions, quench dynamics and quantum simulation more generally.

This chapter details how we achieve condensation for ^{87}Rb and ^{133}Cs using the process of evaporative cooling. After a brief theoretical introduction and an overview of the established method, we discuss the design of the optical traps we use and the optimisation of the experimental sequence. Reaching the BEC transition with our transported atoms was a key technical milestone on our route towards experiments on quantum many-body physics with these atoms and eventually molecules.

4.2 Quantum Statistics in Gases

4.2.1 A Historical Introduction

The Bose-Einstein Condensate (BEC) is a phase of the ideal gas which emerges when statistical mechanics is formulated in a way consistent with two requirements of quantum theory. First, the phase-space (i.e. the allowable atomic positions and momenta) must be quantised, and not continuous. Second, all the atoms in the gas must be treated as indistinguishable particles. Although somewhat counter-intuitive, both of these new postulates solved important problems with the old classical theory. Quantisation was the key step in the discovery of Planck's Law, which solved the ultraviolet catastrophe, and indistinguishability was needed to understand the Gibbs Paradox in statistical mechanics[1].

Taking these new ideas together, Bose and Einstein developed a new quantum theory of the ideal gas, well before any notion of modern quantum mechanics was established. Their formulation predicted a new phase of matter, where every indistinguishable particle occupied the same quantum state at very low temperatures. Although their model is only a crude approximation to other low-temperature phenomena such as superfluidity in ^{4}He and superconductivity, it is a very good model of ultracold gases which are much more dilute and therefore better approximated as ideal gases.

4.2.2 Condensation as the Saturation of Quantised phase-space

The most straightforward formulation of Bose-Einstein statistics is in the grand canonical ensemble, where we consider the system in thermal contact with a reservoir at temperature T with which it can exchange particles at chemical potential μ. For these results in more detail the reader can refer to [54].

In this setting we can use statistical mechanics [27] to find the following expression for the occupation probability N_i for a state i with energy ε_i,

[1]For a detailed account of the early history of the theory of BEC, the reader can refer to e.g. [255]

$$N_i = \frac{1}{e^{\beta(\varepsilon_i - \mu)} - 1}, \tag{4.1}$$

where $\beta = 1/k_B T$. The value of μ is determined by the total number of atoms in the system, which is given by

$$N = \sum_i g_i N_i = \sum_i \frac{g_i}{e^{\beta(\varepsilon_i - \mu)} - 1}, \tag{4.2}$$

where g_i is the degeneracy of the energy level ε_i. To have a finite number of particles $\mu \leq 0$. Often the calculations are simpler if we replace μ by the fugacity $z = e^{\beta\mu}$, where $0 \leq z \leq 1$[2].

As expected, in the classical limit where each individual state has a very low occupation probability, we recover the familiar Gibbs (or Boltzmann) factor

$$N_i = e^{-\beta(\varepsilon_i - \mu)}, \text{ where } \beta(\varepsilon_i - \mu) \gg 1. \tag{4.3}$$

However, if we consider $\lim z \to 1$, we have very different behaviour; to see this clearly we can separate the sum for N into two parts:

$$N = \frac{z}{1 - z} + \sum_{i \neq 0} g_i \frac{z}{e^{\beta\varepsilon_i} - z}. \tag{4.4}$$

Evidently, the ground state population is going to become very large as z approaches 1. For certain systems, the maximum occupation of the other states saturates at finite T. The behaviour of the sum in Eqn. 4.4 is determined by the geometry of the trap via g_i. E.g. for a 3D box potential the sum converges, whereas for a 2D box potential the sum does not. In the situation that the sum in Eqn. 4.4 is finite, any extra particles must go into the ground state, and so it can become macroscopically occupied[3]. The atoms piled up in the ground state are known as the condensate, and the other remaining atoms as the "thermal fraction".

[2] An energy offset such that $\varepsilon_0 = 0$ is assumed.

[3] Even in dilute gases the picture of "saturation" of the excited states is modified by interactions [281] but this analysis still holds in a qualitative way.

To make this explicit, we can evaluate N for a case which is especially relevant to our experiment: a 3D harmonic trap. Working in the limit[4] $\hbar\omega \ll k_B T$, we can use the density of states $g(\varepsilon) = \varepsilon^2/(2(\hbar\omega)^3$ and excluding the ground state we find:

$$\begin{aligned} N &= \int_0^\infty d\varepsilon f(\varepsilon) g(\varepsilon) \\ &= \frac{1}{2(\hbar\omega)^3} \int_0^\infty d\varepsilon \frac{\varepsilon^2 z}{e^{\beta(\varepsilon)} - z} \\ &= \frac{(kT)^3}{(\hbar\omega)^3} Li_3(z), \text{ where } Li_3(z) = \sum_l^\infty \frac{z^l}{l^3}. \end{aligned}$$

Note that $Li_3(1) = 1.202$, and so we find the maximum occupation of the thermal states to be

$$N_{\max} = 1.202 \left(\frac{k_B T}{\hbar\omega} \right)^3. \tag{4.5}$$

Note that the condensation phenomenon occurs at a critical value of the classical peak phase-space density, $\rho_0 = N(\hbar\omega/k_B T)^3$. If we want to create a BEC we thus need to compress the gas into a smaller volume of phase space.

It is interesting to note that the accessible volume of phase space is directly proportional to the entropy of the trapped gas via the Boltzman postulate, sometimes expressed as $S = k_B \ln \Delta\Gamma$, where $\Delta\Gamma$ is the statistical weight and is proportional to the phase space volume of the system (See Section 1.7 of [170]). Thus to force a whole cloud to condense we need to decrease its entropy, so operations which reduce the temperature adiabatically cannot cause a cloud to cross the BEC transition[5].

4.3 Evaporative cooling

In this section, we will look at how BEC is achieved in practice and the particular quirks of ^{87}Rb and ^{133}Cs that need to be taken into account in the design and optimisation of our machine.

[4] Looking ahead to the result in Eqn. 4.5 we see this is indeed a valid approximation if N is large.

[5] It is, however, possible to reversibly cross the BEC transition in a sub-volume of a trapped gas by "concentrating" phase space density without changing the total entropy of the trapped gas [274].

The second law of thermodynamics prevents any decrease in the entropy of a closed system. As discussed earlier, there are many techniques for cooling atoms via resonant laser fields, where the randomly scattered photons carry away entropy. However, these methods are fundamentally limited in the lowest temperature they can reach due to the random velocity kicks from photon recoil. This is quantified by the recoil temperature $kT_{rec} = \frac{\hbar^2 k_{cool}^2}{2m}$, where the relevant wavelength is the species' cooling transition. For reference, these are 0.1 μK for Cs, and 0.18 μK for Rb for the D2 wavelengths of 852 nm and 780 nm respectively. The high densities required for condensation here are difficult to realise, and only recently has BEC of any species been achieved via laser cooling alone [289].

Fortunately, cooling can continue beyond the recoil limit if we allow atoms to leave the system. If atoms with higher than average energy are selectively removed, then the entropy of the sample can decrease. This effect is known as evaporative cooling [131] and was crucial to the first observations of BEC in the 1990s [6, 70].

4.3.1 Basic principle of evaporation

The basic principle of evaporative cooling is illustrated in Figure 4.1, adapted from [54]. Working in an energy state picture, each atom in the trap occupies some energy state E_n and, in the absence of collisions, this would stay the same for all time. The situation is changed via elastic collisions which redistribute particles among energy states. In this case, with a finite trap depth, it becomes possible for atoms to be lost from the trap after an elastic collision, if the larger final energy $E_f > U_0$. This irreversibly carries away energy from the trapped sample, causing a cooling effect and increased phase-space density.

To prove that this removal of atoms increases phase-space density, we can consider a simple equilibrium argument, where we consider evaporation in steps of truncation and re-thermalisation [69]. A single evaporation step involves the sudden removal of any atoms with energy greater than the trap depth, i.e. truncation of the thermal distribution at an energy $U_0 = \eta k_B T$ where we have defined the truncation parameter η, which we assume to be of order 10 so that the number of atoms lost in each step, dN, is small.

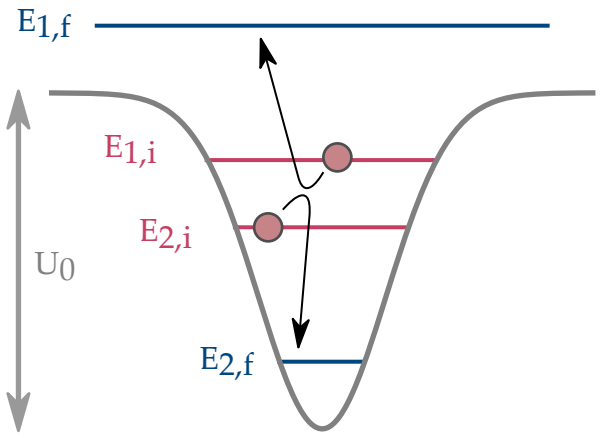

Figure 4.1: Evaporative cooling requires elastic collisions. Consider two atoms in initial energy states $E_{1,i}$,$E_{2,i}$. After an elastic collision, atom 1 gains energy from atom 2, with $E_{1,i} + E_{2,i} = E_{1,f} + E_{2,f}$. If $E_{1,f} > U_0$ then the atom is lost from the trap, and the mean energy of the atoms in the trap decreases, causing a cooling effect.

These atoms have a mean energy slightly larger than U_0, which we will refer to as $(\eta + \kappa)k_BT$. The extra energy κ is small, of order 1 [190]. Recalling the equipartition result for the energy-temperature relation for a 3D harmonically trapped ideal gas, $E = 3Nk_BT$, we can compare the equilibrium before and after truncation and thermalisation. Working to first order we find:

$$3k_B(N - dN)(T - dT) = 3Nk_BT - (\eta + \kappa)k_BTdN$$
$$\frac{dT}{T} = \frac{\eta + \kappa - 3}{3}\frac{dN}{N}$$

From this we can derive many more scaling laws, crucially we find that the peak phase-space density, ρ_0, and the elastic collision rate, Γ_{el}, scale as

$$\rho_0 = N\left(\frac{\hbar\omega}{k_B T}\right)^3 \propto N^{4-(\eta+\kappa)} \tag{4.6}$$

$$\Gamma_{el} = n\sigma v \propto N^{2-(\eta+\kappa)/3} \tag{4.7}$$

This highlights that phase-space density increase only takes place at high enough η, and shows that for very high η the collision rate can increase as evaporation proceeds, leading to what is termed "runaway" evaporation. Recall that the scattering cross section is given by $\sigma = 8\pi a_s^2$ for bosons in the ultracold regime, and can be controlled via a magnetic Feshbach resonance in certain species. Eqn. 4.6 implies we could define the efficiency of evaporation as:

$$\gamma = \frac{d\ln\rho}{d\ln N}. \tag{4.8}$$

4.3.2 Kinetics and Forced Evaporation

Eqn. 4.6 implies that evaporative cooling is most efficient in the limit of very large $\eta = \frac{k_B T}{U_0}$, however, we have neglected the time scale on which these cycles of evaporation and thermalisation take place. If the process is too slow, the experimental repetition rate is hindered, and other heating processes can dominate and limit the maximum ρ_0.

Using Boltzmann's kinetic theory it is possible to calculate the time scale over which evaporation happens analytically [190, 246]. These references derive the following simple expression for the evaporation rate in the limit $\eta \gg 1$, which is valid above $\eta > 5$:

$$\frac{\dot{N}}{N} = -\Gamma_{el}(\eta - 4)e^{-\eta}. \tag{4.9}$$

As expected the evaporation rate depends linearly on the number of collisions, however, the fraction of collisions which can leave the trap is exponentially suppressed in η. In practice, this leads to the temperature settling to a value around $T \approx U_0/(10k_B)$ in most situations where atoms are held in a trap. Settling to this value is sometimes known as "thermalising" with the trap. Further cooling requires lowering the trap depth and is known as forced evaporation.

Exactly how the evaporation is forced depends on the trap involved. In magnetic traps, an RF transition can be used to selectively remove the hottest atoms independently

of the shape of the trap. This is very effective as the rate of elastic collisions can be kept high while selecting the optimum trap depth for evaporation. Magnetic traps can also be made very large and deep, and so can capture atoms from the bright optical molasses, the simplest sub-Doppler laser cooling technique. This leads to a very simple route to BEC, yet it can be slow due to low initial densities and only works well for species with magnetically trapped states which are stable against two-body collisions.

Optical traps can work for all species and spin states, however, they don't allow for simple control of the trap depth independent of the trap frequency. As $U_0 \propto P$, the obvious way to force evaporation is to lower the power in the laser beams forming the trap. Unfortunately, if the shape of the beam stays the same, the trap frequency decreases. For a Gaussian beam of waist w_0, the trap frequency decreases as $\omega^2 = 4U_0/(mw_0^2)$. This can lead to low collision rates which halt the progress of evaporative cooling.

The problem can be circumvented by changing the trap shape, either by dynamically changing the waist of a beam [245, 232], or adding a smaller waist beam to an existing trap, a technique known as the "dimple trick" [274, 301]. The smaller waist trap locally increases the density, effectively concentrating the phase-space density in the "dimple" after the atoms have thermalised. Ramping off the larger trap while maintaining thermal equilibrium allows for efficient evaporation. An alternative method is to tilt the trap [138], which can maintain the trap frequency while allowing atoms to leave along one axis.

4.3.3 Inelastic Collisions

A final, but important, consideration is the role of inelastic collisions. Any change in the internal state is undesirable as normally we aim to work with a spin-polarised sample. These collisions can also release a significant amount of energy, causing heating and loss of atoms from the trap. There are many different mechanisms for inelastic loss, and like all scattering properties, the relative strengths of each vary drastically for each atomic species. The ultimate success of any evaporative cooling depends on the ratio of elastic collisions to inelastic collisions, so understanding the latter is crucial.

As discussed earlier in Chapter 1 understanding and preventing inelastic collisions in ultracold molecules is an active area of research [17, 107], and only very recently has the evaporative cooling of molecules become possible [259, 290, 20, 183]. This will be important for the future of ultracold molecule research, but for the present discussion, we will stick to atoms and briefly summarise the most relevant mechanisms in ^{87}Rb and ^{133}Cs mixtures.

First, there are two-body processes, which involve two particles and scale with temperature and density in the same way as elastic collisions. One of these is the scattering of atoms which aren't in the absolute Zeeman ground state into lower states, known as dipolar relaxation [270]. This loss mechanism is particularly strong for the relatively heavy ^{133}Cs where there is a large spin-orbit interaction[6]. Using the lowest energy (not magnetically trappable) Zeeman state is the only way to avoid these losses, and so in practice, ^{133}Cs BEC can only be formed in optical traps.

When using optical traps, it is important to consider internal state-changing processes involving light. Off-resonant single-photon scattering not only heats the atoms via photon recoil but can also change their internal state leading to dipolar relaxation and more heating. The rate of internal state changing scattering[7] goes as $1/\Delta^4$ [115], and so is more of a problem with relatively near-resonant light.

A laser can also excite two elastically colliding atoms into an excited molecular state [205, 146, 201]. These photo-association spectra appear as dense forests of sharp loss features which appear red-detuned from an atomic transition by energy less than the binding energy of the bialkali molecule. These lines are strongest when there is a strong Franck-Condon overlap between the colliding pair state and the excited vibrational state [205], and so in practice, this means that particular care should be taken when choosing the wavelength of near-resonant red-detuned traps, detuned by less than around 100 nm.

When a third atom is involved in a collision, inelastic scattering into molecular states becomes allowed by energy-momentum conservation. These collisions release large

[6] The spin-orbit interaction makes it easier for the ^{133}Cs pairs in s-wave scattering events to couple to rotating molecular states, which contributes to the rich structure of Feshbach resonances in ^{133}Cs [151], but also yields a strong indirect coupling between the two nuclear spins and a very high rate of spin changing collisions [204].

[7] This process is often known in the literature as "spontaneous Raman scattering"

amounts of energy such that usually all 3 atoms are lost from the trap. As the rate of a three-body process scales as n^2, these losses preferentially affect the coldest atoms at the centre of the trap, leading to anti-evaporative heating. Again, this is particularly a problem for ^{133}Cs. On a basic level, this can be understood by noting that a large scattering length greatly enhances the likelihood of three-body recombination. From a qualitative argument considering the chance of three particles meeting with the right energy and momentum, it can be shown [88] that the rate of these inelastic collisions goes as

$$\Gamma_{3b} = L_3 n^2 \propto \hbar a^4 n^2 / m. \tag{4.10}$$

Beyond this simple picture, bound trimer states can introduce resonant features to the three-body loss spectrum. These were first noted by Efimov in the context of nuclear physics [82], and in our case lead to resonances in the 3-body loss spectrum which can be beneficial for evaporative cooling [164, 87]. The most relevant feature in ^{133}Cs is a loss minimum that occurs around $200a_0$, realised at a magnetic field of e.g. 22G where $L_3 \approx 3 \times 10^{-27}\,\mathrm{cm}^6/\mathrm{s}$ [166]. This is still large compared to other species, for example ^{87}Rb where $L_3 \approx 2 \times 10^{-29}\,\mathrm{cm}^6/\mathrm{s}$ [271].

4.3.4 Dual species Evaporation

Following the case of evaporating a single species, it is worth considering the case of trying to evaporate two species in the same experiment, as is required to produce ultracold molecules.

For some mixtures, where there are favourable interspecies interactions with a high ratio of elastic collisions to inelastic collisions, sympathetic cooling provides a very effective route to dual-species degeneracy [210, 126]. Here a large bath of one species, typically ^{87}Rb or ^{23}Na, is selectively evaporated whilst maintaining thermal equilibrium with a small amount of the other species. This is especially straightforward in magnetic traps where the evaporation is controlled by RF radiation and generally leads to very efficient cooling for the minority species, with $\gamma > 10$ routinely reported. Indeed for

some species, e.g. the K isotopes, it is easier to cool them sympathetically than to build a single species experiment.

For some species, sympathetic cooling is hindered by either very small interspecies elastic collisions, or large interspecies inelastic losses. In these mixtures, methods have been developed where the two species are evaporated in separate optical traps and then merged [173, 76, 116].

The older Durham RbCs experiment uses the sympathetic cooling method to produce dual-species degenerate mixtures in a dipole trap loaded from a magnetic trap [197], which realises a simple and effective way to create the high phase-space density mixtures needed for making molecules. However, this method is slow, requiring 40 s of evaporation in the magnetic trap [198] and doesn't integrate well with our requirement for optical transport, nor the DRSC technique which leaves the atoms in a high-field seeking state. Additionally, because of the immiscibility of the two condensates (see Chapter 1), it is preferable to form the two BECs separately so that they can be merged in a controlled manner [239]. Our experiment is therefore designed to use the alternative method of avoiding interspecies collisions by evaporating in separate dipole traps. This chapter focuses on the evaporation of the two species in separate sequences, and our plans for simultaneous evaporation are discussed in Chapter 7.

4.4 Experimental Results

Having summarised the relevant physics, this section reports on the methods used in our lab to achieve BEC of both ^{133}Cs and ^{87}Rb in the science cell.

4.4.1 Overview

After optical transport, we trap around 2×10^6 ^{133}Cs or 1×10^6 ^{87}Rb atoms in a trap which is mode matched to the transport lattice, which we call the science cell reservoir, for more details on this trap see Chapter 3. This wide trap is unsuitable for evaporation towards BEC as it cannot be ramped down while maintaining high trap frequencies. Therefore we use a tighter waist "dimple" trap which we load isothermally from the

reservoir trap.

4.4.2 Trap Design

Efficient evaporation is dependent on careful control of the trap depth and the trap frequency. As discussed earlier in Chapter 2, the potential of a neutral atom trap consists of three terms:

$$U(\mathbf{r}) = -\mu \cdot \mathbf{B}(\mathbf{r}) - \frac{1}{2}\alpha_\lambda I_\lambda(\mathbf{r}) - mg\mathbf{z} \tag{4.11}$$

where μ denotes the magnetic moment of the atom and α_λ the real part of the polarisability at wavelength λ.

Our aim in evaporative cooling is to reduce the trap depth while maintaining a high collision rate, and ensuring that the atomic density never becomes so high that 3-body loss becomes a problem. A strategy widely employed for atoms in the lowest energy Zeeman state is to use a pair of far red-detuned Gaussian laser beams crossing at a point in the horizontal plane to provide the confining part of the potential. The choice of waist size and crossing angle will determine the shape of the trap. This optical trap is combined with a magnetic levitation field, as discussed in Chapter 2.

The dimple trap we use is designed with waist sizes which yield trapping frequencies which balance the need for fast thermalisation of ^{87}Rb whilst preventing large rates of inelastic 3 body loss in ^{133}Cs. Following previous ^{133}Cs experiments [301, 173, 238], we choose to use one beam with waist $w_0 \approx 50\,\mu$m and another with waist $w_0 \approx 100\,\mu$m, crossing at an angle of 70°. This is a configuration which is similar to those reported whilst also being compatible with the optical access around our cell (see Fig 4.2). It should be noted that if the system was optimised for ^{87}Rb alone, narrower waists would be better to increase the elastic collision rate [13].

4.4.3 Optical Methods

The dimple beams both use 1064 nm light from the system detailed in Chapter 3, To achieve the desired trap parameters the beams out of the optical fibres are expanded

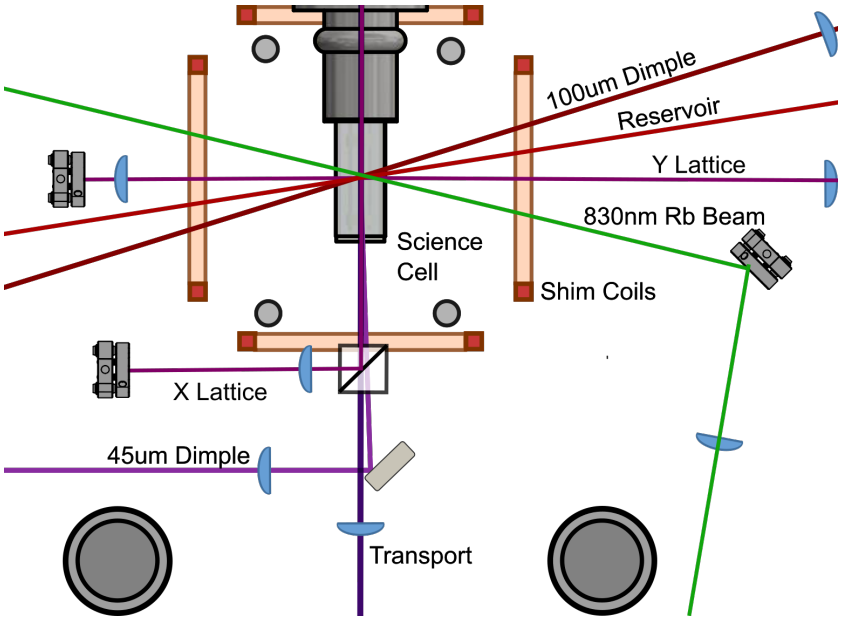

Figure 4.2: Optical layout around the science cell, showing the trapping beams, and relevant obstructions to optical access such as mounting posts (grey circles) and coils (dark orange). Due to the AR coating on the cell, the 1064nm beams must have an angle of incidence of less than 20 degrees.

using telescopes so that focusing lenses placed $1f$ away from the centre of the chamber produce the designed beam waists. The layout of the 1064 nm trapping beams used is illustrated schematically in Fig 4.2.

As is clear in Fig. 4.2, our scheme involves many different 1064 nm trapping beams. It is vital that all of these beams are mutually incoherent to avoid accidentally forming unwanted optical lattices via interference at the crossing point. To ensure mutual incoherence when beams are derived from the same source we chose AOM detunings such that all beams are more than 20 MHz mutually detuned, and any interference effects will be averaged out on the time scale of atomic motion.

Intensity control for both dimple beams is achieved using the standard technique where feedback from a photodiode is fed into a PI controller which actuates the beam power via modulating the amplitude of the RF sent to an AOM. The PI controller is an in-house design, where the sensor signal is low pass filtered to a bandwidth of around

10 kHz to reduce noise. Since fast actuation is not important for these traps we tune the PI controllers conservatively to reduce the servo bump. This is important later in the sequence as the servo bump appears at frequencies that correspond to the trap frequencies formed when loading the BEC into an optical lattice.

To align the dimple trap beams to the reservoir we first got the coarse alignment correct by observing the diffuse reflections of the different beams off the glass cell using an IR camera. To obtain a signal of the atoms interacting with the beam we turn the dimple beam on at maximum power after letting the atoms in the reservoir trap expand along one beam by turning the other beam off, choosing the expansion to be along the beam which is most perpendicular to the new trap. This allows us to coarsely align each beam individually by maximising the atom number captured. Final precise alignment is done by maximising the capture of atoms into the crossed dimple trap at lower powers.

4.4.4 Characterisation of the trap frequency

After aligning the dimple beams to the larger volume reservoir trap, it is important to check that we have crossed the beams such that their foci overlap. This is done by measuring the trap frequency of the harmonic potential, either via parametric heating or in our case by exciting centre-of-mass oscillations of the cloud.

The simplest way to excite oscillations is to drop the thermal atoms trapped in the dimple by turning off the beams and then recapturing them in the beam of interest[8]. Varying the amount of hold time allows observation of the oscillation of the cloud, as seen in Figure 4.3. Effects such as collisions, trap anharmonicity and coupling between the trap axes can change the oscillation amplitude over time, and so a function of the form $y_{\mathrm{COM}} = Ae^{-t/\tau} \sin \omega t + \phi + y_0$ provides a good fit to the data.

To optimise the distance between the final lens of each dimple and the trap centre we maximise this measured frequency.

By measuring the trap frequency at different powers we can extract a value for the beam waist, this is illustrated in Figure 4.3 part (b). For a perfect Gaussian beam of $1/e^2$ radius (waist) w_0, neglecting gravity we expect [115]

[8] Usually, a few ms is sufficient for the atoms to have fallen a small fraction of the beam waist.

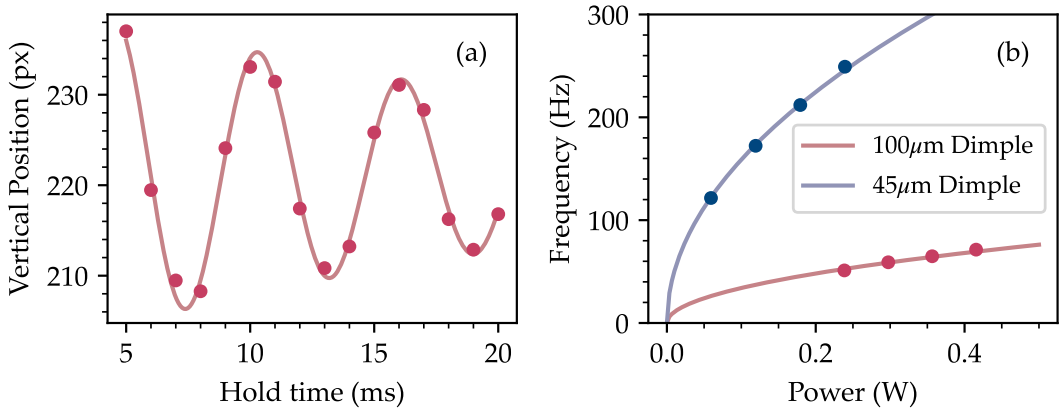

Figure 4.3: Characterising the Dimple trap using ^{133}Cs atoms. (a) shows a representative trap frequency measurement showing the clear centre of mass oscillations. These data were taken in the 45 µm Dimple at 120 mW. A frequency of 172.3(8) Hz was extracted by fitting the data with an exponentially damped sinusoid. (b) shows a summary of data taken at different powers for both beams. The lines show a fit of the form $f^2 = mP$. Error bars based on the statistical uncertainty in the trap frequency fit are too small to be resolved on this plot. From the fits in (b), we extract $1/e^2$ radii of 97.7(6) µm and 45.1(2) µm

$$\omega_r^2 = \frac{4\alpha}{\varepsilon_0 c m w_0^4} P \tag{4.12}$$

where α is the real part of the atomic polarisibility[9] at the trap wavelength. For ^{133}Cs this is 1167 a.u. [253].

After optimisation, via moving the position of the final focusing lens, and measuring the trap frequency we find beam waists from this method of 97.7(6) μm and 45.3(1) μm for our two beams, where the errors are statistical errors from the fits. These values are within a few per cent of values from beam profiling measurements taken using a CCD camera. It is clear that especially for the larger beam there is a small systematic effect from the gravitational force, which we could account for with a more detailed model.

[9]It is useful to note the conversion between atomic and SI units for polarisability: $\alpha/(\text{a.u.}) = 4\pi\varepsilon_0 a_0^3 \alpha$,where a_0 here is the Bohr radius.

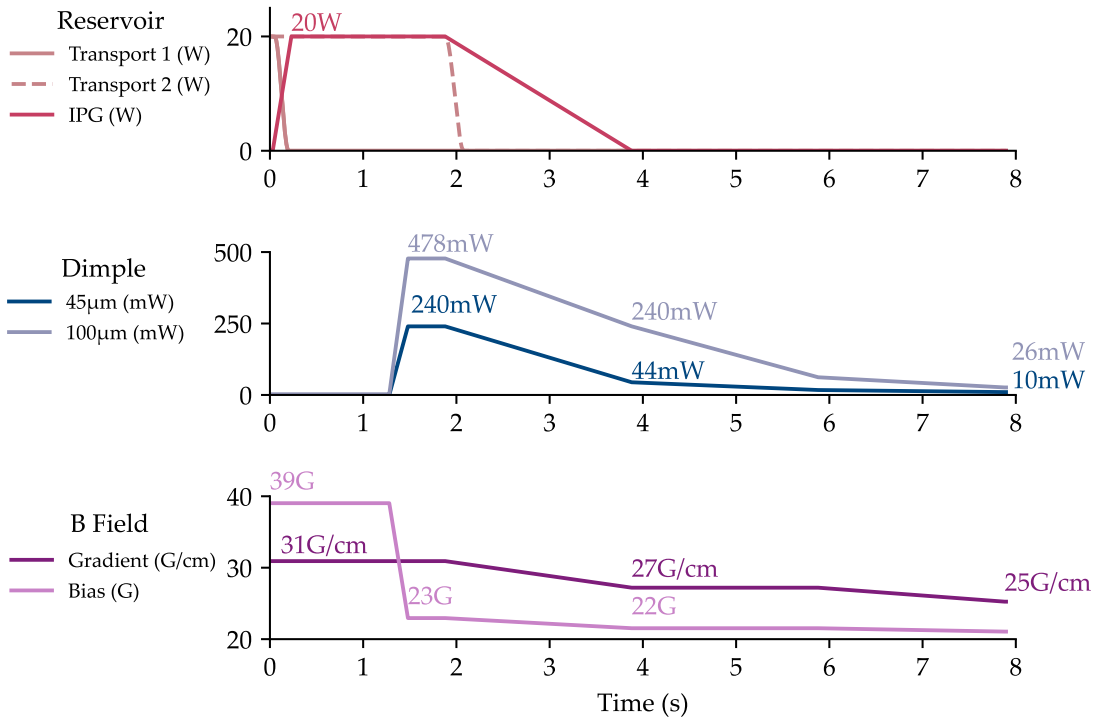

Figure 4.4: Schematic of evaporation trajectory used to reach BEC for ^{133}Cs. Details of each step are given in the text.

4.4.5 Evaporation

To perform evaporation to reach BEC we use sequences as shown in Figure 4.4. Both the ^{87}Rb and ^{133}Cs sequences have the same basic structure: atoms are transferred from the transport lattice to the SC reservoir, as discussed in Chapter 3. After a short hold to allow thermalisation, the tighter waist dimple trap is ramped on in around 100 ms. Forced evaporation then proceeds by ramping down the powers in the beams, first ramping off the reservoir beams, and then ramping down the dimple beams. In the final stages of evaporation, we benefit from the tilting of the trap due to gravitational acceleration [138]. This is illustrated in Fig 4.5, which shows the simulated trap frequency - trap depth relationship for the dimple trap. At depths below $U_0/k_B \approx 1\,\mu$K trap frequency is significantly larger than that expected from $\omega \propto U_0^{0.5}$ scaling without any tilt.

There are a couple of species-specific aspects to the sequences. For ^{133}Cs the mag-

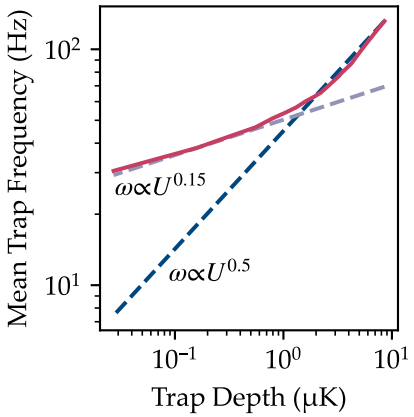

Figure 4.5: Geometric mean trap frequency $\bar{\omega} = (\omega_x \omega_y \omega_z)^{1/3}$ vs trap depth U calculated for the dimple trap during the last two evaporation ramps (dark red solid). Without tilting the trap, we would expect $\bar{\omega} \propto U^{0.5}$ (dark blue dashed). Gravity reduces the trap depth, allowing forced evaporation to continue at moderate trap frequencies, with $\bar{\omega} \propto U^{0.15}$ (light blue dashed).

netic field strongly influences the scattering rate and must be tuned appropriately. After loading the dimple at a field of around 40 G, where the scattering length is large, we then ramp the field to an empirically optimised value close to the Efimov minimum at 22 G to reduce 3-body loss. For Rb the magnetic bias field only influences the magnetic potential used to levitate, but as discussed in Chapter 2 using a large bias field during the reservoir stage is important to counteract the anti-confining effect of the quadrupole field and maintain a high ratio $\eta = U/kT$.

For ^{87}Rb, the lower collision rate and lower polarizabilities need to be accounted for. To counteract these we used an additional trapping beam at 830 nm and 50 μm waist, which is used to increase the trap depth and peak density during the loading of the dimple trap (see Figure 4.2). As this is a near resonant beam it is ramped off with the reservoir beam to avoid spontaneous scattering. Longer collision timescales necessitate longer evaporation ramps, and we used larger dimple powers to counteract the lower atomic polarizability at 1064 nm compared to ^{133}Cs.

The sequences for both species were optimised by maximising the phase-space den-

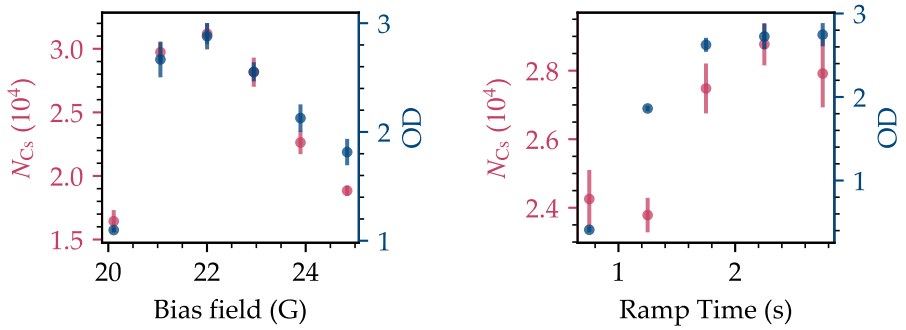

Figure 4.6: Example optimisation plots for evaporation. In both plots, the atom number and peak optical depth are measured at the end of evaporation.

sity (PSD) at successive points in the sequence. PSD was measured by using TOF imaging to extract the temperature of the atoms and simulation of the trapping potential to estimate trap frequencies, but can also be estimated for the purposes of optimisation by observing the peak optical depth (OD) of the cloud after a fixed TOF. In Figure 4.6 example optimisation plots are shown, where the final BEC atom number and OD after a 50 ms TOF are plotted for different experimental parameters. (a) shows the bias field while ^{133}Cs is evaporated in the dimple. The bias field controls the scattering length and 3-body loss rate and as expected we find optimal performance around the Efimov minimum [164]. (b) shows the length of the three ramp steps, which controls the rate of forced evaporation. We find that the cloud evaporates efficiently if the ramp time is longer than 1.5 s. For ^{87}Rb this time scale is closer to 3s.

After optimisation, we can analyse the evaporation trajectory by measuring the thermodynamic properties at various points in the evaporation sequence. Fig. 4.7 (a) shows the PSD-number relation for our optimised sequences, along with the number density and calculated elastic collision rate. Using the definition of evaporation efficiency from Eqn. 4.8, we find $\gamma = 2.4(1)$ and 2.42(5) for Cs and Rb respectively, comparable to other experiments using the dimple method. [173, 301].

By looking at Figure 4.7 (b) and (c), we see two effects of the decrease in trapping frequency during optical evaporation. We see the peak number density, $n_0 = N\omega^3 \left(\frac{m}{2\pi k_B T}\right)^{3/2}$ doesn't significantly increase during evaporation which helps prevent

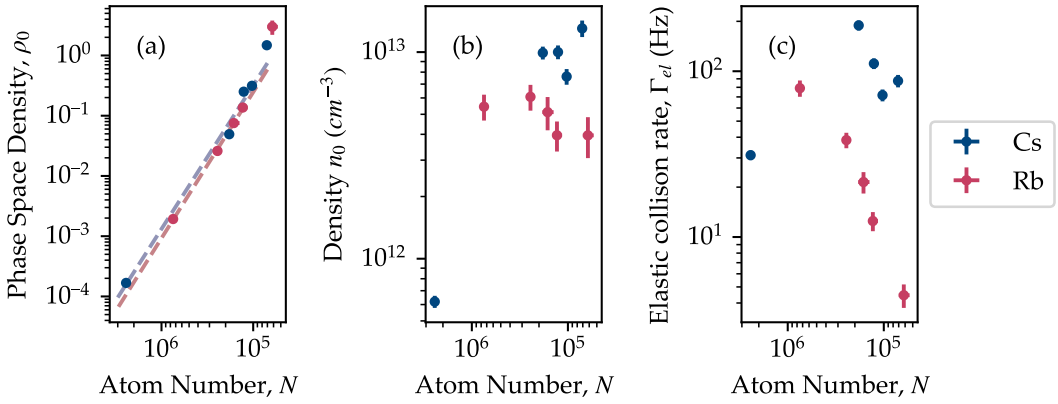

Figure 4.7: Key thermodynamic properties during evaporation, plotted as a function of decreasing atom number. (a) Peak phase-space density $\rho_0 = N(\hbar\bar{\omega}/k_B T)^3$, which measures the overall success of the cooling. (b) Peak number density, which gives an idea of the importance of 3-body loss and (c) Calculated peak elastic collision rate, which sets the time scale for thermalisation. The dashed lines in (a) are linear fits to the trajectory in log(PSD) vs log(N) space and yield evaporation efficiencies of 2.4(1) and 2.42(5) for Cs and Rb respectively.

large 3-body loss. However, the peak elastic collision rate, $\Gamma_{\rm el} = N\omega^3 \frac{m}{2\pi^2 k_{\rm B} T}\sigma$, plotted in (c) does significantly decrease for ^{87}Rb. This low collision rate is the reason longer evaporation times are needed for ^{87}Rb in our experiment compared to other methods.

We can estimate the importance of 3-body loss by considering the peak density plotted in (b), and using L_3 values reported in literature [164, 271]. We expect a minimum 3-body loss lifetime of $(L_3\langle n^2\rangle)^{-1} \approx 4000\,$s for ^{87}Rb and 2 s for ^{133}Cs. Obviously ^{87}Rb would benefit from evaporation in a tighter waist trap, where we could trade off the unnecessarily long 3-body loss lifetime for an increased thermalisation rate.

4.4.6 Crossing the Phase Transition

The emergence of the BEC is most clearly seen in the momentum distribution imaged in TOF, as shown in Figure 4.8. The condensate appears as a sharp peak with a characteristic parabolic momentum distribution, known as the Thomas-Fermi distribution [153]. The disappearance of the thermal Gaussian distributed fraction indicates the production

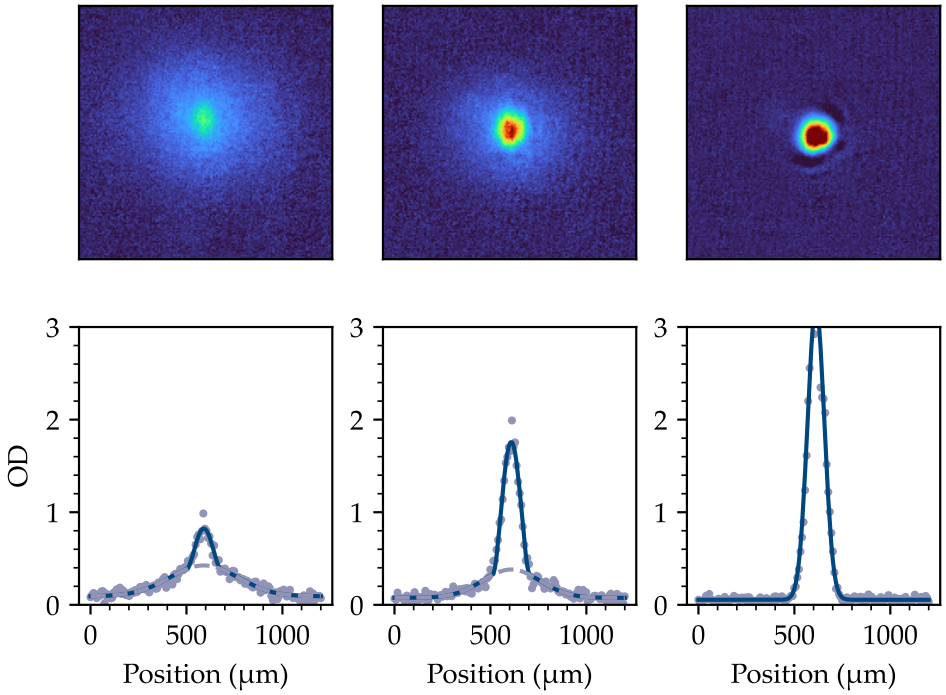

Figure 4.8: Cs crossing the BEC transition. Absorption images taken after 45ms TOF and bimodal fits to central horizontal cuts are shown for clouds produced at successive stages of the final evaporation ramp.

of a cloud with a high condensate fraction, a so-called pure BEC. We are able to produce pure BECs with around 3×10^4 ^{133}Cs atoms or 5×10^4 ^{87}Rb atoms.

4.5 Conclusion and Outlook

Achieving BEC for both species separately was an important milestone for the experiment. In the short-term perspective, BECs are of great practical use in setting up optical lattices[10], and the ability to produce quantum degenerate gases in the science cell demonstrates that our optical transport scheme was sufficient to meet the near-term needs of the experiment. Looking towards the long-term goals, degenerate gases are cru-

[10]BECs enable much easier atom-diffraction calibration of optical lattice depth

cial to preparing low entropy systems for optical lattice experiments needed for quantum simulation. ^{133}Cs is especially interesting due to its tunable interactions and large fine structure splitting which helps realise spin-dependent lattices [142] for quantum simulation of models with effective magnetic fields. These applications are being pursued by a new microscope at LMU [140, 159, 298].

However, it should be noted that our current apparatus is not able to produce dual species condensates, which would be the ideal starting point for our planned experiments with ultracold molecules. Currently, we suffer from two unfortunate properties of the ^{87}Rb ^{133}Cs mixture: unwanted sympathetic cooling, and interspecies 3-body loss. These are both well-known problems when working with this mixture in optical traps, and as mentioned earlier, we plan to tackle them using a variation on the method established in Innsbruck [173], which is discussed in more detail in Chapter 7.

Chapter 5

Optical Lattices

5.1 Introduction

Optical lattices are periodic potentials for ultracold gases formed by interfering lasers. By using interference in a controlled way it is possible to create large arrays of sub-wavelength scale traps with very high uniformity and in almost arbitrary geometries. As well as being useful for cooling and trapping atoms, these periodic structures inspire a direct analogy with lattices encountered in condensed matter physics. This idea of simulating condensed matter systems using ultracold atoms has blossomed into a highly fruitful area of research [119]. Ultracold experiments allow for precise control and tunability of lattice systems and give a complementary set of measurement and preparation techniques compared to traditional solid-state experiments. These have enabled the study of phenomena which are difficult to realise in electronic settings. For example, optical lattices were used in the first direct observation of Bloch oscillations [63], a textbook example of counterintuitive lattice physics.

In early optical lattice experiments, only the bulk properties and momentum space correlations were observable [112, 94], but the development of single-site resolved imaging techniques has allowed for full microscopic investigation of these systems [10]. These "quantum gas microscope" experiments are discussed in more detail in Chapter 7, and a review can be found in [118].

Species	$E_{\mathrm{rec,1064nm}}$/h (kHz)	$E_{\mathrm{rec,1064nm}}/k_B$ (nK)
^{87}Rb	2.0	97
^{133}Cs	1.3	64
^{87}Rb^{133}Cs	0.8	38

Table 5.1: Recoil energy unit conversions, calculated for a $\lambda = 1064$ nm retro reflected lattice.

This chapter details the development of our optical lattice system, designed ultimately for single-site resolved imaging of molecules. After an introduction to the physics of lattices, the design and characterisation of our 3D optical lattice is presented. Finally, we use this optical lattice to observe the quantum phase transition between the superfluid and Mott insulator states in a system with tunable interactions.

5.2 Lattice Physics

First, it is helpful to review the physical description of particles in periodic potentials so that we have a language with which to interpret the results of our lattice experiments. All of this material is covered in more detail in other theses and books [8, 112, 261, 293, 175, 54].

5.2.1 Bloch Waves and Wannier States

To start with the simplest possible case, let us first consider a single quantum particle moving in the potential of a 1D-lattice potential

$$V(x) = V_0 \cos^2(k_{\mathrm{lat}} x). \tag{5.1}$$

This potential can be realised by the standing wave formed by a retro-reflected laser, in which case $k_{\mathrm{lat}} = 2\pi/\lambda$ where λ is the laser wavelength. This corresponds to a spacing between lattice sites of $a_{\mathrm{lat}} = \lambda/2$. A natural unit for the lattice depth, V_0, is the recoil energy, $E_{\mathrm{rec}} = \hbar^2 k_{\mathrm{lat}}^2/2m$. Relevant recoil energies for our work are tabulated in Table 5.1.

An ideal lattice Hamiltonian has a discrete translational symmetry, which must be obeyed by any eigenfunction of the potential. We can express this formally by saying the Hamiltonian commutes with a translation operator $\hat{T} = e^{-i\hat{p}a_{\text{lat}}/\hbar}$, $\hat{T}\psi(x) = \psi(x + a_{\text{lat}})$. Since it is a unitary operator the eigenfunctions of $\hat{T}$ are of the form

$$\hat{T}\phi_\alpha(x) = e^{i\alpha}\phi_\alpha(x) \tag{5.2}$$

In other words, the wavefunction simply "picks up" a phase α when it is translated by a lattice vector a. This allows us to write the eigenstates as

$$\underbrace{\psi_q^n(x)}_{\text{Bloch wave}} = \underbrace{u_q^n(x)}_{\text{Bloch function}} \times \underbrace{e^{iqx}}_{\text{plane wave}}, \tag{5.3}$$

where q is the quasimomentum. Mathematically, q is the rate of phase increase per unit length of translation, which naturally translates to momentum in the free particle case. Unlike momentum, q is only defined over the region $[-k_{\text{lat}}, k_{\text{lat}}]$ which is known as the first Brillouin zone. This result is known as Bloch's theorem.

Using Equation 5.3 as an ansatz, we can solve the Schrödinger equation to find the energy eigenstates. It is convenient here to note that since $u_q^n(x)$ and $V(x)$ are periodic, they have a simple representation as discrete Fourier transforms:

$$\begin{aligned} u_q^n(x) &= \frac{1}{\sqrt{2\pi}} \sum_{j=-\infty}^{\infty} c_j^{(n,q)} \mathrm{e}^{\mathrm{i}2k_{\text{lat}}xj}, \\ V(x) &= \frac{V_0}{2}\left(1 + \frac{e^{i2k_l x} + e^{-i2k_l x}}{2}\right). \end{aligned} \tag{5.4}$$

Using these we can transform the Schrödinger equation into a matrix diagonalisation problem:

$$\begin{aligned} \hat{H}\psi_q^n(x) &= E_q^n \psi_q^n(x), \\ \sum_{l=-\infty}^{l=+\infty} H_{l,l'} c_l^n(q) &= E^n(q) c_{l'}^n(q) \end{aligned} \tag{5.5}$$

where

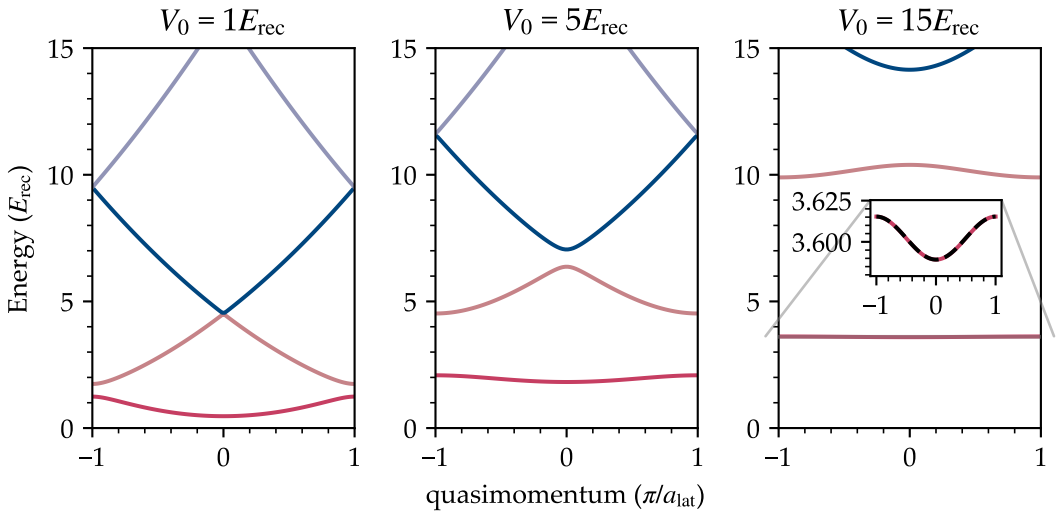

Figure 5.1: Band structure for a single particle in a 1D optical lattice $V(x) = V_0 \cos^2(x)$. As the lattice becomes deeper the gap between the first band and the second excited band widens, eventually, this gap is approximately the harmonic oscillator spacing in the lattice. For lattices deeper than $\approx 5E_{\mathrm{rec}}$, the ground band dispersion relation is well approximated by the tight-binding model $E(k) = -2J\cos^2(ka)$, shown in the inset as a black dashed line.

$$H_{l,l'} = \frac{\hbar^2}{2m}(2lk_{\mathrm{lat}} + q)^2\delta_{l,l'} + \frac{V_0}{4}(\delta_{l,l'+1} + \delta_{l,l'-1}) \tag{5.6}$$

In the systems we study, where only the first few bands are populated, the matrix can be safely truncated at finite l. This allows numerical diagonalisation to find the single particle wavefunctions and energies, as shown in Figure 5.1.

Looking at the energy structure in Figure 5.1 we see that as the lattice depth increases, avoided crossings at $q = 0$, $q = \pi/a_{\mathrm{lat}}$ open up and distinct bands appear. In the deep lattice limit, the lowest band is separated from the other bands by $\Delta E = E^{(1)}_{q=\pi/a} - E^{(0)}_{q=\pi/a} \approx \hbar\omega_T$, where ω_T is the harmonic trap frequency of the lattice sites, which fits with the intuition that at high lattice depth the low energy lattice physics should map onto an ensemble of separated traps.

We also see at lattice depths greater than about 5 E_{rec} that the lowest band dispersion

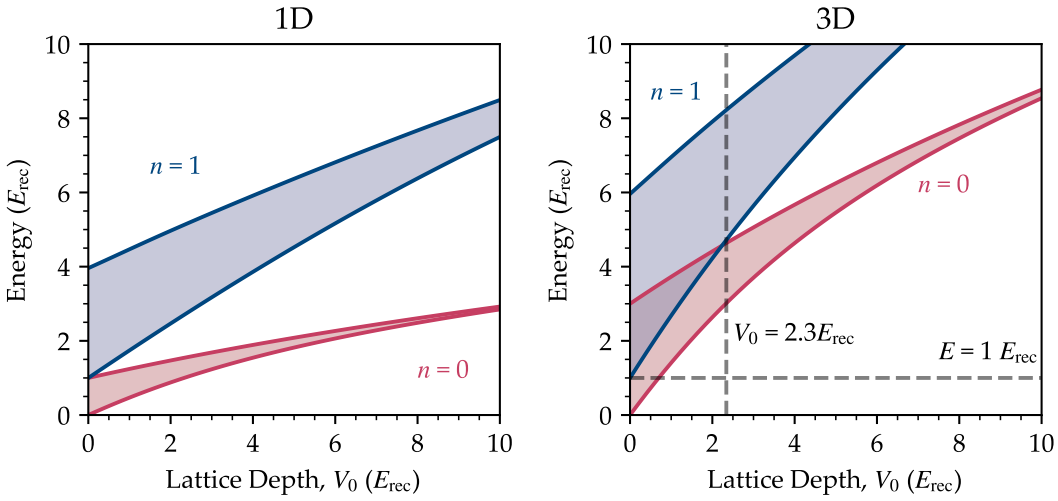

Figure 5.2: Band energies in simple cubic optical lattices, showing the difference between the 1D case and the 3D case. The energy of the highest and lowest states in each band are plotted in dark colours, with lighter shading indicating the width of the band. In 1D there is always an energy gap between the bands for finite V_0, however, in 3D this gap only opens up for all $\mathbf{q} = (q_x, q_y, q_z)$ at $V_0 \approx 2.3E_{\text{rec}}$

relation can be well approximated by the tight-binding model, which uses a linear combination of localised onsite orbitals as basis functions for solving the Hamiltonian and assumes that the only finite matrix elements are between atoms on nearest neighbour sites [8].

This simple model can be extened to a 3D cubic lattice as the potential is separable, $V(x, y, z) = V_0 \sin^2(k_{\text{lat}}x) \sin^2(k_{\text{lat}}y) \sin^2(k_{\text{lat}}z)$. Separability allows us to write the eigenfunctions as products of the 1D Bloch waves, and hence calculate energies as sums over the 1D energies. In 3D the 1st excited band consists of the product of two 1D ground band wave functions and a single excited band wave function, as is shown in Figure 5.2. This means the two bands overlap for lattice depths less than around $V_0 \approx 2.3$, i.e. for certain large $\mathbf{q} = (q_x, q_y, q_z)$ the states with $\mathbf{n} = (n_x, n_y, n_z) = (1, 0, 0)$ character can be lower in energy than those with $n = (0, 0, 0)$ [305]. Similar arguments apply in the 2D case.

How the band gap emerges becomes important when considering how we prepare

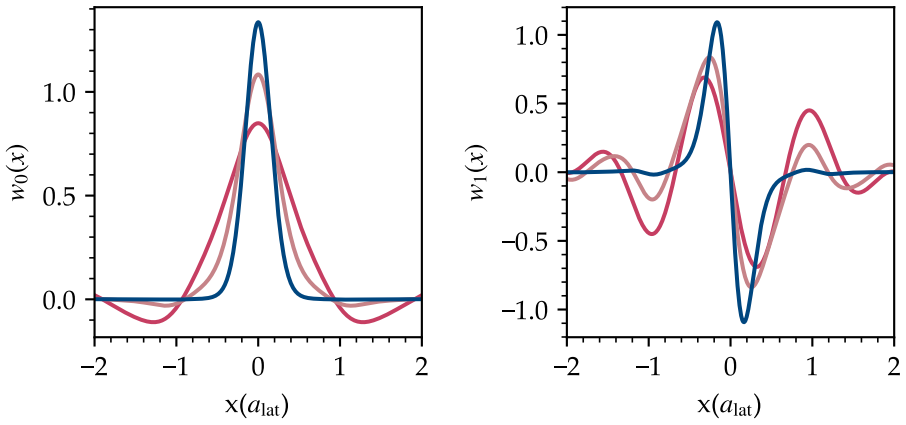

Figure 5.3: Wannier states for the lowest and 1st excited bands for increasing lattice depths $1E_r$ (dark red), $5E_r$ (light red) and $20E_r$ (blue). As the lattice becomes deeper these states become more localised. The plots show the real part of the Wannier state for the lowest band and the imaginary part for the first excited band.

low entropy states by loading lattice from a dipole trap. Fortunately for bosonic samples, if the cloud is condensed, atoms accumulate in $\mathbf{q} = 0$ state, however for fermionic samples or BECs with very strong interactions the filling of high $\mathbf{q}$ states can be significant. This can lead to significant population of the second band even if the lattice is ramped on adiabatically.

The Bloch waves are delocalised over the whole lattice, which makes it difficult to describe local interactions in this basis. A better basis would be a set of localised functions $w_n(x - x_i)$, where x_i is a lattice vector, which are orthonormal [8], i.e.

$$|\langle w_n(x - x_i)|w_m(x - x_j)\rangle|^2 = \delta_{mn}\delta_{ij}. \tag{5.7}$$

We can find a set with these properties from a Fourier sum of the Bloch functions,

$$w_n(x - x_i) = \frac{1}{\sqrt{M}} \sum_q e^{-iqx_i}\psi_q^n(x), \tag{5.8}$$

where M is the number of sites in the lattice. This new set of basis functions, $w_n(x - x_i)$ are known as Wannier functions. Figure 5.3 shows these functions for the lowest two

bands in shallow and deep lattices. We see that for increasing lattice depth the Wannier functions become more and more localised. Finding Wannier functions for the 1D lattice is straightforward, but there is some subtlety in defining these states for lattices with structure within the repeating unit of the lattice, explained in e.g. [22].

At high lattice depths, these functions bear a superficial resemblance to harmonic oscillator wavefunctions, however, they are exponentially localised on the lattice sites as e^{-x}, in contrast to harmonic oscillator wavefunctions which are localised as e^{-x^2}.

5.2.2 Hubbard Model

One of the most celebrated applications of ultracold atoms has been in the study of Hubbard models, as described theoretically in [143]. These are very simple lattice models from condensed matter physics, introduced to understand phenomena which involve strong correlations between electronic quasi-particles in solids. They capture the competition of the delocalising effect of kinetic energy and the localising effect of interactions in a conceptually simple way. In optical lattices, these models can be a very good approximation to experiments, as is shown below in a simple derivation, following lecture notes from Andrew Daley and [305, 112].

On the optical lattice length scale interactions between ultracold (and non-dipolar) particles can be described as contact interactions $V_{\text{int}}(\mathbf{r}) = g\delta(\mathbf{r})$ with strength $g = 4\pi\hbar^2 a_s/m$, and so the microscopic Hamiltonian takes the following relatively simple form

$$\hat{H} = \hat{H}_0 + \hat{H}_{\text{int}} \tag{5.9}$$

$$\hat{H} = \int \mathrm{d}\mathbf{x}\hat{\psi}^\dagger(\mathbf{x})\left(-\frac{\hbar^2}{2m}\nabla^2 + V(\mathbf{x})\right)\hat{\psi}(\mathbf{x}) + \frac{g}{2}\int \mathrm{d}\mathbf{x}\hat{\psi}^\dagger(\mathbf{x})\hat{\psi}^\dagger(\mathbf{x})\hat{\psi}(\mathbf{x})\hat{\psi}(\mathbf{x}), \tag{5.10}$$

where the field operators $\hat{\psi}(\mathbf{x})$ and $\hat{\psi}^\dagger(\mathbf{x})$ represent the annihilation and creation of a particle at position $\mathbf{x}$. Since the interactions are local, it makes sense to expand these in terms of the Wannier basis,

$$\hat{\psi}(\mathbf{x}) = \sum_{i.n} w_n(\mathbf{x} - \mathbf{x}_i)\,\hat{b}_{n,i}. \tag{5.11}$$

At this point, we can make our first simplifying assumption: only the ground band is relevant to the physics, as the band gap is much larger than all other relevant energy scales. This is achieved if $k_B T \ll E_{\text{gap}} \approx \hbar\omega_T$ and if the interaction energies are sufficiently weak[1]. Both of these conditions are straightforward to achieve using ultracold gases, if care is taken to load the lattice adiabatically from a sufficiently low entropy state such as a BEC or a Fermi degenerate gas.

With $\hat{\psi}(\mathbf{x}) = \sum_i w_0(\mathbf{x} - \mathbf{x}_i)\,\hat{b}_{0,i}$ we can expand Eqn. 5.10 into a series of sums over matrix elements of ground band Wannier states with $\hat{H}$:

$$\hat{H} = \underbrace{-\sum_{ij} J_{ij} b_i^\dagger b_j}_{\text{Kinetic Energy}} + \underbrace{\frac{1}{2}\sum_{ijkl} U_{ijkl} b_i^\dagger b_j^\dagger b_k b_l}_{\text{Interactions}} + \underbrace{\sum_i \varepsilon_i b_i^\dagger b_i}_{\text{On-site Energy}}. \tag{5.12}$$

At this point, it is possible to make a second simplifying assumption by identifying the particular values of the matrix elements J_{ij} and U_{ijkl} which dominate over the others. The matrix elements can in general be calculated for any lattice by finding the Wannier functions. However, we can note that since the Bloch functions are eigenfunctions of $\hat{H}_0$ we can simplify J_{ij} [257]:

$$\begin{aligned} J_{ij} &= \int dr w_n^*(r - R_i)\hat{H}_0 w_n(r - R_j) \\ &= \frac{1}{N}\int dr \sum_q \sum_{q'} e^{iqR_i}\psi_{nq}^*(r)\hat{H}_0\psi_{nq'}(r)e^{-iq'R_j} \\ &= \frac{1}{N}\sum_q \sum_{q'} E_{nq'} e^{i\left(qR_i - q'R_j\right)}\delta_{q,q'} \\ &= \frac{1}{N}\sum_q E_{n,q} e^{iq(R_i - R_j)}, \end{aligned} \tag{5.13}$$

[1] $U\langle\hat{n}\rangle/2 \ll \hbar\omega_T$ using terms from later in the derivation

where the representation of the Wannier state in terms of the Bloch states, and the orthonormality of the Wannier states have been used. This works for any lattice where there is only one site per unit cell [200]. The relation in Equation 5.13 allows us to calculate the hopping matrix elements from the Fourier transform of the band dispersion. Equation 5.13 also formalises the intuition that when the dispersion relation of a band is approximately cosine shaped, only nearest-neighbour hopping terms are important. Hence we use the notation $J = J_{i,j}$ for nearest neighbour i, j and assume all other terms are negligible.

The interaction matrix elements, U_{ijkl}, need to be calculated using the Wannier states. It can be shown [112] that in the lowest band the offsite interactions e.g. U_{0101} and tunnelling U_{0001} are both at least two orders of magnitude smaller than the onsite interaction U_{0000} and so is safe to drop the other terms and simply use $U = U_{0000}$.

For lattices with $V_0 \gtrsim 5\, E_{\text{rec}}$ it is, therefore, safe to vastly simplify Equation 5.12 by only keeping nearest neighbour tunnelling and onsite interactions, and we can recover the Hubbard model. Specifically, in the case of a bosonic gas, in the grand canonical ensemble formalism

$$\hat{H} = \underbrace{-J \sum_{\langle ij \rangle} b_i^\dagger b_j}_{\text{N-N hopping}} + \underbrace{\frac{U}{2} \sum_i \hat{n}_i(\hat{n}_i - 1)}_{\text{on-site interactions}} + \underbrace{\sum_i (\varepsilon_i - \mu)\hat{n}_i}_{\text{On-site energy}}, \tag{5.14}$$

where the operators $b_i^\dagger$ etc. obey the bosonic commutator relation $[b_i^\dagger, b_j] = \delta_{i,j}$. μ is the chemical potential which sets the density of particles in the system.

One of the key advantages of ultracold systems is that the parameters of the Hamiltonian can be easily tuned in experiments. In the Bose-Hubbard model case, the tuning can be achieved by varying the lattice depth, V_0 via laser power and the s-wave scattering length, a_s via Feshbach resonances. To determine how V_0 and a_s tune the values of the J and U we can use the single-particle Hamiltonian.

The hopping parameter J can be found directly from the band structure (Equation. 5.13), and if the lattice is deep enough to fulfil the tight-binding approximation then J can be found from the band width: $J = \frac{1}{4}(E(q = k_{\text{lat}}) - E(q = 0))$. An analytic

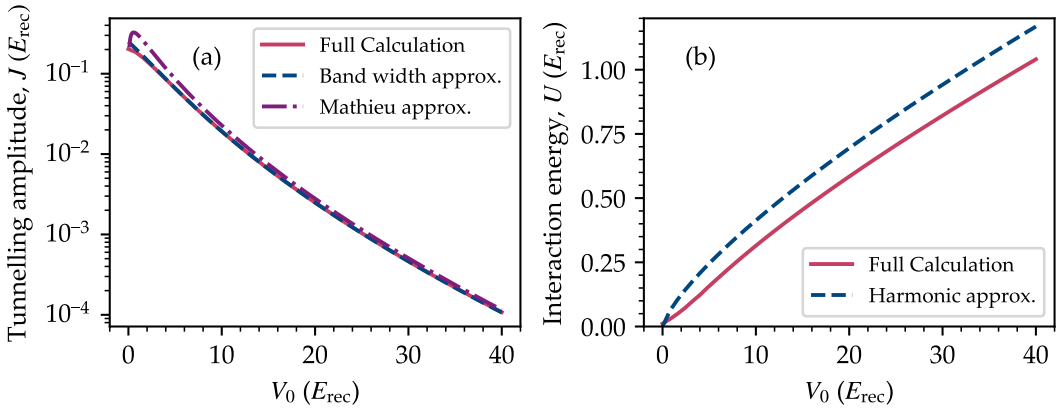

Figure 5.4: Dependence of Hubbard model parameters on lattice depth. (a) The hopping amplitude or tunnel coupling shows exponential dependence on the lattice depth V_0. Red shows the full calculation according to Eqn. 5.13, blue dashed shows J calculated from the width of the lowest band and purple dot-dashed shows the Mathieu approximation given in Eqn. 5.15. (b) The interaction energy U vs V_0, calculated for ^{87}Rb with a_s = 102 a_0. Red shows the full calculation according to Eqn. 5.17 and blue dashed shows the harmonic oscillator approximation, Eqn. 5.18.

approximation can be found by solving the 1D Mathieu equation [321], giving

$$J = \frac{4E_{\text{rec}}}{\sqrt{\pi}} \left(\frac{V_0}{E_{\text{rec}}} \right)^{0.75} e^{-2\sqrt{V_0/E_{\text{rec}}}}. \tag{5.15}$$

Figure 5.4 shows a comparison of the full calculation for J with the bandwidth (tight binding) approximation and the Mathieu approximation (Eqn. 5.15). For lattice depths above $\approx 5\ E_{\text{rec}}$ all three agree well. The scaling of J is generic to any species as it only depends on the ratio of the lattice depth to the recoil energy.

The interaction parameter U is found by integrating the Wannier function. In a 3D separable lattice, we can write $w(\mathbf{r}) = w_x(x)w_y(y)w_z(z)$

$$U = \frac{4\pi\hbar^2 a_s}{m} \int d^3r |w(\mathbf{r})|^4 \tag{5.16}$$

$$U = \frac{4\pi\hbar^2 a_s}{m a_{\text{lat}}^3} \int d^3\xi |w(\xi)|^4, \tag{5.17}$$

where ξ is a dimensionless length such that $r = a_{\text{lat}}\xi$. As the lattice depth increases the confinement of the Wannier function U also increases, as shown in Figure 5.4. As expected, $U \propto a_s$, and so can be controlled independently in systems with accessible Feshbach resonances.

It is tempting to approximate the Wannier states with the corresponding harmonic oscillator ground states to evaluate the dimensionless integral in Eqn. 5.17. This gives

$$U = \sqrt{\frac{8}{\pi}} k_{\text{lat}} a_s \left(\frac{V_0}{E_{\text{rec}}}\right)^{0.75} E_{\text{rec}}. \tag{5.18}$$

Figure 5.4 shows how this compares to the full calculation. For all relevant lattice depths, the harmonic approximation significantly overestimates U but the scaling with V_0 is approximately correct.

In many quantum gas microscopy experiments, the vertical lattice spacing is larger than the horizontal spacing to allow for easier preparation of a 2D gas. As a consequence of Equation 5.17, $U \propto 1/a_z$, and so switching from e.g. a 0.5 μm spacing retro reflected lattice to a 5 μm spacing shallow angle lattice would reduce U by a factor of 10.

5.2.3 Mean field theory of the Bose-Hubbard model

The Bose-Hubbard model has two distinct ground states, dependent on the relative strength of interactions, U, to the kinetic energy term. Below is a very brief summary of the two states, more detail can be found in e.g. [249].

In the case of very weak interactions, we expect the ground state to be the same form as the BEC many-body ground state, except with the single particle state modified by the lattice to be the $\psi^0_{\mathbf{q}=\mathbf{0}}$ Bloch wave,

$$|\Psi_{SF}\rangle = \left(\frac{1}{\sqrt{M}} \sum_{i=1}^{M} \hat{b}_i^\dagger\right)^N |0\rangle, \tag{5.19}$$

where M is the number of lattice sites and N is the number of particles. Since this state retains the off-diagonal long-range order[2] of the BEC, it is known as the superfluid

[2] See [311] or [249] for a definition of this concept

state. We see that locally the atom number can vary freely and the distribution is given by Poissonian statistics. In this state, the atoms are fully delocalised over the lattice.

In the opposite limit of very strong interactions, the ground state minimises the fluctuations of atom number on each site, at the expense of occupying higher **q** Bloch states within the lowest band. Mathematically this can be expressed as a product of local Fock states $|n\rangle$, where for integer $\bar{n} = N/M$

$$|\Psi_{MI}\rangle = \prod_i |\bar{n}\rangle_i. \tag{5.20}$$

It is relatively straightforward to calculate the zero-temperature phase diagram of this model in a mean-field approximation [91, 250, 283]. In summary, the analysis consists of constructing a mean-field version of the model with a term $\psi_{mf} = \langle b_i \rangle$, which allows the off-diagonal long-range order found in the superfluid state. A Landau free energy expansion in terms of ψ_{mf} is used to determine the critical J/U ratio for the second-order phase transition. The resulting phase boundary is shown in Figure 5.5, as a function both of J/U and the chemical potential μ which is used to express the density of particles in the model.

In real optical lattice experiments, there is an underlying long-range potential, $V(r)$ which leads to spatially varying onsite energies ϵ_i. Since the Bose-Hubbard model is local in character we can still use it if the variations in the parameters are on a length scale longer than the longest inter-particle correlations. In the BEC limit, this length scale corresponds to the healing length $\xi = (8\pi n a_s)^{-1/2}$ [95], which is typically on the order of 1 μm. Thus in most cases, it is reasonable to assume that the uniform model results can be applied and we can treat the long-range potential as a spatially varying density $U\bar{n}(r) = \mu_0 - V(r) = \mu_{\mathrm{LDA}}(r)$. This is known as the local density approximation.

Following Jaksch [143] we can get some insight into the Hubbard model ground state with a trapping potential by using the Gutzwiller variational method. In the Gutzwiller method, the variational ansatz is the form of a superposition of local Fock states: $|\phi_i\rangle = \sum_n f_n^{(i)} |n\rangle_i$ where i denotes the site in the lattice. The Mott insulator phase appears as areas with integer number density, i.e. only one component in the superposition. The superfluid phase appears as areas with finite "superfluid density" $\langle b_i \rangle \neq 0$.

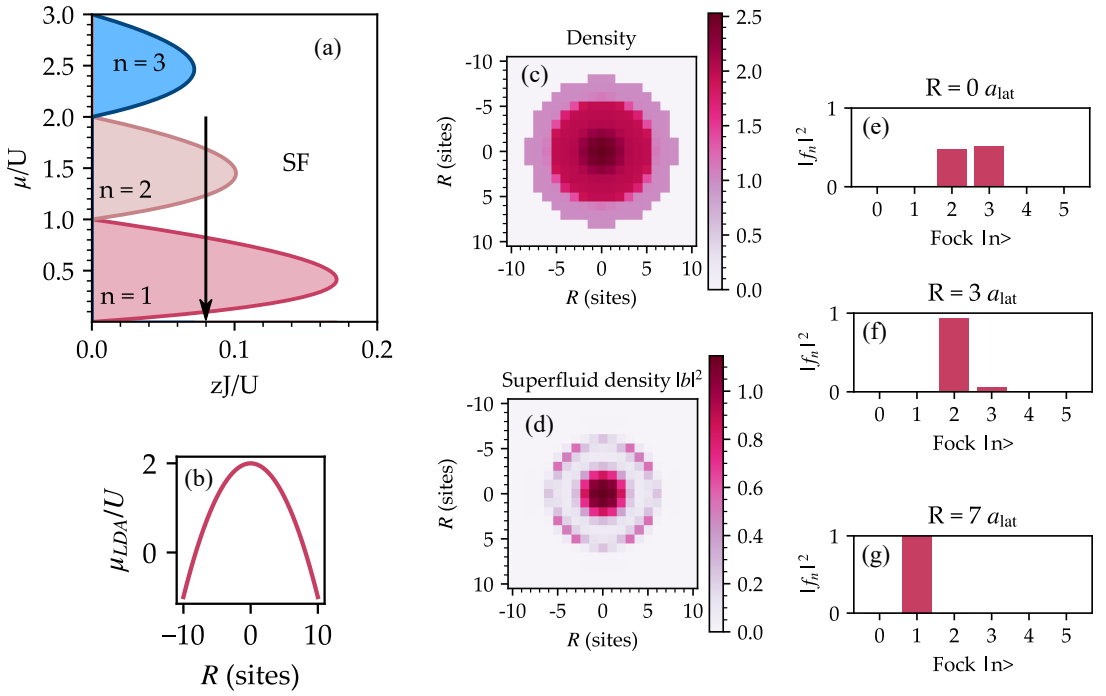

Figure 5.5: Bose-Hubbard model mean field theory for a system with an additional harmonic potential centred at the origin. (a) The calculated phase boundary. The coordination number z counts the number of neighbours each site has. The arrow on the plot indicates the progressively decreasing local μ as a function of distance from the trap. (b) The spatial variation of the local chemical potential. (c) The calculated density profile for the model (parameters in the main text), which shows rings of n=2 and n = 1 Mott insulators, with superfluid areas between them. (d) The calculated superfluid density $\langle b \rangle^2$. (e) Exemplary local Gutzwiller parameters, which can be interpreted as the statistical distribution of particles on a given lattice site, which show the number-squeezing in the Mott insulating shells compared to the superfluid core.

Figure 5.5 shows simulations [56] for a gas with $\mu_0 = 2U, J = 0.02U$ in a confining potential of the form $V(r)/U = 0.03(r/a_{\text{lat}})^2$. In subfigure (c) we see that density decreases away from the centre of the trap, and that for certain r where the local ground state is Mott insulating the density tends to an integer value. The emergence of alternating SF/MI shells is very clear in (d) which shows the relative concentration of superfluid order. (e) shows the Gutzwiller coefficients at various radii, which can be interpreted as the statistical distribution of particles on a site. For $R = 0$ we see a distribution of possible n, in the limit $U \to 0$ this tends to the Poisson distribution. In the Mott insulating shells at $R = 3, 7$, we see that integer occupation of the site becomes very likely.

One of the first applications of single-site resolved imaging was the observation of this microscopic shell structure [265, 10]. These experiments observed that at finite temperatures almost all the positional entropy is located in the super-fluid regions, leaving a low entropy Mott insulator which is the ideal starting point for many other experiments. The control offered by projected potentials allows full utilisation of this effect [48, 140], allowing local reduction of the entropy of the Mott insulator. Similar physics is hoped to be useful in the preparation of low-entropy samples of molecules.

5.3 Design

The optical lattice system in our experiment is designed for quantum gas microscopy, which requires very high lattice depths on the order of 3000 E_{rec} to keep the atoms pinned to sites during imaging. This requirement for high intensities must be balanced with that of providing a uniform lattice at the centre of the trap.

A practical way to quantify the uniformity of the lattice is to consider the largest $\bar{n} = 1$ Mott insulator that can be formed. The Gaussian beam profile of a red-detuned lattice formed by beams of waist w_0 produces a confinement potential of the form

$$V(r) = V_0 e^{-2r^2/w_0^2}, \tag{5.21}$$

where V_0 is the peak lattice depth. Therefore in the local density approximation we have

$$\mu_{\mathrm{LDA}}(r) = \mu_0 - V_0 e^{-2r^2/w_0^2}. \tag{5.22}$$

We can now determine the maximum radius of a $\bar{n} = 1$ Mott insulator by setting $\mu_0 = U$. Inverting Equation 5.22 we find

$$R_{\mathrm{MI}} = \frac{w_0}{\sqrt{2}} \sqrt{\ln \frac{1}{1 - \frac{U}{V_0}}} \tag{5.23}$$

$$R_{\mathrm{MI}} \approx \frac{w_0}{\sqrt{2}} \left(\frac{U}{V_0}\right)^{0.5}, \tag{5.24}$$

where the approximation holds for small U/V_0. We see that the largest possible Mott insulator size is strongly dependent on the beam waist and to a lesser extent the interaction energy.

We can calculate the maximum lattice depth we can achieve for a retro-reflected Gaussian beam of waist w_0 and power P simply as 4 times the depth of a single beam trap [305, 115]

$$V_{0,\mathrm{max}} = \frac{2}{\epsilon_0 c} \mathrm{Re}(\alpha_\lambda) \frac{2P}{\pi w_0^2}. \tag{5.25}$$

We chose to balance these two requirements by choosing beams of around 90 µm waist, which allows us to reach Mott insulator sizes of around 30 sites radius and lattice depths of around 4000 E_{rec} for ^{87}Rb with 10 W of laser power in each beam. For ^{133}Cs these figures of merit are better thanks to larger available scattering lengths and higher polarisibility at 1064 nm.

5.4 Setup

The setup for the 3D square lattice is similar to that of the dipole traps presented in Chapter 4, however, there are a few complications from needing to control the beams at high and low optical powers during the experimental sequence.

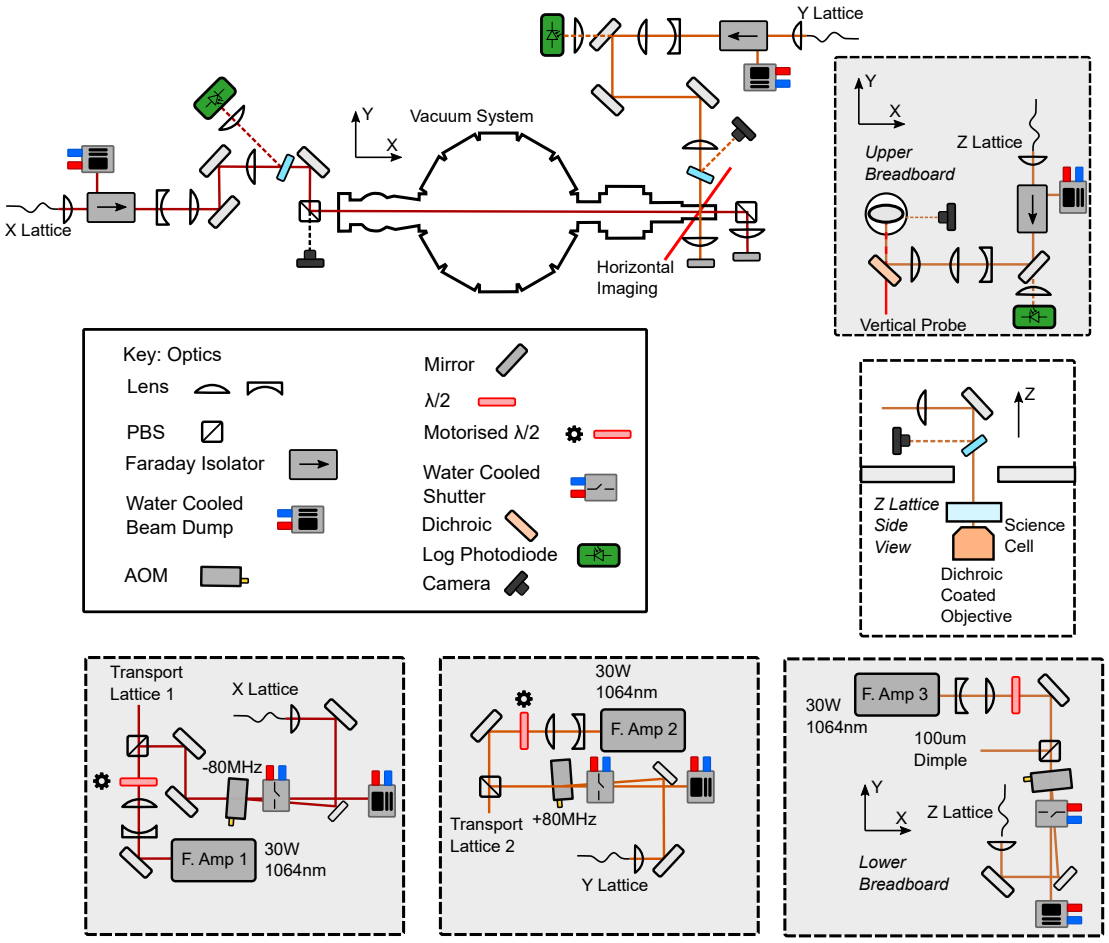

Figure 5.6: Optical layout for the 3D optical lattice, shown schematically. Each lattice beam has an AOM for intensity control and PCF fibre is used to ensure pointing stability. Logarithmic photodiodes placed after the fibres provide feedback on the intensity and Raspberry Pi cameras are used to monitor the positions of the beams.

5.4.1 Optics

Figure 5.6 shows the optical layout of the lasers used for our 3D lattice. For each axis, we use a 30 W fibre amplifier[3] to provide high-power single-frequency light at 1064 nm. Because of the way optical transport is implemented, two of these amplifiers must be phase-coherent. Therefore we carefully choose AOM diffraction orders to ensure sufficient detuning between the lattice beams so that interference is washed out on the timescale of atomic motion. The third fibre amplifier is seeded by an independent laser[4] so that it cannot interfere with the other two microscope lattice beams or the transport lattice beams. Our vertical lattice is retro-reflected off the flat HR-coated surface of the microscope objective.

We use a naming convention for the three lattice axes where X is the transport direction, Y is the perpendicular horizontal direction and Z is the vertical direction.

The stability of the lattice beam focal positions is crucial and so optical fibres are used to ensure that the beam outputs are stable. Due to the high powers needed for the pinning part of the experiment we use photonic crystal fibre (PCF). When using high powers in optical fibre it is important to avoid Stimulated Brillouin Scattering (SBS) within the fibre [269, 68, 83]. To prevent this we use custom short fibres[5] with 1.5 m length. Using focus adjustable couplers we achieve >70% coupling efficiency, which given the manufacturer's specified maximum insertion loss of 6 W allows us to couple in up to 20 W into the fibre, and put up to 13W of light on the atoms. As in the transport lattice, we use high-power compatible Faraday isolators[6] to dump the retro-reflected beam safely.

To achieve the target beam waists we use expanding telescopes combined with a final focusing lens, characterised using a beam profiling camera[7]. When focusing the light after the PCF, we saw that the measured divergence was larger than expected from the beam waist measured on the camera. This caused some difficulties, particularly

[3] ALS-IR-1064-30-A-SF, Azurlight Systems
[4] RIO Orion 1064 nm
[5] Alphanov
[6] EOT Pavos
[7] Thorlabs Zelux

with the X-direction lattice where the optical access was from the far end of the chamber. Again, as in Chapter 4 we characterised the beam waists on the atoms using trap frequency measurements and found measured waists of 87.6(3) μm for the X beam and 80.6(4) μm for the Y beam, slightly smaller than that measured using the beam profiling camera. The vertical lattice is more difficult to characterise this way as the retro reflection cannot be blocked. Therefore we simply use the lattice depth measured by Kaptiza-Dirac diffraction (see section 5.4.3) to optimise the focus position.

5.4.2 Electronics

One key difference between the dipole traps and the lattices is the dynamic range over which we need to control the beams. To perform experiments at under 5 E_{rec} we require powers on the order of 1 mW, however, pinning requires powers on the order of 10 W. If a single linear photodiode is used, where the maximum signal voltage is around 10 V, this means the low optical power signal is washed out in 10 mV scale sensor noise. This is a well-known problem for quantum gas microscope experiments. Some groups rail the power in the beams during pinning, based on the assumption that during imaging the power in the lattices is unimportant. In [25] a dual control scheme is implemented. Other groups use logarithmic photodiode amplifiers or two photodiodes with different gains. We developed a simplified version of the Texas Instruments LOG114 evaluation board to act as a logarithmic photodiode, which we found worked well over seven orders of magnitude in optical power.

In future work, to further improve the low-power servo performance we could use the motorised waveplates to ensure that we operate in the linear response region of the AOM. This would implement a crude form of gain scheduling [18]. However, this would require careful timing of the sequence to allow for the changing waveplates so we have not yet investigated this.

5.4.3 Alignment

The precise alignment of the incoming lattice beams to the existing dipole trap is key for ensuring the atoms are loaded into the lattice with minimal heating. To achieve high ac-

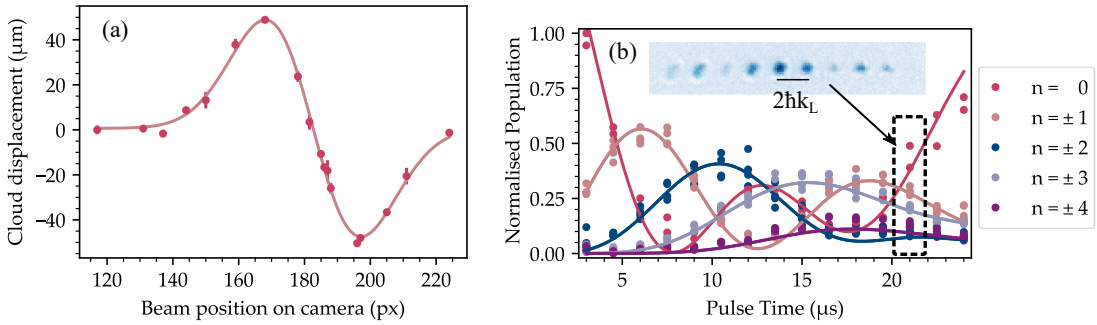

Figure 5.7: Exemplary characterisation measurements. (a) A measurement used to align the X lattice beam to the atoms. As described in the text, if the beam is off-centre from the atomic cloud it imparts a force which we can measure as a displacement in time of flight. (b) Kaptiza Dirac diffraction data used to characterise the Y lattice retro reflection alignment. Short pulses of the lattice on a BEC populate $|2nk_{\mathrm{lat}}\rangle$ momentum states where n is an integer. By fitting to a single particle simulation we can extract the lattice depth.

curacy alignment we used a technique suggested in [303] where the new ingoing lattice beam is applied to the cloud for a short time $t \approx 1/(4f_{\mathrm{trap}})$ before TOF. The momentum applied to the atoms by the lattice beam causes a displacement of the cloud centre after TOF, which gives a derivative-of-a-Gaussian error function for the alignment of the beam, as shown in Figure 5.7. From the fit, we can determine the optimal beam position, in practice the precision of the kinematic mirror mount used limits us to about 5 μm.

5.4.4 Kaptiza Dirac Scattering

To align the lattice retro-reflection precisely, and calibrate the lattice depth we use Kaptiza-Dirac scattering [147, 106]. In this technique, the lattice is switched on to a set power in less than 1 μs, held for a short variable time and then switched off again. The experiment realises a matter-wave analogue of the grating diffraction of light, such as that which occurs in an AOM. Since the diffraction dynamics are strongly dependent on the lattice depth it makes for an ideal calibration measurement.

This system of a BEC being "kicked" by short intense pulses of optical lattices is well studied in its own right, as it makes for a highly tunable test bed for quan-

tum dynamics. Notable experiments include the observation of dynamical localisation [215], topological Anderson insulators [199] and quasi-periodic order in an optical lattice [294]. The basis of momentum states populated by Kaptiza-Dirac type experiments can also be viewed as a synthetic dimension to realise lattice models [98].

To calibrate the lattice depth using the Kaptiza-Dirac effect we use the numerical solutions to the lattice Hamiltonian discussed earlier. The lattice Hamiltonian in the basis of momentum states $|2jk_{\mathrm{lat}} + q\rangle$ can be written as

$$H_{i,j} = \frac{\hbar^2}{2m}(2jk_{\mathrm{lat}} + q)^2\delta_{i,j} + \frac{V_0}{4}(\delta_{i,j+1} + \delta_{i,j-1}). \tag{5.26}$$

Note this Hamiltonian only couples momentum states that differ from q by integer numbers of $2k_{\mathrm{lat}}$, and so if the system is prepared in a BEC with $q = 0$ then the quench to this single particle Hamiltonian can only populate momentum states $2k_{\mathrm{lat}}j$. Experimentally, the technique is facilitated by the narrow momentum width of the BEC, but can also be observed with thermal atoms [106].

The dynamics can be calculated by integrating the Schrodinger equation. Crucially the time scale of the dynamics and the relative population of different states are strongly dependent on the lattice depth, so we can fit the data to simulations with variable V_0 to calibrate the lattice depth, as shown in Figure 5.7.

Realising the short pulses needed for these experiments requires that the AOMs are switched on as quickly as possible. To achieve $<1\,\mu$s rise times we control the AOM driver modulation voltage directly using an RF switch, bypassing the servo. Another complication is that as the high k diffraction orders expand along the optical axis of the absorption imaging system they are affected by defocus aberration, which can be seen in Figure 5.7. Since we integrate the optical depth to determine the population in each peak this is not a serious problem.

From Kapitza-Dirac measurements we extract lattice calibrations shown in Table 5.2. From the perspective of quantum gas microscopy, these are promising results, as we can quite easily achieve the large lattice depths required for fluorescence imaging [265], even with the less polarizable ^{87}Rb.

Lattice Direction	Observed ^{133}Cs Depth (μK/W)	Power (W) for $3000E_r$ ^{87}Rb
X	79.0(7)	6.58(6)
Y	77.8(2)	6.67(2)
Z	65.5(9)	7.9(1)

Table 5.2: Lattice depth calibrations measured by Kapitza Dirac scattering

5.5 Observing the Superfluid - Mott Insulator transition

As outlined above we expect two distinct ground states of the Bose-Hubbard model: a superfluid phase which retains the global phase coherence of a BEC and a Mott-insulating phase where atom number fluctuations are suppressed. These phases are linked by a quantum phase transition. Unlike a classical phase transition, this occurs at zero temperature and is driven by changing the many-body Hamiltonian rather than temperature [249]. We can observe the effects of this phase transition experimentally by loading a BEC into our optical lattice. As well as providing a demonstration of the physics discussed in this chapter, these experiments allowed us to confirm that our optical lattices were well-controlled and behaved as expected.

We can prepare low entropy states in a lattice potential by adiabatically ramping on the lattice beams around a BEC. There are two timescales which need to be considered for this loading to be adiabatic [112]. First, as discussed earlier in section 5.2.1, the lattice ramp must be adiabatic with respect to the band gap. In this case, the usual Landau-Zener criterion applies, where we consider the gap between Bloch wave states $|\psi_q^n\rangle$,

$$|\langle\psi_q^n| d/dt |\psi_q^0\rangle| \ll |E_{n,q} - E_{0,q}|/\hbar. \tag{5.27}$$

This criterion is calculated in [63] as $|\frac{d}{dt}V_0/E_r| \ll 32\sqrt{2}E_r/\hbar \approx 4\times10^5\ \mathrm{s}^{-1}$ for ^{133}Cs in our lattice, and so is easy to achieve if the atoms occupy low-lying momentum states initially.

Second, the ramping on of the lattice must be adiabatic with respect to the motion

of the atoms in the harmonic trapping potential, which arises from a combination of the original dipole trap and the Gaussian envelope of the optical lattice beams. This can be expressed as the need to maintain a uniform chemical potential over the lattice $\mu_0 = V(r) + U\bar{n}(r)$. Since equilibration relies on the slow process of atoms redistributing within the trap this time scale is often much slower than the band gap time scale. Even though there is a weak increase in U with V_0, it doesn't fully compensate for the change in confinement. For example, $U \approx \frac{1}{20}V_0$ for ^{87}Rb in our lattice. One way to get around this is to control the confinement potential independent of the lattice depth using a dipole trap [305]. In our case the BEC is formed in a trap with trap frequencies around 30 Hz and the lattice confinement frequency is around 30 Hz at 10 E_r[8].

The two ground states of the lattice can be distinguished via time-of-flight (TOF) imaging [114], which images the momentum distribution. After TOF, the position of an atom with momentum $\mathbf{k}$ is given by $\mathbf{r} = \hbar\mathbf{k}t/m$. Due to interference between atoms on different lattice sites, the imaged momentum distribution is given by the product of an envelope function determined by the Fourier transform of the Wannier function (a Gaussian envelope) and a structure factor which accounts for the interference between atoms expanding from different lattice sites [101],

$$n(\mathbf{k}) = \underbrace{|\tilde{w}(\mathbf{k})|^2}_{\text{Wannier envelope}} \underbrace{\sum_{i,j} e^{i\mathbf{k}\cdot(\mathbf{r}_i - \mathbf{r}_j)} \left\langle \hat{b}_i^\dagger \hat{b}_j \right\rangle}_{\text{Lattice interference}}. \tag{5.28}$$

In the case of the superfluid, where there is off-diagonal long-range order [311], there are many interfering terms in the structure factor sum, which yield sharp interference peaks at the reciprocal lattice points, weighted by the Wannier envelope. In the Mott insulator $\left\langle \hat{b}_i^\dagger \hat{b}_j \right\rangle = \delta_{ij}$ and the sum is simply a constant, yielding the Gaussian Wannier function.

As discussed in section 5.2.3, the Bose-Hubbard model ground state is determined by the competition of interaction energy with kinetic energy. At a fixed density, this is determined solely by the ratio U/Jz, where the coordination number $z = 6$ for a cubic lattice. In systems where we can tune the atomic interactions with a Feshbach

[8] Calculated using Eqn. 2.71 from [305]

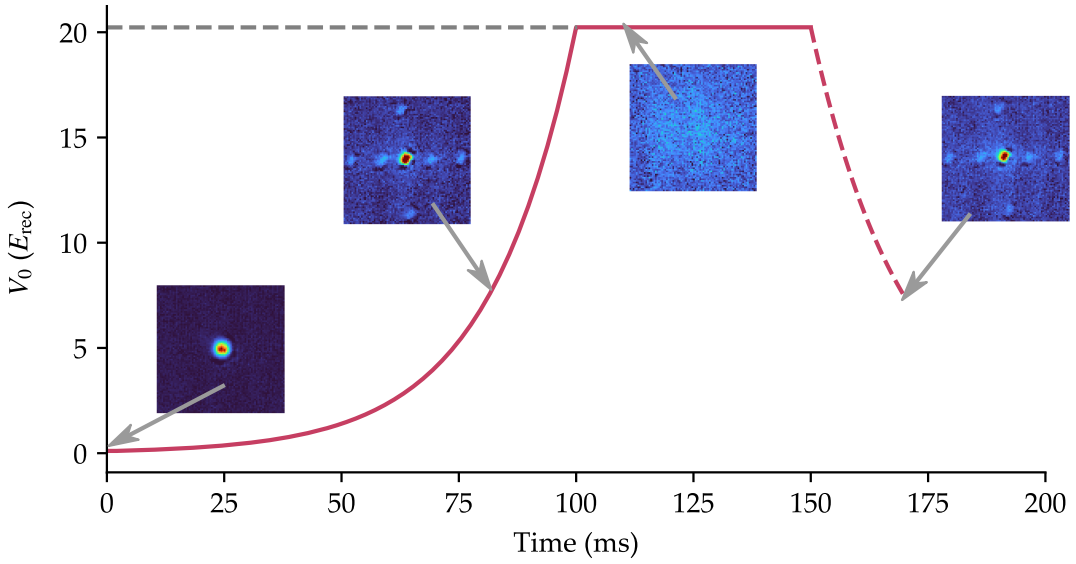

Figure 5.8: Ramp used to prepare superfluid and Mott insulator ground states, along with representative TOF images. TOF images of ^{133}Cs at 22 G are shown after releasing the cloud at various points in the ramp (0 E_{rec}, 8 E_{rec} 20 E_{rec} and 8 E_{rec} after ramping down). Note that the imaging axis is angled at 60 degrees to the lattice axis, as shown in Figure 5.6, and so all 6 1st-order diffraction peaks are visible. The sudden loss of coherent momentum peaks shows the system has entered the Mott insulator phase, and the restoration of coherence after ramping down the lattice proves that the loss of coherence is not simply due to increased entropy.

resonance, we can independently tune U/Jz by varying either the scattering length or the lattice depth.

In our experiment, we can observe the superfluid and Mott insulator phases by starting from the ^{133}Cs BEC sequence described in Chapter 4. Keeping the dimple trap on at the evaporation ramp endpoints we first set the magnetic field to set the scattering length using the broad low field Feshbach resonance. We estimate the scattering length that the field setpoint corresponds to using calculations from Jeremy Hutson's group and a magnetic field calibration based on $^{133}Cs_2$ Feshbach resonances. After allowing 50 ms for the magnetic field to settle, we ramp up the lattice using an exponential ramp over 100 ms, starting at 0.1 E_{rec} ending at $20E_{rec}$. To observe the momentum distribution we suddenly turn off all optical traps in less than 10 µs. Figure 5.8 shows this ramp, and

representative TOF images to illustrate the behaviour.

Depending on the scattering length and the final lattice depth we observe differing contrast in the atomic diffraction pattern, which allows us to differentiate the two Bose-Hubbard ground states, as shown in Figure 5.9. For moderate V_0 the first and second-order reciprocal lattice peaks are clearly visible. Note that the images are taken at an angle to the lattice beams and show a projection of a cubic momentum space lattice. For larger lattice depths and scattering lengths, the visibility of the interference pattern decreases.

To prove that the loss of coherence is due to interactions and not just increased entropy we can reverse the lattice power ramp and recover superfluid coherence, and eventually the original BEC phase. Since any process that adds entropy must be irreversible, the recovery of the superfluid order proves that the system was still close to the ground state. This is shown in Figure 5.8. We do see some loss of atoms, likely due to three-body loss, however not enough to explain the complete loss of coherence in the Mott insulator state.

The images can be analysed to quantify the loss of coherence against the Bose-Hubbard model parameter U/Jz. We calculate U/Jz for each set of experimental parameters using the formulae given in section 5.2.2, assuming a 10% uncertainty in the atomic scattering length and 5% uncertainty in the lattice depth. To quantify the coherence we measure the relative height of the lattice diffraction peaks using the visibility method [102]. We compare the optical density at two points, one centred on a 1st order diffraction peak, denoted $n_{\max}$, and another centred at the same momentum magnitude but 45 degrees offset on the circle of constant $k = 2\pi/a_{\text{lat}}$, denoted $n_{\min}$. This is illustrated in figure 5.10 (a). By defining the visibility,

$$\mathcal{V} = \frac{n_{\max} - n_{\min}}{n_{\max} + n_{\min}} \tag{5.29}$$

it is possible to divide out the Wannier envelope in equation 5.28 to measure the atomic coherence.

The results of a visibility analysis on our data are shown in figure 5.10 (b). From mean-field theory, it is expected that beyond a critical $U/Jz = 5.8$ the system will transition in regions where the density is such that the local ground state is no longer the

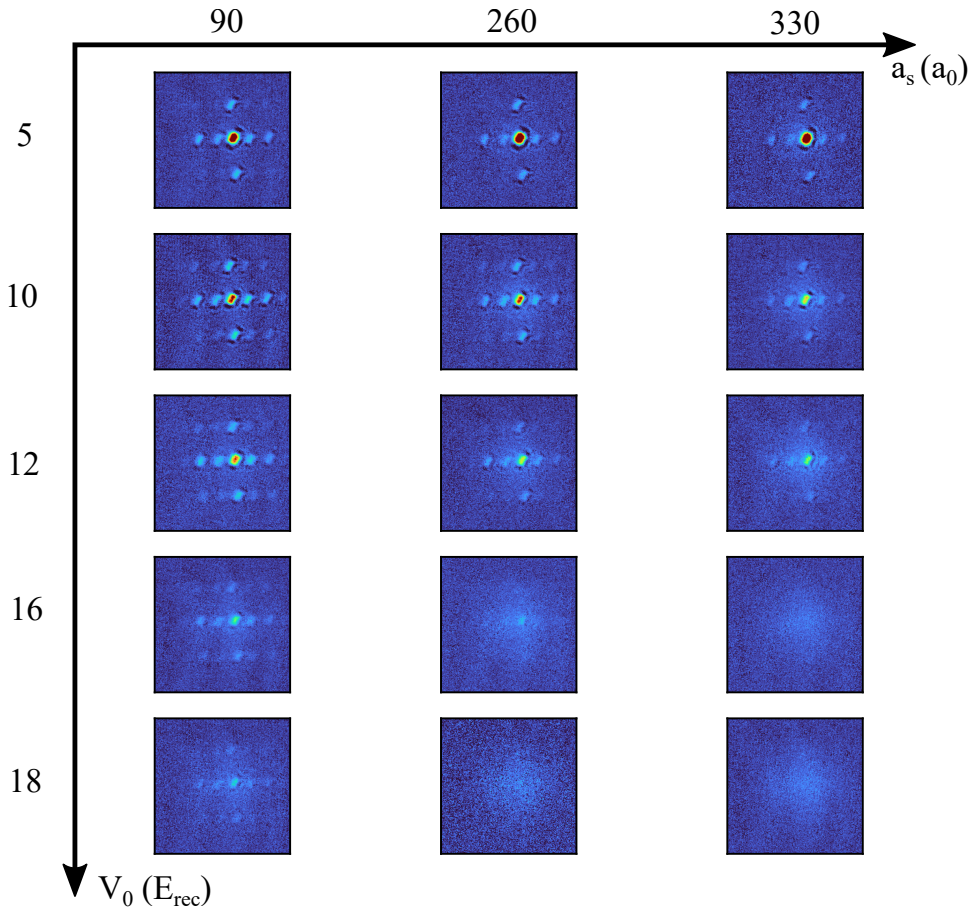

Figure 5.9: SF/MI transition as a function of both the lattice depth and the atomic scattering length. Absorption images are shown with a fixed colour scale for ^{133}Cs atoms at various lattice depths and scattering lengths. There is a significant uncertainty on the scattering length of around ±10%

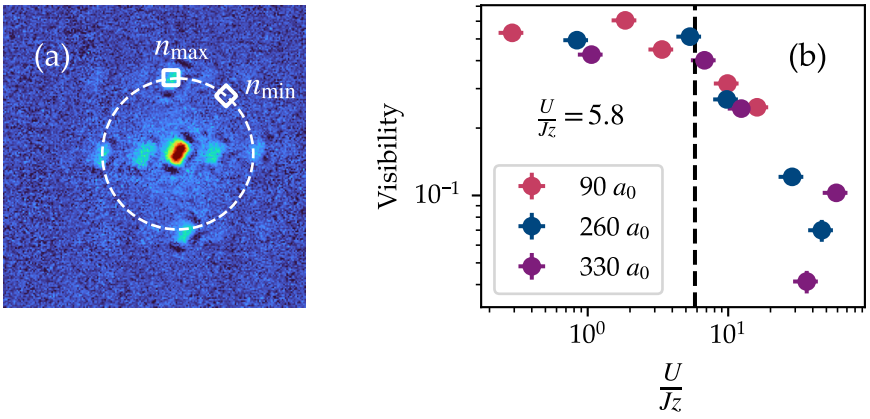

Figure 5.10: Analysis of data in figure 5.9 based on the visibility method [101]. We compare the mean column density in TOF images at two points on a circle of constant momentum, indicated by boxes in (a). We compare two points, one at a diffraction peak, labelled $n_{\max}$ and another at a point equidistant between two peaks $n_{\min}$. The visibility is defined as $\mathcal{V} = (n_{\max} - n_{\min})/(n_{\max} + n_{\min}.)$, and is plotted against the Bose-Hubbard model parameter U/Jz. The mean field critical value of $U/Jz = 5.8$ is indicated with a dashed line.

superfluid phase. Two effects lead to finite visibility beyond the critical U/Jz. First, the variation in density across the trap leads to some regions still having a superfluid local ground state. Additionally, even in the Mott insulating regions, the ground state still has an admixture of particle-hole pairs. These consist of an additional particle at one lattice site and a missing particle at a neighbouring site. These pairs restore short-range coherence to the Mott insulator, leading to a finite visibility in the Mott phase which is proportional to Jz/U [102]. This theory broadly agrees with our results, where we see that when expressed in terms of the combined parameter U/Jz the three data sets overlap reasonably, and show the expected reduction in visibility beyond the mean-field critical point.

The data and experiments described in this section are very preliminary, and many other experiments could be done to characterise the preparation of Mott insulating states, especially with ^{133}Cs where low-field Feshbach resonances are available. For example, it is possible to determine the number of evenly occupied sites in the lattice by forming

$^{133}Cs_2$ molecules [258, 239], which would be a helpful measurement for our experiment where a unity filling Mott insulator of each species is the ideal starting point. Additionally, the Mott insulating phase has an excitation gap and therefore shows distinct resonances in a modulation spectrum [114]. A very thorough characterisation of a ^{133}Cs lattice system via modulation spectroscopy has been reported in [193]. These methods will be useful for later work in using ^{133}Cs Mott insulators to prepare $^{87}Rb^{133}Cs$ molecules following the method in [239], or other experiments using our quantum gas microscope but for now, we pass on these experiments to work on demonstrating quantum gas microscopy and the preparation of molecules.

Chapter 6

Single Site Resolved Fluorescence Imaging

The main goal of our experimental apparatus is to demonstrate single-site resolved imaging of molecules in optical lattices. As there are no closed cycling transitions in the bialkali molecules we will work with, this requires imaging the constituent atoms after dissociation. This chapter details the design and preliminary characterisation of atomic high-resolution imaging in our experiment.

Single site-resolved fluorescence imaging, also known by the more memorable term quantum gas microscopy, has emerged as a crucial technique for studying ultracold lattice systems [118]. The term quantum gas microscopy is usually used to describe imaging of atoms in a 2D Hubbard-regime optical lattice where information about the local density is extracted at a single site level. In this context, Hubbard-regime roughly means a lattice where ultracold atoms are free to tunnel around and interact such that the super-fluid/ Mott insulator transition can be observed. This is in contrast to earlier experiments which demonstrated single-site resolved imaging of non-degenerate samples in large spacing lattices [218]. The first quantum gas microscopes were first developed for ^{87}Rb [10, 265] where these pioneering experiments used single atom resolved control and readout to study quantum phase transitions [9, 265, 86], resolve few body correlations [43, 236], observe magnetic ordering in optical lattices [267, 97] and experimentally probe the relationship between thermodynamics and entanglement in closed

quantum systems [141, 49, 149]. Around 2015 a second wave of microscopes emerged using different atomic species, allowing the study of fermionic Hubbard models [45, 29, 111] which are of special interest in the quantum simulation of high-T_c compounds, and electronic effects where fermionic statistics are important. Given the usefulness of microscopy in experiments with ultracold atoms, there is abundant motivation to apply the technique to molecules. A technique for molecular microscopy was proposed in [62] and is being pursued experimentally in a few other molecule labs [99, 61], most notably the ^{23}Na^{87}Rb experiment at Princeton where single site-resolved imaging of molecules has been demonstrated [243, 52].

The chapter is structured as follows. Section 6.1 gives a technical literature review of the quantum gas microscopy method. This will give important context to Section 6.2 which discusses the design of our microscope. Section 6.3 details the algorithms used to reconstruct the atomic density. Sections 6.4 and 6.5 present our preliminary experimental work on fluorescence imaging of ^{133}Cs.

6.1 Quantum Gas Microscopy

Achieving single site-resolved imaging in the Hubbard regime is a technical tour-de-force. For the sake of discussion, we can separate the challenge into four interrelated components:

1. An optical lattice. In most implementations, this must be deep enough to pin the atoms to their sites while they fluoresce.

2. An imaging system with high enough spatial resolution to resolve the lattice. This requirement can be made less strict by careful image analysis.

3. A method to reliably prepare low entropy 2D gases, as any out-of-focus atoms will confuse the analysis of the images.

4. A method for exciting fluorescence without the atoms leaving their sites. Usually laser cooling, but in some cases, a fast cycling transition is used.

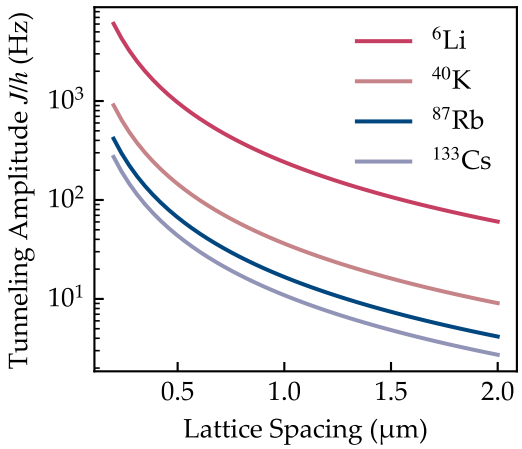

Figure 6.1: Tunneling rate of lattices with variable spacing, calculated for a depth $V_0 = 9E_{\text{rec}}$. The difference between the species and the dependence on lattice spacing arises from the absolute scale of $E_{\text{rec}} = \frac{h^2}{8ma_{\text{lat}}^2}$

This section describes generally how these four components are implemented. Appendix A gives a table of how different published experiments achieve quantum gas microscopy, illustrating the diversity of approaches used.

6.1.1 Optical Lattices for Microscopy

In microscopy experiments, there are two roles played by a lattice. In the "science" phase the lattice is used as the potential in which the quantum dynamics and phase transitions take place, and this lattice must be imaged with single-site resolution. In most experiments, during the imaging phase, the lattice must hold the atoms in place while they fluoresce. These two steps (science and imaging) can be handled by different lattices, as in [10, 223], but usually, there is one lattice which is ramped up to a high depth during imaging [265].

The science lattice geometry is specific to the individual experiment's goals. To observe the Mott transition, the science lattice must have a short enough spacing for tunnelling to happen on a reasonable time scale compared to the lifetime in the lattice. As discussed in Chapter 5, for most atomic species the phase transition occurs around

5 - 10 E_{rec}. To ensure a good ratio of tunnelling rate to decoherence rate, the lattice spacing must be smaller than 1 µm for most elements, or closer to 3 µm for the exceptionally light Li species. This is illustrated in Figure 6.1. In the first experiments, square lattices were used for simplicity, but more recent machines have implemented triangular lattices where more exotic physics can be studied [307, 314]. Other experiments gain added control over the sample through the use of super-lattices [162, 180, 304].

The vertical lattice spacing only impacts the physics of the 2D Hubbard model via the changing the strength of interactions $U \propto 1/a_z$, and so a larger spacing can be used to facilitate the preparation of a 2D layer. Many groups use a shallow-angle or accordion vertical lattice. There is an upper limit on vertical lattice spacing set by the depth of field of the microscope, as the fluorescing atoms must be confined to within the depth of field to keep the resolution of the imaging high. Typically the depth of field $z_{\text{dof}} \approx \lambda/\text{NA}^2 \approx$ 3 µm.

A common feature for all microscope science lattices is a low-noise laser system to avoid heating, an example of the technical implementation can be found in [25]. Er or Yb-doped fibre amplifiers with low noise seeds and Ti-Sapphire lasers are commonly used.

During imaging, unless the species has a very broad transition which allows μs scale imaging times [207, 277], the lattice must hold the atoms on their sites. Typically the required depths are around 1000-5000 E_{rec}, which requires either near-resonant light [10] or high laser intensity [265]. Achieving these high depths also requires tightly focused beams, which can limit the system homogeneity.

6.1.2 High Resolution Imaging

Imaging the lattice structure requires a microscope with a resolution comparable to the lattice spacing. We can define the resolution of an imaging system using the Raleigh criterion: the intensity peak of one source must lie outside the first minimum of the second for two sources to be resolved, see Figure 6.2 (a). For microscopes with a circular aperture, this is the radius of the first Airy disk,

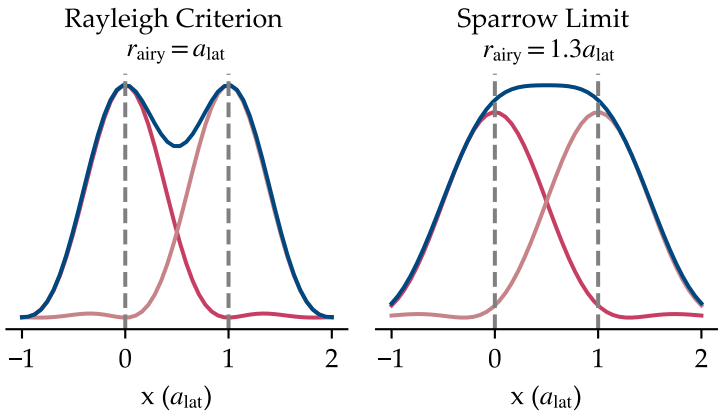

Figure 6.2: Diffraction limits in quantum gas microscopy. Two atoms are pinned to adjacent lattice sites and imaged with Airy point spread functions of radius r_{Airy}. At the Rayleigh limit defined as r_{Airy}=a_{lat}, there is a clear minimum between the sites. The Sparrow limit is defined as the r_{Airy} for which this minimum vanishes, and occurs around r_{Airy}=$1.3a_{\text{lat}}$

$$a_{\text{Airy}} = 0.61\frac{\lambda}{\text{NA}}, \tag{6.1}$$

where NA refers to the numerical aperture. Thanks to the underlying structure of the lattice, perfect reconstruction of the distribution of atoms is possible up to the Sparrow limit of $a_{\text{Airy}} = 1.3a_{\text{lat}}$ using simple deconvolution techniques [169], see Figure 6.2 (b). More advanced algorithms have allowed reconstruction up to $a_{\text{Airy}} = 2.2a_{\text{lat}}$ with fidelity above 96% [140]. The fidelity of these algorithms is improved by a high imaging signal/noise ratio. In section 6.3 these algorithms are discussed in more detail.

The optomechanical design of a quantum gas microscope objective lens needs to achieve a high numerical aperture whilst imaging a sample under vacuum, and allowing for optical access for all the beams used to trap and manipulate the gas. Currently, there are several methods in use, as illustrated in Figure 6.3. Perhaps the simplest method is to use a long working distance microscope objective outside the vacuum, corrected for the aberration induced by the few mm thick glass window [265]. (Figure 6.3 (a)). These are available commercially, but due to mechanical size constraints are limited to around

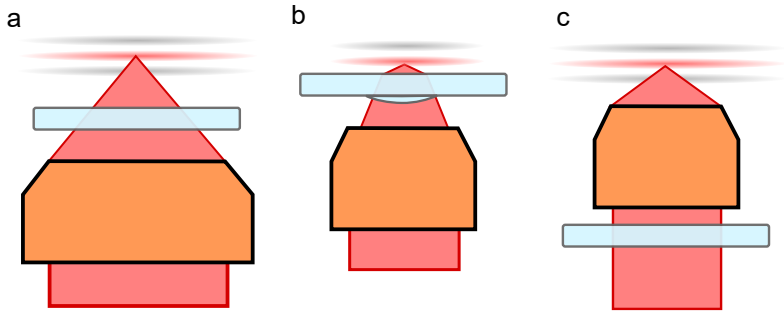

Figure 6.3: Most common optomechanical designs for high-resolution imaging. (a) Ex. vacuum long working distance (LWD) objective, corrected for the vacuum window. (b) solid immersion lens (SIL), which allows for improved numerical aperture at the expense of optical access. (c) In vacuum objective, specially designed for UHV compatibility.

0.8 NA.

Alternatively, a solid immersion lens [192] or in-vacuum hemisphere can be used as the first element of a microscope [10]. (Figure 6.3 (b)) These give an enhancement of up to n in the NA and can eliminate the need to correct the aberration from the vacuum window. Because of the very short working distance of these lenses, the cloud must be prepared within 10 µm of the glass surface, and all beams must either reflect off or be transmitted through the in-vacuum lens. Therefore, this method is not suitable for polar molecules or Rydberg atoms as they are very sensitive to stray electric fields from charges on the dielectric surface.

A third option is to have a long working distance objective inside the vacuum system, [272, 277]. (Figure 6.3 (c)) This gives high ≈ 0.9 numerical apertures and long working distances, but requires that the objective is made with low outgassing materials and mechanical methods (e.g. vented threads) which ensure UHV compatibility.

In our design for a microscope for polar molecules, a long working distance objective was chosen, as a SIL would risk uncontrolled electric fields from surface charges. For simplicity, we used a lens outside the vacuum system.

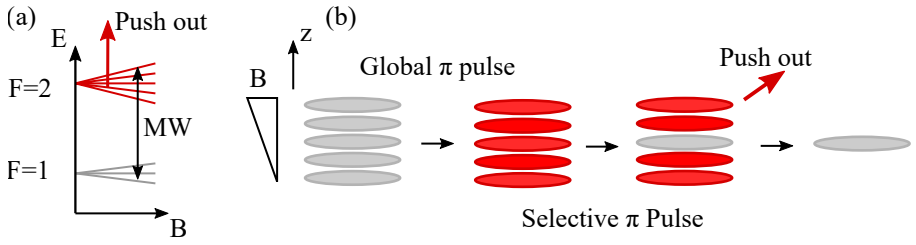

Figure 6.4: Overview of the microwave layer selection method, as applied to ^{87}Rb [303]. (a) Cartoon of the relevant level structure. The method relies on the Zeeman shift of the microwave (MW) transitions between states far enough apart in energy to allow selective optical removal. (b) Sequence to prepare a single layer. A large B gradient is applied. First, a broad MW pulse shifts the population to the removable state, and then a selective pulse "saves" one layer from optical pushout.

6.1.3 2D Gas Preparation

The depth of field of a microscope is given by $z_{\mathrm{dof}} \approx \lambda/\mathrm{NA}^2$, and so in most cases, it is necessary to prepare the atoms in a single plane of a vertical lattice to avoid out of focus atoms complicating the analysis of images. 2D quantum gases are a field of study in their own right [208] and similar techniques are used in experiments on 2D gases in uniform potentials [296]. Broadly speaking there are two ways to prepare 2D gases: compressing the gas into traps with successively smaller vertical extent or selectively removing all but one layer of a vertical lattice.

In [103] the cloud was compressed into a single lattice layer using an evanescent wave trap, a method not yet replicated in another experiment, as far as the author is aware. A more popular compression method was introduced in [209] where the atoms are loaded into a tightly focused light sheet, formed by an elliptical beam down with a vertical waist around 10 µm. This compressed cloud is then transferred into a large-spacing vertical lattice, often an "accordion lattice" with variable spacing, which provides a straightforward way to further compress the cloud vertically.

Selective removal of planes requires no additional optical potentials but has its own challenges. The most popular of these methods is microwave layer selection [93], which is very similar to techniques used in medical MRI. A magnetic field gradient of around 50 - 100 G cm^{-1} from a vertically offset quadrupole is applied to the cloud to give

each layer a different hyperfine transition frequency, with typical spacings of a few mG per layer equating to around 10 kHz microwave detuning per layer. The target layer is shelved to the other hyperfine F state so that all the other layers can be removed with a resonant light pulse. The technical challenge is achieving a highly stable magnetic field so that the narrow microwave transition is resolved and doesn't drift over time. Typical field stability requirements are on the order of 1 part in 1×10^5. A similar spectroscopic selection method can be implemented in species with a narrow line transition [306].

6.1.4 Fluorescence and cooling

To faithfully resolve the position of single atoms within the lattice, the atoms must remain on their sites while they fluoresce. This is usually achieved by cooling the atoms using a laser cooling technique. Which fluorescence techniques can be used is dependent on the atomic species being imaged.

The simplest method is to use optical molasses or polarisation gradient cooling [66]. The cooling effect in optical molasses occurs from optical pumping between the m_F ground states as an atom moves through a polarisation gradient. Therefore it works best in species with resolved hyperfine structures, such as ^{87}Rb and ^{133}Cs. A further consideration is the lattice potential for the excited state, which renders this method impractical in ^{40}K where the excited state is strongly anti-trapped [46]. To ensure that every site in the lattice has a large enough polarisation gradient for cooling the interference pattern of the molasses needs to be averaged out by shaking the retroreflection and detuning the pairs of beams [303]. Typically around 1×10^5 photons per atom are scattered in exposure times around 1s.

To perform free space sub-doppler cooling of species with unresolved hyperfine structure a technique called grey molasses is often used [28, 89], and a similar lattice-based cooling method known as Electromagnetically-Induced-Transparency (EIT) cooling has been demonstrated in ^{40}K microscopes [127, 81].

Another method that works for more species than bright molasses is to make use of the optical lattice and perform Raman sideband cooling. In this method, a coherent 2-photon process resolves sidebands of the harmonic motional states $n \rightarrow n-1$. Optical

pumping between the two F ground states is used to carry away entropy, and so only the two F levels need to be resolved. This is in contrast to degenerate Raman sideband cooling where the pumping is between m_F sub-levels in the same F ground state. Raman sideband cooling is used routinely for microscopy of the light alkali elements Li [230, 223] and K [46].

In atoms with a two-electron level structure (e.g. Yb, Er, Sr...), the strong ${}^1S_0 \rightarrow {}^1P_1$ type transitions are a powerful tool for imaging. These transitions are around 5 times stronger than alkali D_2 line transitions and occur at short optical wavelengths around 400nm, which allows higher imaging resolution. Thanks to the large linewidth cooling is not necessary, for example in [206] the pinning lattice wavelength is tuned to provide very strong confinement in the excited state, pinning the atoms during a short 100 µs exposure without any cooling. A recent experiment with Er uses a 2D accordion lattice to expand the cloud before imaging with the fast 30MHz 401 nm transition in 8 µs [277].

One final consideration is that all fluorescence methods lead to on-site light-assisted collisions, and so most quantum gas microscopes often only image the *parity* of the atomic density. Schemes to get around this have been implemented, for example over-sampling the science lattice with a separate pinning lattice [222], and by using optical superlattices to offset the pairs vertically [235, 162, 129]. These schemes can also be used to fully resolve the spin distribution which is important for studies of quantum magnetism. Using superlattices also allows imaging of bilayer systems, which are of interest as analogues of condensed matter physics (e.g. bilayer graphene).

6.2 A Microscope for Molecules

Having reviewed the field, this next section discusses our quantum gas microscope design for RbCs molecules, focusing on the construction and characterisation of the high-resolution imaging system.

The optical lattice we use for fluorescence imaging is described in detail in Chapter 5 and is a 532 nm spacing $\lambda = 1064$ nm cubic lattice, where the vertical lattice is generated by retro reflection off the objective front face. This should ensure common

mode drifts between the objective and the vertical lattice position, however, it does risk the formation of extra lattices from any reflection off the AR-coated glass cell.

To prepare the 2D gas we planned to use the microwave layer selection method, this is discussed more in Section 6.4.

One advantage of working with Rb-Cs is that simple D_2 molasses fluorescence imaging works well for both species. This allows us to design a system that can image both species, which would allow for full rotational state resolved imaging of molecules, following the approach outlined in [62]. All that is needed is an objective which is diffraction limited at both of the imaging wavelengths.

Since we are working with polar molecules, our objective lens must have a long working distance to avoid surface charge effects. To keep the vacuum design simple we use an external objective corrected for the 3mm thick glass window. The custom-made objective is designed to have a minimal focal length shift between 780 nm and 852 nm[1]. The objective is designed to give a diffraction-limited performance at 0.7 NA, the maximum allowed by our square cross-section glass cell.

The objective is infinity corrected (i.e. collimates the fluorescence) with an effective focal length of 35.2 mm. We image the fluorescence using an EMCCD camera[2] with comparatively large 16x16 μm pixels. To adequately sample the lattice requires a magnification such that 1 lattice spacing is around 3-5 pixels on the camera. We achieve this using a 1000mm tube lens and a 4X magnifying telescope (f_1=50mm, f_2=200mm, with achromatic lenses to reduce aberrations) giving a nominal magnification of 114 X. This yields an effective pixel size of 0.127μm = a_{lat}/4.2 and sensor diameter of 61μm. The imaging system is modelled in Zemax ray tracing software, which calculates the diffraction-limited field of view as 60 μm. Zemax also allows us to calculate tolerances on the optical alignment of the system.

The mounting for the objective should allow for motorized control of the z-position, and easy adjustment of the tip-tilt and xy-position to achieve the required relative tilt and centring. We use a piezo-actuated three-screw kinematic mount[3] to achieve remote

[1] Special Optics 54-51-36

[2] Andor iXon

[3] Custom made by Radiant Dyes, with Physik Instrumente PiezoMike actuators

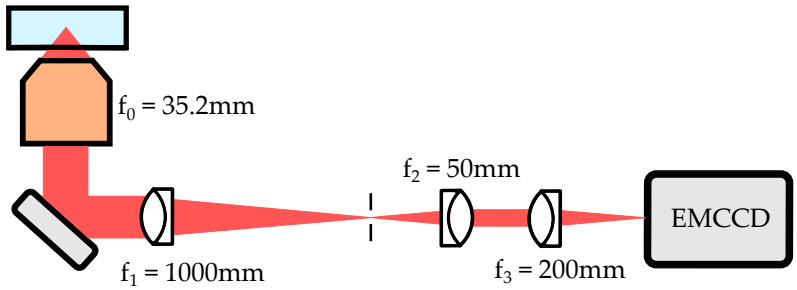

Figure 6.5: Optical Schematic for the high-resolution imaging system.

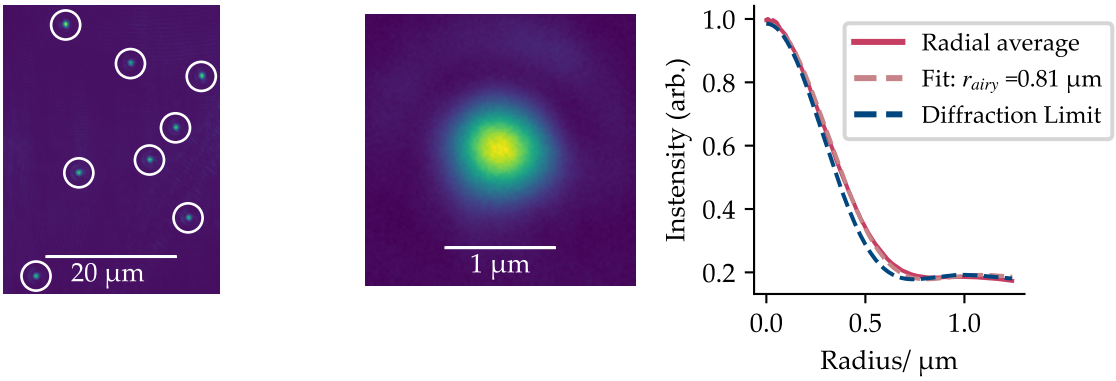

Figure 6.6: Testing of the objective at 852 nm using an ion-milled test target. (a) Raw image showing eight point sources. (b) Sub-pixel averaged PSF (c) Radial average of PSF, showing diffraction limit point spread function (blue dashed) and fitted Airy function with airy radius r_{Airy} =0.81 µm (pink dashed).

control of the objective z position and tip-tilt, mounted on thick aluminium posts to reduce sensitivity to vibrations. Fine adjustment of the x-y position is achieved through fine-thread screws which can push the mount across the optical table.

Before moving it into position around the glass cell, the objective was characterised using a test rig. This used an ion-beam milled test target manufactured by Joakim Reuteler at ETH Scope-M consisting of a pseudo-random array of 200nm diameter holes. The target was illuminated with 852 nm light from a laser diode, and the results are shown in Figure 6.6. To replicate the glass cell we use a test piece of the same thickness supplied by the cell manufacturer. Since the holes in the test target are prepared deterministically with <100 nm precision we can calibrate the magnification of the images simply by analysing the relative spacing of the point sources. Using this method

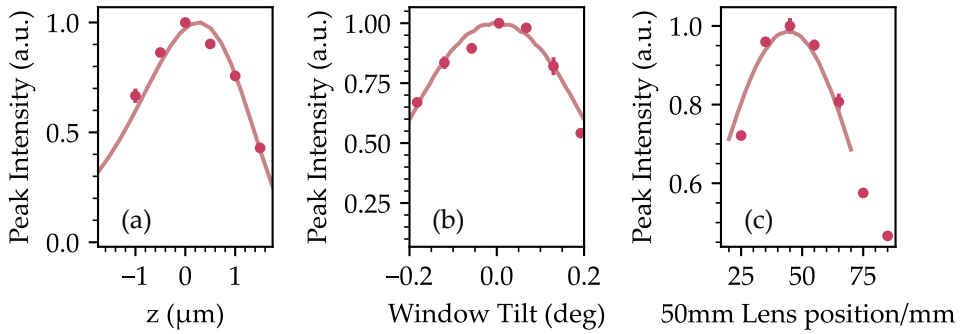

Figure 6.7: Comparison of Zemax ray tracing simulation and test target data. (a) Defocus or depth of field, changing the vertical position of the objective. Note that the asymmetric depth of field arises from residual spherical aberration. (b) The tilt of the glass cell w.r.t. to the objective (c) 2nd order misalignment where the objective -atom distance is corrected by a different telescope lens position. The x-axis is displacement relative to the nominal image plane of the 1000mm lens.

we found that the real magnification of the system when optimised was 121(1)X.

After optimising the objective z position, window tilt and tube lens positions the target was used to determine the point spread function of the microscope. The images were analysed by fitting a 2D Gaussian to each of the point sources individually, and then overlapping over-sampled copies to produce an average point spread function with less pixelation. The optimal Airy radius achieved was $r_{\mathrm{Airy}} = 809(8)$ nm, corresponding to an effective $\mathrm{NA}_{\mathrm{eff}} = 0.64$. This gives $r_{\mathrm{Airy}} = 1.52\ a_{\mathrm{lat}}$ for 852 nm and a calculated $r_{\mathrm{Airy}} = 1.39\ a_{\mathrm{lat}}$ for 780 nm, which should be sufficient to resolve the 532 nm lattice with the help of reconstruction algorithms. The focal length shift between 852 nm and 780 nm was separately measured with a SNOM fibre to be 0.8(1) μm [34], which, if needed, could be easily compensated with a separate imaging path for the two species as implemented in the MPQ ^{6}Li microscope [134]. During testing, we found that it is beneficial to aperture the beam to around 0.5" diameter at the focal point of the 1000 mm lens to eliminate caustics from stray light.

Using the test setup the effect of misalignment on the system was characterised, allowing comparison of the Zemax simulations to the real optical system. Figure 6.7

shows the depth of field, the effect of tilt between the objective and the glass cell window, and a 2nd-order misalignment where the object plane to objective distance is incorrect but is compensated by displacement of the first lens of the 4x telescope. Note that a $\delta f_2 = 10$ mm displacement of the $f_2 = 50$ mm lens corrects for approximately 10 μm displacement of the objective from the optimal position. In each case, the only free parameter in the theory curve is the offset of the x-axis, and so the good agreement shows that the Zemax simulation is faithfully reproducing the optical system.

Given that the glass cell bottom face must be perpendicular to the optical axis of the objective to within 2 mrad or 0.1° we took particular care to align the cell and objective. A laser guide beam was used to first set the rectangular glass cell to be aligned square to the optical table using retro reflections from two perpendicular horizontal faces, adjusting the cell by tilting the vacuum system around the bellows between the cell and MOT chamber. The optical axis of the imaging system was set square to the cell by retro-reflecting the guide beam off the bottom face of the cell using the periscope mirror of the imaging system, adjusting the periscope mirror to retro-reflect the beam. After mounting, the objective was set flat using mechanical limit switches located in the coil mount.

The final alignment of the objective to the atoms was facilitated by the weak transmission of the vertical lattice beam. This beam is retroreflected off the objective front face and is aligned to the atoms, and therefore it acts as a good definition of the optical axis. To get the correct alignment of the x-y position[4] of the objective we moved it such that the vertical lattice beam was centred on the periscope mirror of the imaging system. Using fine-threaded pushing screws while monitoring with dial gauges we were able to position the objective in the x-y plane with 10 μm precision. By aligning the z lattice transmission through the telescope and onto the camera we were able to get the image of the fluorescence on the camera.

[4]Same coordinate system used for the lattices: X = Horizontal parallel to transport, Y = Horizontal perp. to transport and Z = vertical

6.3 Image Analysis and Deconvolution

Although many QGM experiments work at resolutions below the Rayleigh criterion, single-site resolution is still possible thanks to the periodic structure of the optical lattice. This section details the code that was developed to analyse our microscope images.

6.3.1 Making simulated test images

By simulating the atomic fluorescence it is possible to develop and test image reconstruction algorithms without the need for experimental data. Simulating images also allows us to directly compare the reconstruction to the known atomic distribution. The protocol we used was similar to that which was independently reported in [169]. To generate images, we use the following procedure. First, we define a list of lattice points, (x_i, y_i), and a corresponding set of binary occupancies, n_i. To simulate the effect of spatially varying fluorescence, n_i are multiplied by prefactors A_i, with some variance $\Delta A_i/\bar{A}$. In the experiment, spatially varying fluorescence could be caused by e.g. variation in the molasses intensity. At this stage, we convert the representation to a matrix, where single pixels at the centre of each lattice site as it would appear at the camera image plane are assigned the values A_i and all other pixels are 0. To reduce digitization artefacts we oversample the camera pixels by a factor of 10. This image matrix is then convolved with an Airy disk point spread function normalised to unit height of width r_{Airy}. Gaussian noise of width σ_{BG} is added to simulate the effect of readout noise, photon shot noise and other background noise sources like stray light. We can define the signal-to-noise ratio as the peak counts per pixel from the atom signal to this noise level, i.e. $S/N = \bar{A}/\sigma_{\mathrm{BG}}$

6.3.2 Determining the lattice vectors and phases

The first step to reconstructing the lattice distribution is to determine the position of the lattice sites. For this, we follow the method described in e.g. [303, 44]. First using a blob detection algorithm[5] the positions of isolated atoms in the image are found, forming a

[5] Scikit-Image Blob LoG [291]

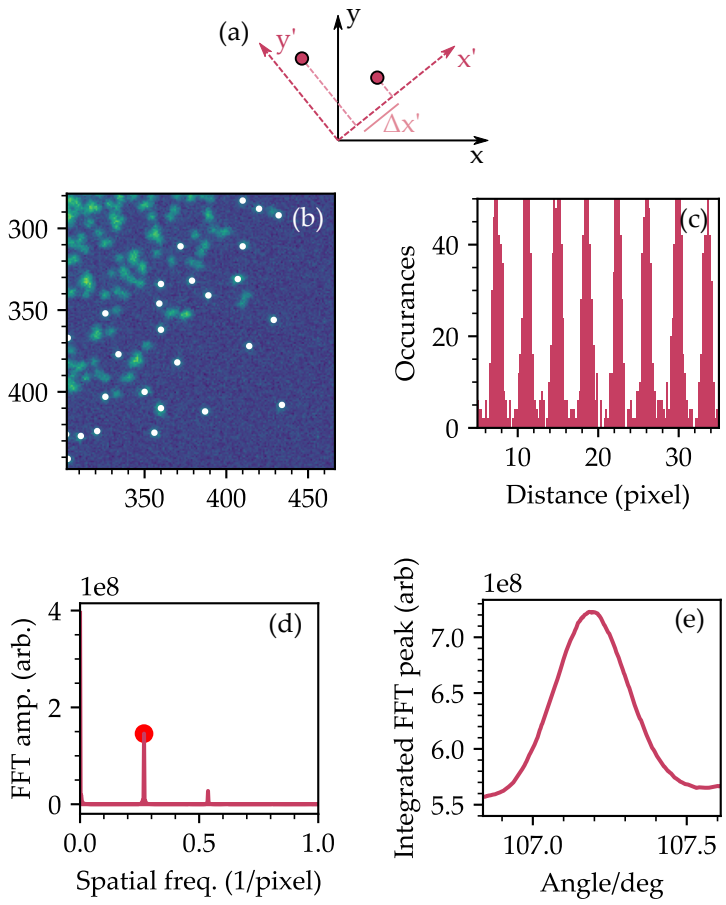

Figure 6.8: Determining the lattice angles and spacings. This is illustrated for one axis only, the process is repeated to find the orthogonal axis. (a) Finding one of the lattice angles requires finding the direction x' which is parallel to the lattice. This can be done by histogramming projected distances between atoms, $\Delta x'$. (b) Section of a simulated image, showing isolated atoms found by the blob detection algorithm. (c) Histogram of projected distances at optimal transform angle θ_x. (d) FFT of (c) shows a clear peak, which allows us to determine the lattice period. (e) Strength of the peak in (c) as a function of the lattice angle, showing we can precisely determine the optimal angle.

list (x_i, y_i) of lattice points. Exemplary results are shown in Figure 6.8 (b). The task is now to find the coordinate transformation of the form

$$\begin{aligned} x' &= x\cos\theta_y + y\sin\theta_y \\ y' &= -x\sin\theta_x + y\cos\theta_x. \end{aligned} \tag{6.2}$$

such that x' and y' are aligned with the lattice. Note that since the lattice need not be exactly square, θ_x doesn't necessarily equal θ_y. To find the optimal angles a histogram of all the relative distances between coordinates in the new basis (x', y') is formed, as illustrated in Figure 6.8 (a) and (c). When the new basis corresponds to the lattice directions, this histogram is periodic. The fundamental peak in the spatial spectrum, as shown in Figure 6.8 (d), allows us to determine the lattice spacing. By finding the angle with the highest fundamental peak we can accurately determine the lattice angle, as shown in Figure 6.8 (e).

Once the lattice vectors are known, the lattice must be matched to the image. This is done by searching for the optimal offset vector (x_0, y_0) such that there is minimal distance between the atom positions (x_i, y_i) and their nearest lattice site. It is well known that small fluctuations in the distance of the atoms to the lattice retro mirror can cause the lattice to move slightly in the image shot to shot, so this part of the analysis must be updated regularly. Fortunately, there are usually a few well-isolated thermal atoms around the edge of the cloud which can be used to pin down the phase of the lattice. To find the optimal lattice phases a candidate lattice is calculated and the distance of the closest site is averaged over a sample of up to 40 atom positions (x_i, y_i). A minimisation algorithm can be used to find the optimal phases.

6.3.3 Deconvolution and Thresholding

Once the lattice is determined the image must be processed if the large point spread function is too large to simply bin the counts to the lattice sites. The earliest experiments used a method where the image is reconstructed by placing a point spread function of variable height on each lattice site and then using a fitting algorithm to find the best reconstruction [303]. A faster alternative method is to use deconvolution algorithms and

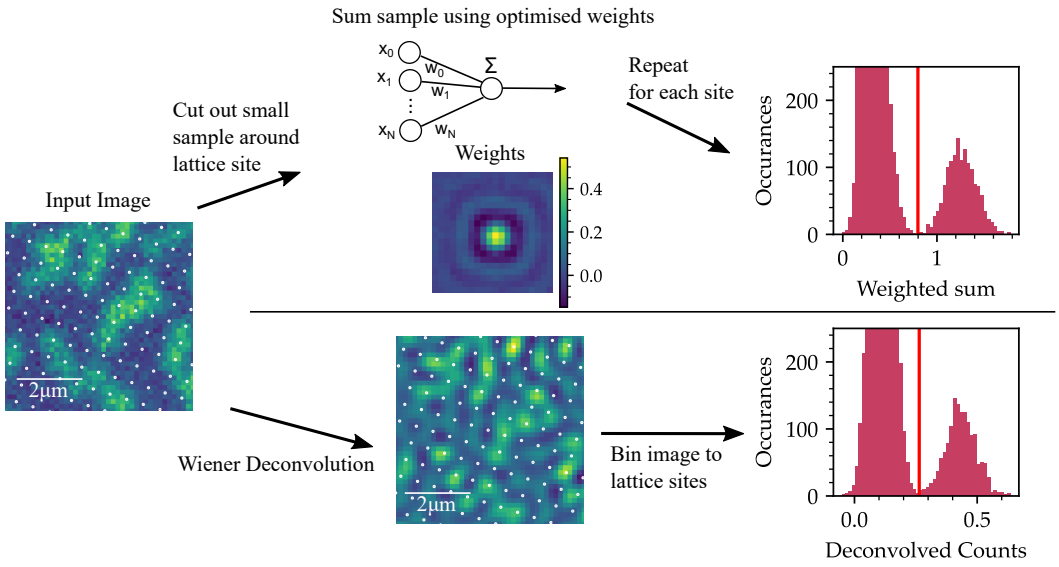

Figure 6.9: Overview of the two processing methods investigated in this work. The top path shows the "weighted sum" method based on a very simple neural network. Using the determined lattice sites a 20x20 pixel area is taken around a site, and summed with weights, shown in the inset. These weights are optimised using simulated data. The weighted sum is repeated for all sites to build up a histogram which can be thresholded to determine the site occupation. The bottom path shows the deconvolution method, where the image is first deconvolved using an Airy point spread function and then binned to the lattice sites to produce a histogram.

then bin the counts on each lattice site to produce a histogram which can be thresholded to determine empty and occupied sites, [44, 133]. A detailed comparative study of these methods showed that the deconvolution approach outperforms the original fitting method both in time and in the robustness of the reconstruction to noise [169].

Recently neural-network based methods have been applied to the problem, which when appropriately designed can allow for the reconstruction of images well beyond the Sparrow limit [234, 140]. The method developed in [140] is particularly interesting as it is unsupervised, i.e. doesn't require simulated data for training. Deep learning methods can also account for non-linear phenomena such as super-radiance in the fluorescence.

In our work, we investigated two approaches, first a deconvolution approach using the Wiener-Hunt algorithm [139, 224, 291, 44] and second a method based on a very

simple neural network, loosely following [234]. The working principle of each method is illustrated in Figure 6.9. In the deconvolution method, the image is first processed with the known point spread function and then binned to the lattice sites to produce a histogram which can be used to determine the occupancy. The neural network-based method iterates through each site, taking a 20 x 20-pixel sample of the image centred on the lattice site, which is fed into a single-layer neural network to achieve a weighted sum. The weights, shown in Figure 6.9, are trained using simulated data with a variety of noise levels and a point spread function corresponding to $a_{\mathrm{Airy}}/a_{\mathrm{lat}} = 0.7$. The output of the network is essentially a scaled histogram which can be used to determine the occupancy as in the deconvolution method.

To compare the performance of the two methods we define the fidelity of imaging as

$$F = 1 - \frac{N_{\mathrm{errors}}}{N_{\mathrm{sites}}}. \tag{6.3}$$

Figure 6.10 shows the measured fidelity for processing a 100 x 100 pixel simulated image with the pixel size/ lattice site ratio achieved in our experiment, as a function of resolution for various noise configurations. To give a more reliable measure of the performance F is averaged over five fillings in the range 10% to 90%. To assess the robustness of the two methods we compare the performance for differing levels of background noise and variation in the atomic fluorescence.

The two methods perform similarly, with the weighted sum method performing slightly better at low resolution. Note that the neural network weights were not re-optimised for every case as this is computationally expensive and also would lead to overfitting effects, however, the correct PSF size for each resolution was used with the deconvolution method. To improve performance further a more involved neural network approach could be implemented, following [140].

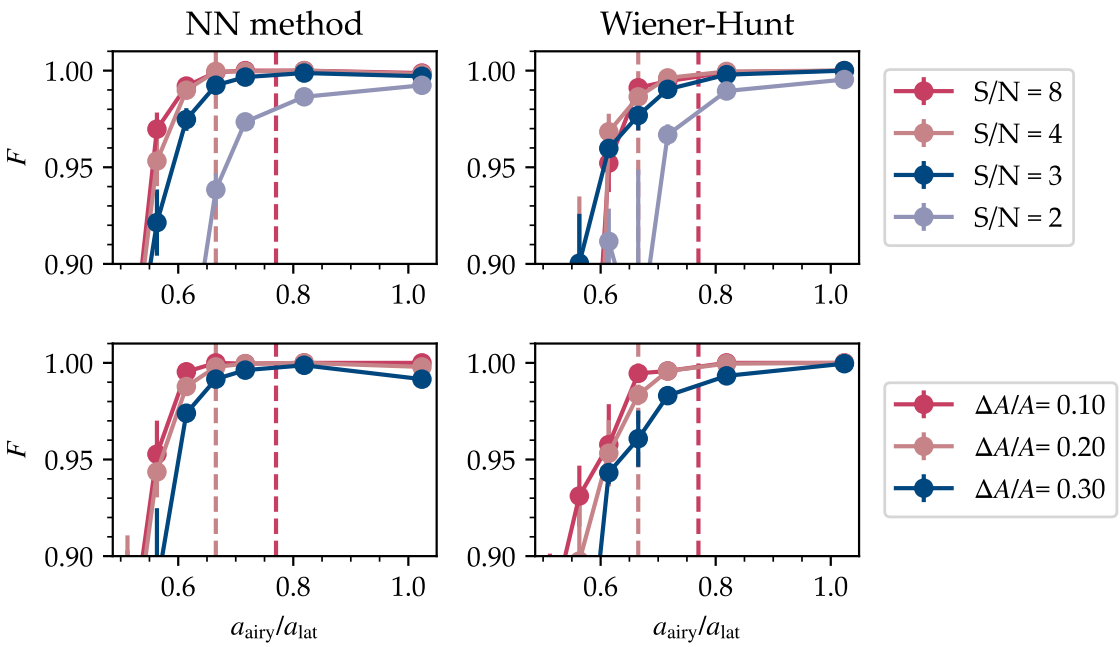

Figure 6.10: Testing the robustness of image analysis against finite resolution and noise. Each plot shows the calculated fidelity averaged over 5 lattice fillings, as a function of resolution defined as $a_{\mathrm{Airy}}/a_{\mathrm{lat}}$. To guide the eye $a_{\mathrm{Airy}}/a_{\mathrm{lat}}$ corresponding to the sparrow limit is marked with a dark dashed line, and corresponding to the resolution for ^{133}Cs expected from testing the objective is marked with a lighter dashed line. The left column shows results with the Neural-network method, and the right column shows the Wiener-Hunt deconvolution method. In the top row, we investigate the effect of adding more background noise, and in the bottom row, we add more variance in the atomic fluorescence.

6.4 Microwave layer selection

To prepare atoms in a single layer of the 532 nm spacing vertical lattice we planned to use microwave layer selection [93, 303]. This method has the advantage of not using up optical access in the horizontal plane and allows us to use a small vertical lattice spacing to achieve large interaction strengths (and therefore large mott insulators as discussed in Chapter 5). However, this method is known to be technically challenging and indeed has proved to be in our experiment. Although we have not yet demonstrated layer selection using this method, I will summarise the technique here and discuss our progress towards preparing a 2D gas.

The working principle of microwave slicing was introduced in Section 6.1, but to understand the technical challenge it must be considered in more detail. A large magnetic field gradient is applied to atoms in the optical lattice, using an offset quadruple similar to magnetic levitation. To reduce the curvature of the gradient a large offset field must be applied. The effect of curvature is illustrated in Figure 6.11 (a). Applying this large bias field with sufficient stability and low noise requires a highly effective current stabilisation system.

Once the magnetic gradient is applied, the atoms are first transferred to the upper hyperfine state using a broad microwave sweep, usually an adiabatic transfer achieved by sweeping the frequency over a large range. After this, a single target layer is transferred back using a spectrally narrow microwave pulse in a large magnetic field gradient. Amplitude-shaped and frequency-chirped HS1 adiabatic pulses [157] are used to give this pulse a top-hat spectral profile. A 100 G/cm field gradient produces a 5 mG shift between adjacent layers, which equates to a 13 kHz shift in the $|F = 3, m_F = 3\rangle \rightarrow |F' = 4, m_{F'} = 4\rangle$ transition in ^{133}Cs. Finally, a resonant pulse is used to push out all of the atoms that were not addressed, leaving a single layer in the optical lattice.

To control the hyperfine states in our experiment we used a printed circuit board antenna based on the design reported in [34]. To provide the microwave tone to the amplifier we used a function generator[6], amplified using a 3W amplifier[7]. Figure 6.11 shows a representative Rabi oscillation on resonance for the ^{133}Cs $|3, 3\rangle \rightarrow |4, 4\rangle$ transition.

Achieving successful microwave selection requires high-fidelity microwave transfer in a large magnetic field gradient, which can only be achieved in a very low magnetic field noise environment. We were able to demonstrate the required field stability with the magnetic field controlled by our shim coils, where we could measure transitions as narrow as 3 kHz wide, and observed a 1.8(3) ms dephasing time. However, when the high-current coils were used to control the field we observed around 100 kHz (50mG) variations in the field shot-to-shot. We concluded these must be caused by low-

[6] Windfreak SynthHD
[7] Minicircuits ZVE-3W-183+

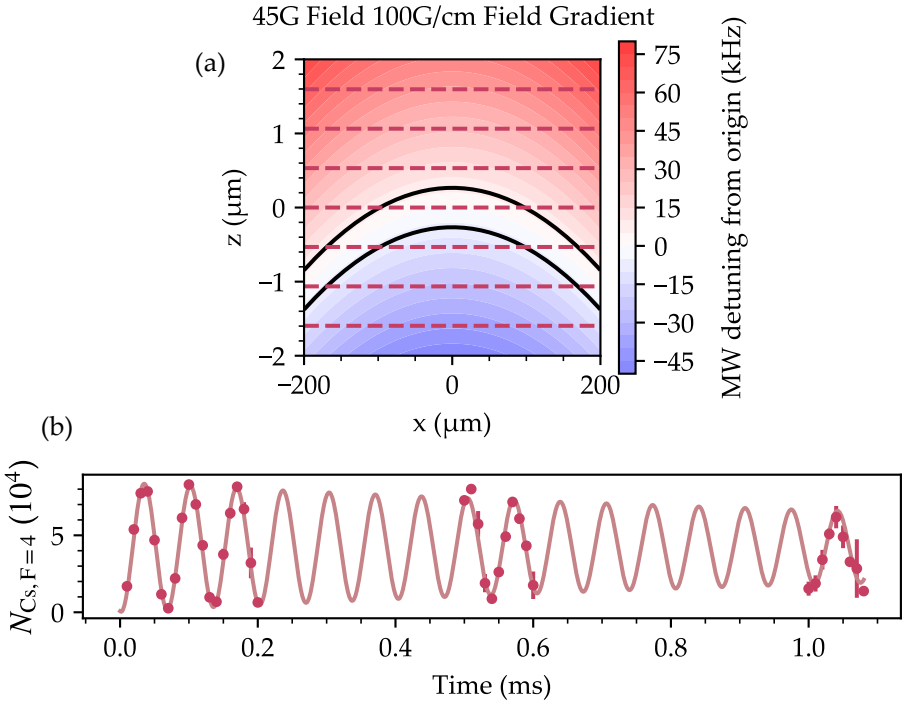

Figure 6.11: Practical aspects of layer selection. (a) Effect of field curvature on layer selection. The contour plot shows the microwave detuning as a function of space. Dashed lines indicate the position of lattice minima, and the black contours indicate the region that would be selected by a pulse which selects a single layer in the centre of the lattice. (b) A representative Rabi frequency measurement with, showing a 14.95(2) kHz oscillation, with an exponential time constant for dephasing of τ = 1.8(3) ms. This data was taken using only the low-current shim coils to control the field.

frequency noise as in some runs almost complete transfer was observed using a narrow 10 kHz sweep, whereas in other runs under the same conditions no transfer was observed. To improve the current stability we made sure to use thermally stable voltage references and resistors to set the servo setpoint and optimised the servo loop gain using an out-of-loop precision hall sensor. We also attempted syncing the microwave pulses to the mains 50 Hz cycle, however, this did not appear to impact the performance. In summary, we were not able to eliminate the shot-to-shot field variation, and therefore could not implement layer selection in the time allowed for this thesis work. In future we plan to perform a thorough analysis of the magnetic field around the atoms, and search for

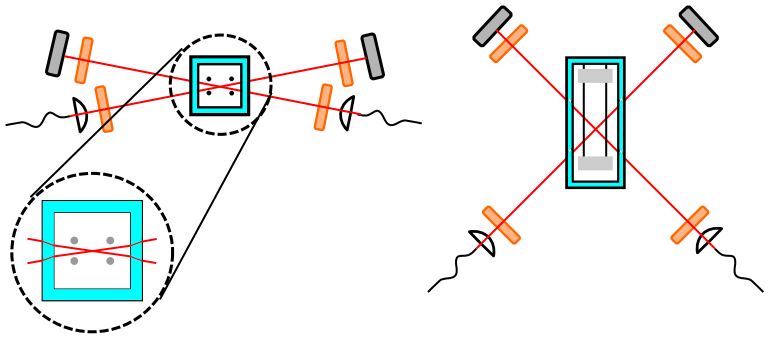

Figure 6.12: Optical Setup for fluorescence molasses. Left, a view looking down the transport axis of the chamber. Right, a view from above the glass cell looking along the vertical lattice.

ground loops in the servo and monitoring circuit we use for the high-current coils or similar technical problems that could be causing this unexpected large instability.

6.5 Molasses and Fluorescence Imaging

Even without the layer selection required for single-site resolved imaging, we can still demonstrate effective molasses cooling and perform preliminary work on high-resolution imaging of atoms in the lattice. Much of this work is still in progress at the time of writing.

To implement D_2 molasses cooling we use a four-beam configuration where the beams are tilted out of the horizontal plane by 8 degrees to give vertical polarisation gradients [243], as illustrated in Figure 6.12. Particular care must be taken in our setup to avoid these beams clipping on the electrodes, which can lead to a bright background in fluorescence images. The molasses setup is designed to allow for the modulation of the polarisation gradient interference pattern which is needed to avoid large variations in fluorescence between sites. Lightweight 1mm thick retro mirrors are mounted on piezo elements[8] to allow for modulation of the retro reflection phase and to allow a small controlled detuning between the beams each molasses beam frequency is controlled by an independent AOM and DDS. The power and detuning of the molasses

[8]Thorlabs PA4FKW, driven by Texas Instruments DRV2700EVM

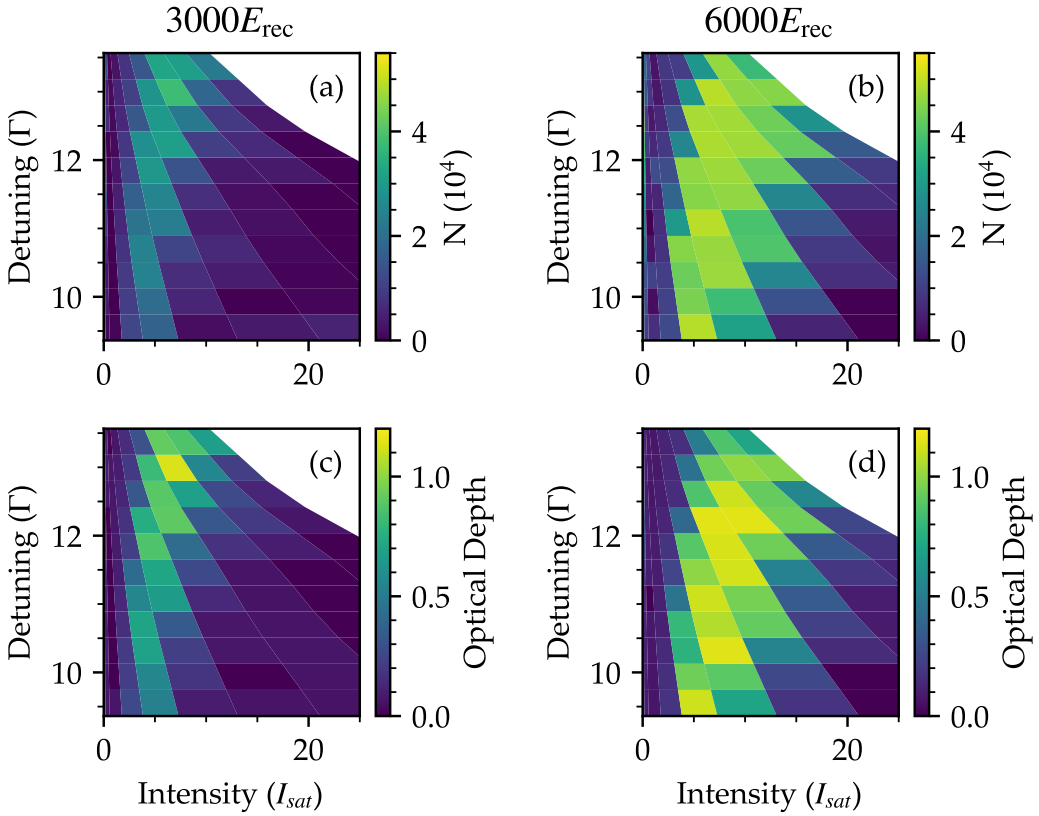

Figure 6.13: Optimisation of the optical molasses parameters, using the sequence described in the main text where the atoms in the lattice are exposed to 500 ms of molasses cooling. The top row ((a) and (b)) shows the atom number, and the bottom row ((c) and (d)) shows optical depth. The left column ((a) and (c)) is for a lattice depth of 3000 E_{rec}, the right column ((b) and (d)) is for a lattice depth of 6000 E_{rec}. High atom number and optical depth after 500 ms of molasses imply effective cooling. Cooling is much more robust in the deeper lattice, and as expected the molasses cooling requires more power at larger detunings.

beams are important parameters in the cooling. From previous experiments [303], and theory [266], we know that the molasses detuning should be several multiples of the linewidth red-detuned and that the total photon scattering rate should not exceed the lattice trapping frequency. Using the reported literature values we were able to get an initial fluorescence signal with which we could find the optimal shim coil setpoints to null the background field during molasses.

To optimise the molasses cooling further we used low-resolution absorption imaging. A thermal cloud was loaded from the dimple trap ($N = 1 \times 10^5$, PSD ≈ 0.1) into a deep lattice and imaged in absorption imaging after 500 ms of molasses. During loading the atom number drops by around 30%, presumably due to 3-body loss, and after a short pulse of resonant light to eject pairs we are left with around 5×10^5 atoms on singly occupied sites. By using low-resolution imaging we get a more quantifiable signal and we can image independently of the molasses' effectiveness.

Figure 6.13 shows the atom number and optical depth after release from the lattice as a function of the molasses power and detuning for two lattice depths. The molasses intensity in these plots is estimated from the power in the beams and the waist of the beam as estimated from the fibre collimator specification of $w_0 = 600\,\mu\text{m}$. Since we also have to extrapolate from the expected beam divergence to estimate the power on the retro path, there is significant uncertainty on the actual I/I_{sat}. It is also worth noting that to get the optimal imaging performance we needed to aperture and carefully align the beams so that they did not clip the electrodes, which further complicates estimating this quantity. A more accurate way to establish the intensity would be by using the atoms, e.g. with an optical pumping measurement, however, we have not yet had time to implement this. By contrast, the detuning is known precisely as it is well-calibrated by vapour cell spectroscopy and absorption imaging. By comparing to fluorescence images from the microscope we confirmed that the optima of these plots coincide with where we see the brightest fluorescence. We found that the cooling performance was not significantly helped by using both molasses beam paths, but rather simply depended on the total molasses power and the beam being retroreflected. This may indicate a technical problem with the molasses, or simply that the strong optical lattice is able to redistribute energy between the different spatial dimensions.

The atomic scattering rate as a function of detuning, Δ, and intensity, I, is given by [95]

$$\Gamma_{sc} = \frac{\Gamma}{2} \frac{I/I_{sat}}{1 + I/I_{sat} + (2\Delta/\Gamma)^2} \tag{6.4}$$

From this equation, and the known molasses detuning and estimated intensity, we can estimate that the optimal molasses parameters in the 6000 E_{rec} lattice correspond to a range of scattering rates between 50 and 70 kHz. Again the absolute scale of these numbers is subject to a large uncertainty from the uncertainty in estimating the molasses intensity.I/I_{sat}.

To establish the imaging resolution and demonstrate that the atoms stay on their sites during imaging we can prepare very dilute samples so that the signal from the in-focus layer is more clearly visible, as was done in [84]. This is done simply by using intentionally inefficient evaporation and loading a small MOT. The atoms are imaged onto the EMCCD for 1 s using the optimal molasses parameters from Figure 6.13 (I/I_{sat}=10, Δ =11 Γ, 6000 E_{rec} lattice), and 200x EMCCD gain. Figure 6.14 shows pairs of fluorescence images taken successively and the difference between the successive images. Using the blob detection algorithm on the difference image it is possible to estimate the loss rate and hopping rate. From a sample of 45 images with total N = 496 detected atoms, we find a fraction of 0.09 of the atoms significantly lose signal between the two images, and a fraction of 0.06 atoms hop to new locations and appear in the second image. These results are good for a preliminary effort but show that some further optimisation is required to improve the fidelity to the levels seen in other microscopes [303].

By fitting the brightest atoms in the same data set we can estimate the resolution of the imaging system following the same procedure as used with the test target. To calibrate the distance scale we assume the magnification observed in the test setup, as the lattice finding algorithm didn't converge well in these images with out-of-focus atoms. If we instead use the nominal magnification of the lenses gives a 5% larger point spread function radius. Ultimately the best way to calibrate the size of the point spread function is to determine the lattice spacing. Figure 6.15 (a) and (b) show that the

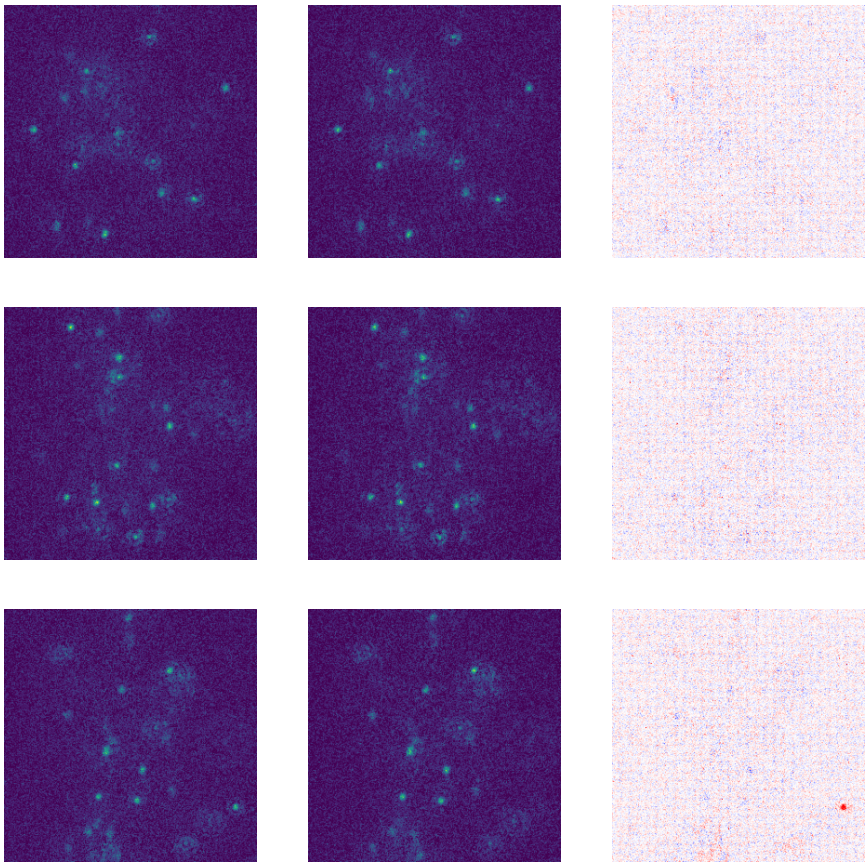

Figure 6.14: Example fluorescence images. Each row consists of two successive images and the difference between them, which shows any atoms which have been lost or moved during the imaging process.

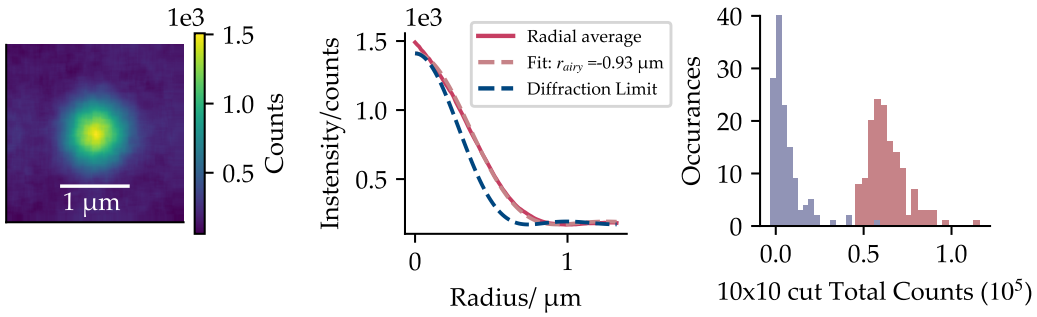

Figure 6.15: Data on the imaging of single atoms. (a) and (b) show the averaged point spread function (PSF) obtained from 20 images of a dilute cloud. The atomic PSF is larger than that observed in the test target, suggesting that further optimisation of the imaging system is required. (c) Comparing the summed fluorescence counts from 10x10 pixel regions centred around an atom (red) or randomly selected (blue).

atomic point spread function is significantly broader than the test point spread function, and we currently achieve a resolution relative to the lattice spacing of $a_{\mathrm{Airy}}/a_{\mathrm{lat}} = 0.56$, corresponding to an effective NA = 0.55. This larger Airy radius could be due to atoms in out-of-focus layers or indicate further optimisation of the imaging system is required. From visual inspection of the out-of-focus atoms, it appears that there is little coma or astigmatism, but there may be significant spherical aberration. This may be improved if a careful optimisation of the objective to atom distance is performed. It may also be the case that there is significant bowing of the glass cell, which could be compensated for with a correction plate.

To estimate the signal-to-noise ratio of the fluorescence imaging the average height of the atomic point spread function can be compared to the standard deviation of the background counts. By randomly selecting small sections of the image and calculating the standard deviation of the counts we can estimate the background noise to be around $\sigma_{\mathrm{BG}} = 150$ counts. We observe a observe mean atomic point spread function amplitude $\bar{A} = 1400$ counts and variance $\Delta A/A = 0.1$. Thus we estimate a signal-to-noise ratio of $\bar{A}/\sigma_{\mathrm{BG}} = 9.5$, which should facilitate deconvolution in an improved setup with effective layer selection. Figure 6.15 (c) shows a standard histogram measurement where we compare the total fluorescence from a region of 10x10 pixels around the atoms to a

selection of random background points in the image. We see that even in the presence of out-of-focus atoms there is still a clear distinction between signal and background.

Chapter 7

Outlook

This thesis has described the development and construction of a new apparatus for producing ultracold $^{87}Rb^{133}Cs$ molecules, with the aim of studying quantum many-body physics of molecules in optical lattices with single-site-resolved imaging. The implementation of dual-species laser cooling, optical transport and separate evaporation to degeneracy reported in this thesis are all key milestones towards a new molecule apparatus, and the construction of a high-power optical lattice and high-resolution imaging system lays the foundations for quantum gas microscopy of molecules in this apparatus.

Although much progress has been made in this work towards quantum gas microscopy of $^{87}Rb^{133}Cs$ molecules, it is clear that some steps remain in the path towards reaching this ambitious goal. To conclude this thesis I will give an overview of the plans for solving the current technical problems and upgrading the experiment to perform experiments with molecules and single-site resolved imaging of low entropy gases.

7.1 Dual-Species Degenerate Mixtures

The immediate next step for the experiment is to form ultracold molecules in the science cell, which requires a high phase-space density (PSD) mixture of the two species. Although we demonstrated the ability to form ^{87}Rb BECs in chapter 4, at the time of writing this thesis a change in the beam quality of one of the transport beams reduced the atom number in the science cell significantly. The first step towards molecules is

therefore to resolve this technical problem.

As stated in Chapter 2, the experiment was designed from the outset to implement the "all-optical" dual-species cooling methods used in the Innsbruck RbCs experiment [173], instead of the slower shared magnetic trap method used in the older Durham experiment [197]. The shared magnetic trap method relies on inter-species collisions for thermalisation and uses a large excess of ^{87}Rb to perform efficient sympathetic cooling. In the all-optical method, where loading of ^{87}Rb is limited, sympathetic cooling can be detrimental. In Innsbruck, the species were separated using two dimple traps, one which is made repulsive for ^{133}Cs using light at 830 nm [173] and to minimise mixing between the traps they were moved apart during evaporation, before being recombined after reaching BEC separately.

We plan to implement a variation on this scheme based on sequential loading of the two species, facilitated by our fast optical transport. Using time rather than species-specific traps to separate the species offers two valuable simplifications. First, it avoids the need to compromise between the species during the laser cooling steps, which allows optimal loading of the dipole traps for both species. Second, it eliminates the need for a bi-chromatic trap which requires careful optical design to ensure the two colours focus at the same point and also leads to loss of phase-space density due to near-resonant scattering.

The scheme is illustrated in Figure 7.1. First ^{87}Rb is cooled, transported to the science cell and loaded into a dimple trap formed by the crossing of one static beam and one beam which can move in the horizontal plane. A moving beam is used to move the atoms out of the path of the transport lattice, during this time ^{133}Cs can be cooled and loaded into the MC reservoir trap. ^{133}Cs is then transported to the science cell and transferred into a dimple formed by the static shared beam and a third beam. Evaporation proceeds by ramping down the shared beam and reducing magnetic levitation. This is done to minimise evaporation along the shared beam which would lead to inelastic inter-species collisions when evaporating atoms from one trap collide with atoms in the other trap. During evaporation, the bias field is set to the ^{133}Cs optimal values. At the end of the evaporation ramps the dimples are brought together to merge the species, forming

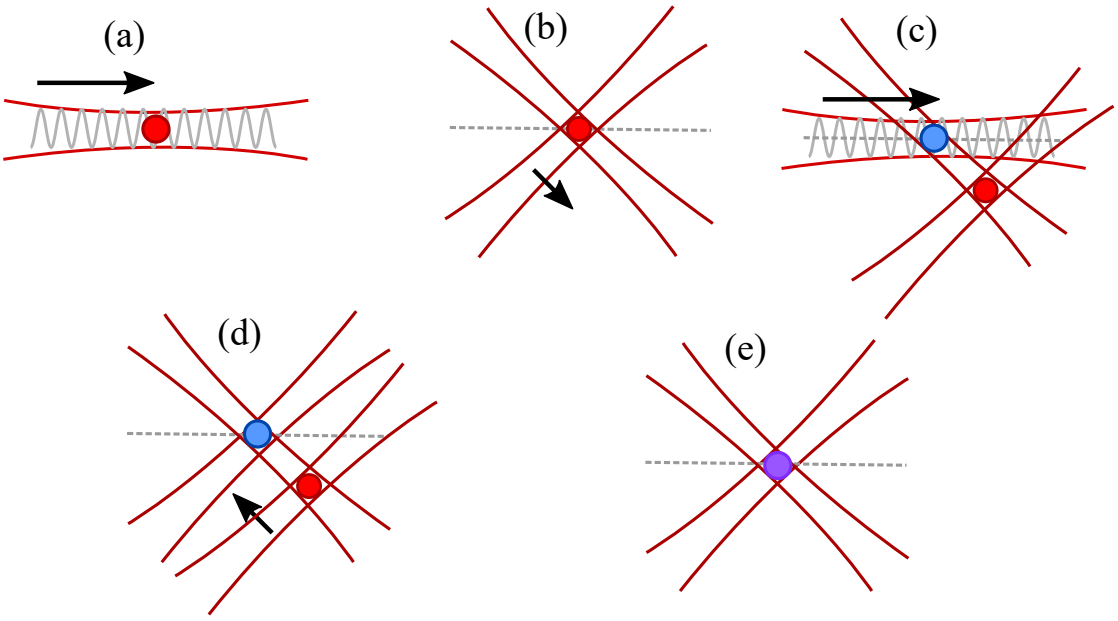

Figure 7.1: Sequential loading scheme using optical transport. (a) ^{87}Rb is cooled and loaded into the transport lattice, then moved to the science cell. (b) ^{87}Rb is transferred to a movable dipole trap and moved out of the transport path. During this time ^{133}Cs is cooled and loaded into the reservoir trap in the main chamber. (c) ^{133}Cs is transported to the SC (d) ^{133}Cs is loaded into a dipole trap formed by one of the Rb dipole trap beams and a separate beam. Evaporation then proceeds in these separated traps. (e) At the end of evaporation, the species are merged ready to form Feshbach molecules or load into an optical lattice.

the high phase-space density mixture required for magneto-association of molecules.

The moving beam apparatus required for this has already been built and tested by Adarsh Raghuram and is ready to add to the experiment in due course. It is based on a design reported in [240], where a piezo-actuated translation stage is used to move an optical fibre off-axis from its collimating lens. Since the optical system used to form the tightly focused trapping beam can be thought of as a magnifying imaging system with magnification given by the ratio of the trap waist to the fibre mode field waist, the motion of the stage is amplified by the magnification of the lens system. The piezo range requirement can also be reduced by reducing the crossing angle of the dipole trap beams.

We are also considering ways to improve the phase-space density of the atoms loaded into the transport lattice to allow larger phase-space densities in the dimple traps and ultimately improve the potential molecule number. One promising method is the dark-spot MOT [155, 152], where a spherical shadow of repump light is projected onto the MOT to reduce outward radiation pressure in the centre of the trap. This should be particularly helpful in improving the mode-matching between the MOT, DRSC lattice and reservoir trap, and also improve the elastic collision rate during the loading of the reservoir trap. Another proven method is to use a second pulse of DRSC one quarter oscillation period after loading the reservoir trap [173].

7.2 Forming Molecules

With the sequential loading sequence, we should be able to form high PSD mixtures with comparable atom numbers to the two previous ^{87}Rb^{133}Cs experiments, a good starting point for forming Feshbach molecules. We initially plan to produce molecules in a bulk gas, however, it may be beneficial to associate in the optical lattice to realise higher association efficiency [239].

To make ground state molecules we plan to use the same STIRAP scheme used in the older Durham experiment. The design for the system is much the same as that used in the older experiment [212], and the parallel experiment on RbCs in optical tweezers [125]. Note that this system is capable of performing STIRAP association near two different interspecies Feshbach resonances, one near 180 G as usually used in the older experiment, and another broader resonance at 350 G as is required for the lattice-based association method [67]. As of the time of writing the lasers we will use have been locked to the cavity. We are also planning on upgrading the locking system compared to the previous work by implementing feedforward to reduce intensity noise at the STIRAP Rabi frequency [179].

7.3 2D Gas Preparation

As discussed in Chapter 6, we are not yet able to perform quantum gas microscopy as we have not implemented a method for preparing degenerate 2D gases. In principle, there is no reason that the microwave layer selection should not work in our experiment, and so it should be possible with a detailed investigation into the observed magnetic field instability. However, the magnetic layer selection method is known to be challenging to perform reliably so it is worth considering if we can use a simpler method.

The most obvious alternative method would be to use a light sheet to load a single plane of a shallow-angle lattice. In our current setup, the electrodes limit the numerical aperture available from the side. If we assume a 1mm clearance is required to avoid clipping then the maximum opening angle is around 10 degrees, or 0.17 NA. This would allow us to realise a shallow angle lattice with spacings as low as 3 μm using 1064 nm light, or 1.5 μm using a repulsive 532 nm lattice, comparable values to those used in other microscopes. This technique has worked well in the MPQ ^{133}Cs microscope [140, 160], and so it can be assumed it should work in our experiment too.

7.4 Collisional Shielding of Molecules

A key requirement for quantum simulation with ultracold molecules is the preparation of low entropy states, and so it is worth considering how we could increase the phase-space density of a molecular sample formed by associating the atoms just above BEC, as is done in the two existing ^{87}Rb^{133}Cs experiments.

Evaporative cooling of molecules has recently become a possibility through the shielding of collisions, as discussed in Chapter 1. One particularly attractive option for ^{87}Rb^{133}Cs is resonant electric field shielding, which thanks to the small rotational constant can be implemented at relatively modest electric fields, as shown in Figure 7.2. Scattering calculations [217] predict a broad range of electric fields around 2.7 kV/cm where efficient shielding is expected, with a ratio of elastic to inelastic two-body collisions exceeding 1000 in the low energy regime realised in evaporative cooling.

Another interesting result of these calculations is that ^{87}Rb^{133}Cs has a moderate pos-

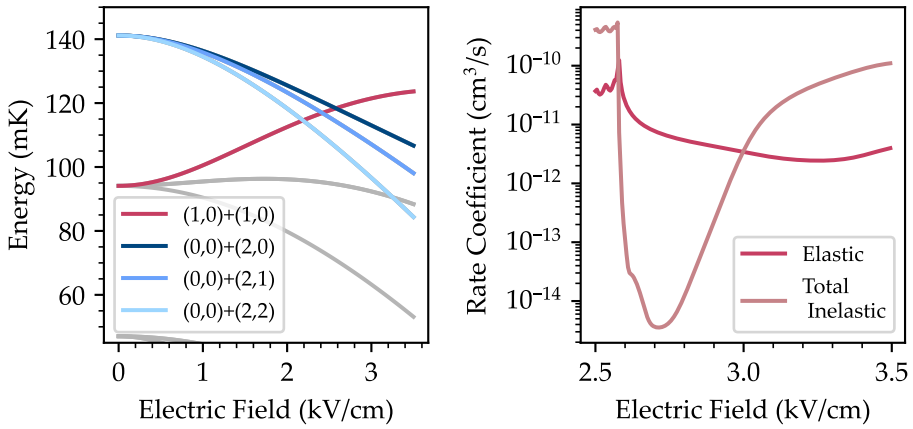

Figure 7.2: Electric field shielded collisions in RbCs. (a) Energy levels for pairs of molecules in different field-dressed rotational states $|\tilde{n}, m_n\rangle$. In the excited $|1,0\rangle$ state molecules can be brought into resonance with other channels leading to shielding [178]. (b) Calculated two-body rate coefficients in the shielded electric field region, evaluated at $E_{\mathrm{col}} = 10\,\mathrm{nK}$. This data is from calculations performed by Bijit Mukherjee and Jeremy Hutson [217].

itive background scattering length of around 150 a_0 in the shielding region, unlike most other bialkais. This would prevent BEC collapse caused by attractive interactions and may help stabilise a polar molecule BEC against 3-body loss caused by an excessively large a_0. There is surprising diversity in the expected collisional shielding properties of bialkali molecules, and so there is ample motivation for shielding experiments on as many species as possible.

Appendix A

Microscopy Literature Survey

This appendix aims to briefly detail as many quantum gas microscope experiments as I could find, detailing the key parts of the method as outlined in Chapter 6:

1. Lattice type, spacing and wavelength
2. 2D gas preparation method
3. Imaging system specification
4. Ratio $\beta = a_{\text{airy}}/a_{\text{lat}}$
5. Method used to collect fluorescence.

From this table, we get an impression of the development of the technique. Of course, no list like this will be complete, and the boundary between Quantum gas microscope experiments and other experiments such as tweezer arrays is becoming increasingly blurred, for example some of the most recent experiments [286, 316] do not use degenerate gases prepared by evaporative cooling but rather implement rearrangement with tweezers to prepare low entropy states. Unless mentioned otherwise the lattice type is square and formed by retroreflection.

Group	Date	Ref	Species	Lattice	2D Gas Method	Imaging System	β	Fluorecence method
Harvard	2009	[10]	^{87}Rb	Holographic projection a_{xy}=640nm a_z=1.5μm λ_S=758nm λ_P = λ_{D1}+10GHz	Evaneseant wave + magnetic trap loading 1.5μm vertical lattice [103]	In vac. Hemi-sphere NA = 0.8	0.92	D2 molasses λ_{im}=770nm
MPQ	2010	[265]	^{87}Rb	a_{xyz}=532nm λ=1064nm	MW selection	Long working distance NA = 0.68	1.4	D2 Molasses λ_{im}=780nm
MIT	2015	[46]	^{40}K	a_{xy}=541nm a_z=5μm λ=1064nm	MW selection	SIL NA = 0.87	1.2	Raman Side-band Cooling λ_{im}=770nm
Toronto	2015	[81]	^{40}K	a_{xyz}=527nm λ=1053nm	MW selection	200μm window + LWD objective NA = 0.8	1.3	EIT cooling λ_{im}=770nm
Strathclyde	2015	[127]	^{40}K	a_{xyz}=532nm λ=1064nm	MW selection	LWD Ob-jective NA = 0.68	1.3	EIT cooling λ_{im}=770nm

Group	Date	Ref	Species	Lattice	2D Gas Method	Imaging System	β	Fluorecence method
Tokyo	2015	[207]	^{174}Yb	a_{xy}=544nm a_z=5.2μm λ=1082nm	Two Accordion lattices and conveyor belt transport to surface of SIL	SIL NA = 0.81	0.74	Fast Imaging on 30MHz line, with deep excited state potential.
MPQ	2015	[223]	^{6}Li	Science: a_{xy}=1.15μm a_z=3μm Pinning: a_{xyz}=532nm $\lambda_{S,P}$=1064nm	1.7um waist light sheet	LWD objective NA = 0.5	0.8	Raman Sideband cooling
Harvard	2015	[230]	^{6}Li	a_{xy}=569nm a_z=1.5μm λ=1064nm	Accordian lattice	SIL NA = 0.87	1.15	Raman Sideband cooling (pulsed)
Kyoto	2016	[306]	^{174}Yb	a_{xy}=266nm a_z=5μm λ=532nm	Clock light selection	LWD Objective NA = 0.75	1.4	Narrow line molasses with short wavelength probe λ_{im}= 399nm
Princeton	2017	[36]	^{6}Li	a_{xy}=752nm a_z=3.5μm λ_{xy}=1064nm λ_z=532nm	5μm waist light sheet + 532nm accordion	LWD objective NA = 0.5	1.3	Raman Sideband cooling λ_{im}=671nm

Group	Date	Ref	Species	Lattice	2D Gas Method	Imaging System	β	Fluorecence method
Aarhus	2020	[84]	^{87}Rb	a_{xyz}=532nm λ=1064nm	None- perform 3D imaging	LWD objective NA = 0.69	1.3	D2 Molasses λ_{im}=780nm
RIKEN	2020	[307]	^{87}Rb	Triangular a_{xy}=709nm a_z=3μm λ=1064nm	MW selection	LWD objective NA = 0.65	1.1	Raman Sideband cooling λ_{im}=780nm
Virginia	2021	[314]	^{6}Li	Triangular a_{xy}=1003nm λ=1064nm (no z lattice)	4.2μm lightsheet and accordion lattice [214]	LWD objective NA = 0.5	0.815	Ramand Sideband cooling λ_{im}=671nm
Hefei	2021	[181]	^{87}Rb	Superlattice a_{xy}=630nm,1260nm λ_{xy}=532nm,1064nm a_z=532nm λ_z=1064nm	MW selection	LWD objective NA = 0.8	1.1	D2 Molasses λ_{im}=780nm
KAIST	2021	[168]	^{7}Li	a_{xy}=752nm λ_{xy}=1064nm a_z=2μm λ_z=532nm	4.4μm Light sheet and 532nm Accordion	LWD objective NA = 0.65	1	Raman Sideband cooling λ_{im}=671nm

Group	Date	Ref	Species	Lattice	2D Gas Method	Imaging System	β	Fluorecence method
Princeton	2022	[243]	^{23}Na^{87}Rb	a_{xy}=752nm a_z=3.8μm λ=1064nm	Light sheet and large spacing vertical lattice	LWD Objective NA = 0.5	1.3	D2 Molasses for ^{87}Rb λ_{im}=780nm
LMU	2022	[140]	^{133}Cs	Superlattice a_{xy}=384nm, 767nm λ_{xy}=767nm, 1534nm a_z=8μm λ_z=1064nm	Large spacing lattice and forced evaporation	LWD Objective NA = 0.8	2	D2 Molasses λ_{im}=852nm
Chicago	2022	[286]	^{133}Cs	Triangular a_{xy} = 881 nm λ = 935 nm, rearrangement via tweezers	Light sheet	LWD Objective pair, NA=0.8	0.73	DRSC λ_{im} = 852 nm
Harvard	2023	[277]	^{168}Er	a_{xy}=266nm λ_{xy}=532nm a_z=532nm λ_z=1064nm	Accordion lattice transfer into 1064nm retro vertical lattice	In Vac. Objective NA = 0.9	≈0.5	2D Accordion expansion to 3μm spacing, image on fast 30MHz transition with no cooling.

Group	Date	Ref	Species	Lattice	2D Gas Method	Imaging System	β	Fluorecence method
Stanford	2022	[316]	^{88}Sr	a_{xy} = 575 nm a_z = 1.32 µm λ = 813 nm (Clock Magic)	Optical Tweezers	LWD objective NA=0.65	0.75	Resolved sideband cooling, while scatting on broad λ_{im} = 460 nm transition

Bibliography

[1] K. Aikawa et al. “Coherent Transfer of Photoassociated Molecules into the Rovibrational Ground State”. In: *Physical Review Letters* 105.20 (Nov. 10, 2010), p. 203001. DOI: 10.1103/PhysRevLett.105.203001 (cit. on p. 12).

[2] K. Aikawa et al. “Toward the Production of Quantum Degenerate Bosonic Polar Molecules, 41K87Rb”. In: *New Journal of Physics* 11.5 (May 2009), p. 055035. ISSN: 1367-2630. DOI: 10.1088/1367-2630/11/5/055035 (cit. on p. 15).

[3] X. Alauze et al. “An Ultracold Molecular Beam for Testing Fundamental Physics”. In: *Quantum Science and Technology* 6.4 (July 2021), p. 044005. ISSN: 2058-9565. DOI: 10.1088/2058-9565/ac107e (cit. on p. 4).

[4] Loïc Anderegg et al. “An Optical Tweezer Array of Ultracold Molecules”. In: *Science* 365.6458 (Sept. 13, 2019), pp. 1156–1158. DOI: 10.1126/science.aax1265 (cit. on pp. 12, 18).

[5] Loïc Anderegg et al. “Radio Frequency Magneto-Optical Trapping of CaF with High Density”. In: *Physical Review Letters* 119.10 (Sept. 6, 2017), p. 103201. DOI: 10.1103/PhysRevLett.119.103201 (cit. on p. 12).

[6] M. H. Anderson et al. “Observation of Bose-Einstein Condensation in a Dilute Atomic Vapor”. In: *Science* 269.5221 (July 14, 1995), pp. 198–201. DOI: 10.1126/science.269.5221.198 (cit. on p. 66).

[7] V. Andreev et al. “Improved Limit on the Electric Dipole Moment of the Electron”. In: *Nature* 562.7727 (7727 Oct. 2018), pp. 355–360. ISSN: 1476-4687. DOI: 10.1038/s41586-018-0599-8 (cit. on p. 4).

[8] Neil W. Ashcroft and N. David Mermin. *Solid State Physics*. Cengage Learning, 1976 (cit. on pp. 84, 87, 88).

[9] W. S. Bakr et al. "Probing the Superfluid-to-Mott Insulator Transition at the Single-Atom Level". In: *Science* 329.5991 (June 2010), pp. 547–550. ISSN: 00368075. DOI: 10.1126/science.1192368. pmid: 20558666 (cit. on p. 110).

[10] Waseem S. Bakr et al. "A Quantum Gas Microscope for Detecting Single Atoms in a Hubbard-regime Optical Lattice". In: *Nature* 462.7269 (Nov. 2009), pp. 74–77. ISSN: 00280836. DOI: 10.1038/nature08482. pmid: 19890326 (cit. on pp. 2, 83, 96, 110, 112, 113, 115, 145).

[11] Yicheng Bao et al. *Dipolar Spin-Exchange and Entanglement between Molecules in an Optical Tweezer Array*. Nov. 17, 2022. DOI: 10.48550/arXiv.2211.09780. arXiv: 2211.09780 [physics, physics:quant-ph]. preprint (cit. on p. 18).

[12] Yicheng Bao et al. "Fast Optical Transport of Ultracold Molecules over Long Distances". In: *New Journal of Physics* 24.9 (Sept. 2022), p. 093028. ISSN: 1367-2630. DOI: 10.1088/1367-2630/ac900f (cit. on pp. 41, 48, 53, 56).

[13] M. D. Barrett, J. A. Sauer, and M. S. Chapman. "All-Optical Formation of an Atomic Bose-Einstein Condensate". In: *Physical Review Letters* 87.1 (June 19, 2001), p. 010404. ISSN: 0031-9007, 1079-7114. DOI: 10.1103/PhysRevLett.87.010404 (cit. on p. 73).

[14] Roman Bause. "Understanding and Controlling the Collisions of Ultracold Polar Molecules". PhD thesis. Ludwig-Maximilians-Universität München, 11.2.22 (cit. on pp. 3, 11, 15).

[15] Roman Bause et al. "Collisions of Ultracold Molecules in Bright and Dark Optical Dipole Traps". In: *Physical Review Research* 3.3 (Mar. 2021). ISSN: 26431564. DOI: 10.1103/PhysRevResearch.3.033013 (cit. on p. 17).

[16] Roman Bause et al. "Tune-Out and Magic Wavelengths for Ground-State Na 23 K 40 Molecules". In: *Physical Review Letters* 125.2 (2020), pp. 1–11. ISSN: 10797114. DOI: 10.1103/PhysRevLett.125.023201. pmid: 32701321 (cit. on p. 19).

[17] Roman Bause et al. “Ultracold Sticky Collisions: Theoretical and Experimental Status”. In: *The Journal of Physical Chemistry A* 127.3 (Jan. 26, 2023), pp. 729–741. ISSN: 1089-5639. DOI: 10.1021/acs.jpca.2c08095 (cit. on pp. 5, 6, 70).

[18] John Bechhoefer. “Feedback for Physicists: A Tutorial Essay on Control”. In: *Reviews of Modern Physics* 77.3 (Aug. 31, 2005), pp. 783–836. DOI: 10.1103/RevModPhys.77.783 (cit. on p. 100).

[19] Klaas Bergmann, Nikolay V. Vitanov, and Bruce W. Shore. “Perspective: Stimulated Raman Adiabatic Passage: The Status after 25 Years”. In: *The Journal of Chemical Physics* 142.17 (May 1, 2015), p. 170901. ISSN: 0021-9606. DOI: 10.1063/1.4916903 (cit. on p. 15).

[20] Niccolò Bigagli et al. “Collisionally Stable Gas of Bosonic Dipolar Ground-State Molecules”. In: *Nature Physics* (Sept. 4, 2023), pp. 1–6. ISSN: 1745-2481. DOI: 10.1038/s41567-023-02200-6 (cit. on pp. 17, 70).

[21] Niccolò Bigagli et al. *Observation of Bose-Einstein Condensation of Dipolar Molecules*. Dec. 18, 2023. arXiv: 2312.10965. URL: http://arxiv.org/abs/2312.10965. preprint (cit. on p. 17).

[22] Ulf Bissbort. “Dynamical Effects and Disorder in Ultracold Bosonic Matter”. PhD thesis. Johann Wolfgang Goethe-Universitat in Frankfurt am Main, 2012 (cit. on p. 89).

[23] Jacob A. Blackmore et al. “Controlling the Ac Stark Effect of RbCs with Dc Electric and Magnetic Fields”. In: *Physical Review A* 102.5 (July 2020), pp. 1–15. ISSN: 24699934. DOI: 10.1103/PhysRevA.102.053316 (cit. on p. 19).

[24] Jacob Andrew Blackmore. “Coherence and Collisions in Ultracold 87 Rb 133 Cs Molecules Coherence and Collisions in Ultracold 87 Rb 133 Cs Molecules”. PhD thesis. Durham University, 2020. 215 pp. URL: http://etheses.dur.ac.uk/13730/ (cit. on pp. 3, 16, 27).

[25] S. Blatt et al. “Low-Noise Optical Lattices for Ultracold Li 6”. In: *Physical Review A - Atomic, Molecular, and Optical Physics* 92.2 (2015). ISSN: 10941622. DOI: 10.1103/PhysRevA.92.021402 (cit. on pp. 100, 113).

[26] Immanuel Bloch, Jean Dalibard, and Wilhelm Zwerger. “Many-Body Physics with Ultracold Gases”. In: *Reviews of Modern Physics* 80.3 (July 2008), pp. 885–964. ISSN: 00346861. DOI: 10.1103/RevModPhys.80.885 (cit. on p. 2).

[27] Stephen J. Blundell and Katherine M. Blundell. *Concepts in Thermal Physics*. OUP Oxford, 2010. 513 pp. ISBN: 978-0-19-956209-1. Google Books: T0luBAAAQBAJ (cit. on p. 63).

[28] D. Boiron et al. “Three-Dimensional Cooling of Cesium Atoms in Four-Beam Gray Optical Molasses”. In: *Physical Review A* 52.5 (Nov. 1, 1995), R3425–R3428. ISSN: 1050-2947, 1094-1622. DOI: 10.1103/PhysRevA.52.R3425 (cit. on p. 117).

[29] Martin Boll et al. “Spin- and Density-Resolved Microscopy of Antiferromagnetic Correlations in Fermi-Hubbard Chains”. In: *Science* 353.6305 (Sept. 2016), pp. 1257–1260. ISSN: 10959203. DOI: 10.1126/science.aag1635. pmid: 27634528 (cit. on p. 111).

[30] Fabian Böttcher et al. “Transient Supersolid Properties in an Array of Dipolar Quantum Droplets”. In: *Physical Review X* 9.1 (Mar. 22, 2019), p. 011051. DOI: 10.1103/PhysRevX.9.011051 (cit. on p. 13).

[31] T. Bourdel et al. “Experimental Study of the BEC-BCS Crossover Region in Lithium 6”. In: *Physical Review Letters* 93.5 (July 27, 2004), p. 050401. DOI: 10.1103/PhysRevLett.93.050401 (cit. on p. 2).

[32] S. Braun et al. “Negative Absolute Temperature for Motional Degrees of Freedom”. In: *Science* 339.6115 (Jan. 4, 2013), pp. 52–55. DOI: 10.1126/science.1227831 (cit. on p. 13).

[33] R. V. Brooks et al. “Preparation of One 87Rb and One 133Cs Atom in a Single Optical Tweezer”. In: *New Journal of Physics* 23.6 (June 2021), p. 065002. ISSN: 1367-2630. DOI: 10.1088/1367-2630/ac0000 (cit. on p. 18).

[34] Ralph Vincent Brooks. “Control and Collisions of 87Rb and 133Cs Atoms in Optical Tweezers”. PhD thesis. Durham University, 2022 (cit. on pp. 27, 121, 129).

[35] Antoine Browaeys and Thierry Lahaye. “Many-Body Physics with Individually Controlled Rydberg Atoms”. In: *Nature Physics* 16.2 (2 Feb. 2020), pp. 132–142. ISSN: 1745-2481. DOI: 10.1038/s41567-019-0733-z (cit. on p. 3).

[36] Peter T. Brown et al. “Spin-Imbalance in a 2D Fermi-Hubbard System”. In: *Science* 357.6358 (Sept. 29, 2017), pp. 1385–1388. DOI: 10.1126/science.aam7838 (cit. on p. 146).

[37] Nikolaus Walter Buchheim. “Dual-Species Apparatus for Creating a Dipolar Quantum Gas of 23Na40K Molecules”. PhD thesis. 2015 (cit. on p. 43).

[38] Iulia Buluta and Franco Nori. “Quantum Simulators”. In: *Science* 326.5949 (Oct. 2, 2009), pp. 108–111. DOI: 10.1126/science.1177838 (cit. on p. 7).

[39] B. Capogrosso-Sansone et al. “Quantum Phases of Cold Polar Molecules in 2D Optical Lattices”. In: *Physical Review Letters* 104.12 (Mar. 25, 2010), p. 125301. DOI: 10.1103/PhysRevLett.104.125301 (cit. on p. 11).

[40] Cheng Chen et al. “Continuous Symmetry Breaking in a Two-Dimensional Rydberg Array”. In: *Nature* 616.7958 (7958 Apr. 2023), pp. 691–695. ISSN: 1476-4687. DOI: 10.1038/s41586-023-05859-2 (cit. on p. 9).

[41] Xing-Yan Chen et al. “Field-Linked Resonances of Polar Molecules”. In: *Nature* 614.7946 (7946 Feb. 2023), pp. 59–63. ISSN: 1476-4687. DOI: 10.1038/s41586-022-05651-8 (cit. on p. 17).

[42] Xing-Yan Chen et al. *Ultracold Field-Linked Tetratomic Molecules*. June 1, 2023. arXiv: 2306.00962 [cond-mat, physics:physics, physics:quant-ph]. URL: http://arxiv.org/abs/2306.00962. preprint (cit. on p. 17).

[43] Marc Cheneau et al. “Light-Cone-like Spreading of Correlations in a Quantum Many-Body System”. In: *Nature* 481.7382 (2012), pp. 484–487. ISSN: 00280836. DOI: 10.1038/nature10748. pmid: 22281597 (cit. on p. 110).

[44] Lawrence W. Cheuk. “Quantum Gas Microscopy of Strongly Correlated Fermions”. PhD thesis. MIT, 2017 (cit. on pp. 123, 126).

[45] Lawrence W. Cheuk et al. “Observation of 2D Fermionic Mott Insulators of K 40 with Single-Site Resolution”. In: *Physical Review Letters* 116.23 (June 2016), p. 235301. ISSN: 10797114. DOI: 10.1103/PhysRevLett.116.235301. pmid: 27341242 (cit. on p. 111).

[46] Lawrence W. Cheuk et al. “Quantum-Gas Microscope for Fermionic Atoms”. In: *Physical Review Letters* 114.19 (Mar. 2015). ISSN: 10797114. DOI: 10.1103/PhysRevLett.114.193001. pmid: 26024169 (cit. on pp. 117, 118, 145).

[47] Cheng Chin et al. “Feshbach Resonances in Ultracold Gases”. In: *Reviews of Modern Physics* 82.2 (Apr. 2010), pp. 1225–1286. ISSN: 00346861. DOI: 10.1103/RevModPhys.82.1225 (cit. on p. 12).

[48] Christie S. Chiu et al. “Quantum State Engineering of a Hubbard System with Ultracold Fermions”. In: *Physical Review Letters* 120.24 (June 2018), p. 243201. ISSN: 10797114. DOI: 10.1103/PhysRevLett.120.243201. pmid: 29956952 (cit. on p. 96).

[49] Jae Yoon Choi et al. “Exploring the Many-Body Localization Transition in Two Dimensions”. In: *Science* 352.6293 (June 2016), pp. 1547–1552. ISSN: 10959203. DOI: 10.1126/science.aaf8834. pmid: 27339981 (cit. on p. 111).

[50] L. Chomaz et al. “Long-Lived and Transient Supersolid Behaviors in Dipolar Quantum Gases”. In: *Physical Review X* 9.2 (Apr. 19, 2019), p. 021012. DOI: 10.1103/PhysRevX.9.021012 (cit. on p. 13).

[51] Lauriane Chomaz et al. “Dipolar Physics: A Review of Experiments with Magnetic Quantum Gases”. In: *Reports on Progress in Physics* 86.2 (Dec. 2022), p. 026401. ISSN: 0034-4885. DOI: 10.1088/1361-6633/aca814 (cit. on p. 3).

[52] Lysander Christakis et al. “Probing Site-Resolved Correlations in a Spin System of Ultracold Molecules”. In: *Nature* 614.7946 (7946 Feb. 2023), pp. 64–69. ISSN: 1476-4687. DOI: 10.1038/s41586-022-05558-4 (cit. on pp. 9, 18, 19, 111).

[53] Steven Chu. “Nobel Lecture: The Manipulation of Neutral Particles”. In: *Reviews of Modern Physics* 70.3 (July 1, 1998), pp. 685–706. DOI: 10.1103/RevModPhys.70.685 (cit. on p. 1).

[54] Claude Cohen-Tannoudji and David Gury-Odelin. *Advances in Atomic Physics: An Overview*. World Scientific, 2011. 794 pp. ISBN: 978-981-277-496-5. Google Books: 3SVpDQAAQBAJ (cit. on pp. 23, 63, 66, 84).

[55] Claude N. Cohen-Tannoudji. "Nobel Lecture: Manipulating Atoms with Photons". In: *Reviews of Modern Physics* 70.3 (July 1, 1998), pp. 707–719. DOI: 10.1103/RevModPhys.70.707 (cit. on p. 1).

[56] Tommaso Comparin. *Tcompa/GutzwillerDynamics: GutzwillerDynamics v0.1*. Zenodo, Nov. 24, 2020. DOI: 10.5281/zenodo.4288892 (cit. on p. 96).

[57] E. A. Cornell and C. E. Wieman. "Nobel Lecture: Bose-Einstein Condensation in a Dilute Gas, the First 70 Years and Some Recent Experiments". In: *Reviews of Modern Physics* 74.3 (Aug. 19, 2002), pp. 875–893. DOI: 10.1103/RevModPhys.74.875 (cit. on p. 1).

[58] Simon L. Cornish, Michael R. Tarbutt, and Kaden R. A. Hazzard. *Quantum Computation and Quantum Simulation with Ultracold Molecules*. Jan. 10, 2024. DOI: 10.48550/arXiv.2401.05086. arXiv: 2401.05086 [cond-mat, physics:physics, physics:quant-ph]. preprint (cit. on pp. 11, 17).

[59] Simon L. Cornish et al. "Stable 85 Rb Bose-Einstein Condensates with Widely Tunable Interactions". In: *Physical Review Letters* 85.9 (2000), p. 1795 (cit. on p. 13).

[60] Dylan A Cotta. "A Single-Site Resolution Fermionic Quantum-Gas Microscope". PhD thesis. University of Strathclyde, 2018. URL: http://digitool.lib.strath.ac.uk/webclient/StreamGate?folder_id=0&dvs=1564048749330$%5Csim$86 (cit. on p. 43).

[61] Jacob P. Covey. "Enhanced Optical and Electric Manipulation of a Quantum Gas of KRb Molecules". PhD thesis. Cham: University of Colorado, 2018. DOI: 10.1007/978-3-319-98107-9 (cit. on pp. 18, 111).

[62] Jacob P. Covey et al. "An Approach to Spin-Resolved Molecular Gas Microscopy". In: *New Journal of Physics* 20.4 (2018). ISSN: 13672630. DOI: 10.1088/1367-2630/aaba65 (cit. on pp. 20, 111, 119).

[63] Maxime Ben Dahan et al. “Bloch Oscillations of Atoms in an Optical Potential”. In: *PHYSICAL REVIEW LETTERS* 76.24 (1996) (cit. on pp. 83, 103).

[64] Andrew J. Daley et al. “Practical Quantum Advantage in Quantum Simulation”. In: *Nature* 607.7920 (7920 July 2022), pp. 667–676. ISSN: 1476-4687. DOI: 10.1038/s41586-022-04940-6 (cit. on p. 7).

[65] J. Dalibard and C. Cohen-Tannoudji. “Laser Cooling below the Doppler Limit by Polarization Gradients: Simple Theoretical Models”. In: *Journal of the Optical Society of America B* 6.11 (Nov. 1989), p. 2023. ISSN: 0740-3224. DOI: 10.1364/josab.6.002023 (cit. on p. 32).

[66] J. Dalibard and C. Cohen-Tannoudji. “Laser Cooling below the Doppler Limit by Polarization Gradients: Simple Theoretical Models”. In: *JOSA B* 6.11 (Nov. 1, 1989), pp. 2023–2045. ISSN: 1520-8540. DOI: 10.1364/JOSAB.6.002023 (cit. on p. 117).

[67] Arpita Das et al. *An Association Sequence Suitable for Producing Ground-State RbCs Molecules in Optical Lattices*. Mar. 28, 2023. arXiv: 2303.16144 [cond-mat, physics:physics]. URL: http://arxiv.org/abs/2303.16144. preprint (cit. on p. 141).

[68] Asaf David and Moshe Horowitz. “Low-Frequency Transmitted Intensity Noise Induced by Stimulated Brillouin Scattering in Optical Fibers”. In: *Optics Express* 19.12 (June 2011), p. 11792. ISSN: 1094-4087. DOI: 10.1364/oe.19.011792 (cit. on p. 99).

[69] K. B. Davis, M. -O. Mewes, and W. Ketterle. “An Analytical Model for Evaporative Cooling of Atoms”. In: *Applied Physics B Laser and Optics* 60.2-3 (1995), pp. 155–159. ISSN: 0946-2171, 1432-0649. DOI: 10.1007/BF01135857 (cit. on p. 66).

[70] K. B. Davis et al. “Bose-Einstein Condensation in a Gas of Sodium Atoms”. In: *Physical Review Letters* 75.22 (Nov. 1995), pp. 3969–3973. ISSN: 00319007. DOI: 10.1103/PhysRevLett.75.3969 (cit. on p. 66).

[71] Nicolò Defenu et al. “Long-Range Interacting Quantum Systems”. In: *Reviews of Modern Physics* 95.3 (Aug. 29, 2023), p. 035002. DOI: 10.1103/RevModPhys.95.035002 (cit. on p. 3).

[72] D. DeMille. “Quantum Computation with Trapped Polar Molecules”. In: *Physical Review Letters* 88.6 (Sept. 2002), p. 4. ISSN: 10797114. DOI: 10.1103/PhysRevLett.88.067901 (cit. on p. 6).

[73] D. DeMille et al. “Enhanced Sensitivity to Variation of m_e/m_p in Molecular Spectra”. In: *Physical Review Letters* 100.4 (Jan. 29, 2008), p. 043202. DOI: 10.1103/PhysRevLett.100.043202 (cit. on p. 5).

[74] David DeMille, John M. Doyle, and Alexander O. Sushkov. “Probing the Frontiers of Particle Physics with Tabletop-Scale Experiments”. In: *Science* 357.6355 (Sept. 8, 2017), pp. 990–994. DOI: 10.1126/science.aal3003 (cit. on p. 4).

[75] M. H. G. de Miranda et al. “Controlling the Quantum Stereodynamics of Ultracold Bimolecular Reactions”. In: *Nature Physics* 7.6 (6 June 2011), pp. 502–507. ISSN: 1745-2481. DOI: 10.1038/nphys1939 (cit. on p. 17).

[76] B. J. DeSalvo et al. “Observation of a Degenerate Fermi Gas Trapped by a Bose-Einstein Condensate”. In: *Physical Review Letters* 119.23 (Dec. 7, 2017), p. 233401. DOI: 10.1103/PhysRevLett.119.233401 (cit. on p. 72).

[77] K. Dieckmann et al. “Two-Dimensional Magneto-Optical Trap as a Source of Slow Atoms”. In: *Physical Review A* 58.5 (Nov. 1, 1998), pp. 3891–3895. DOI: 10.1103/PhysRevA.58.3891 (cit. on p. 24).

[78] R. W. P. Drever et al. “Laser Phase and Frequency Stabilization Using an Optical Resonator”. In: *Applied Physics B* 31.2 (June 1, 1983), pp. 97–105. ISSN: 1432-0649. DOI: 10.1007/BF00702605 (cit. on p. 15).

[79] Marcel Duda. “Production of Ground-State 23Na40K Molecules in the Quantum-Degenerate Regime”. PhD thesis. LMU, 2022 (cit. on p. 44).

[80] Marcel Duda et al. “Transition from a Polaronic Condensate to a Degenerate Fermi Gas of Heteronuclear Molecules”. In: *Nature Physics* 19.5 (5 May 2023), pp. 720–725. ISSN: 1745-2481. DOI: 10.1038/s41567-023-01948-1 (cit. on p. 14).

[81] G. J.A. Edge et al. “Imaging and Addressing of Individual Fermionic Atoms in an Optical Lattice”. In: *Physical Review A - Atomic, Molecular, and Optical Physics* 92.6 (Dec. 2015), p. 063406. ISSN: 10941622. DOI: 10.1103/PhysRevA.92.063406 (cit. on pp. 117, 145).

[82] V. Efimov. “Energy Levels Arising from Resonant Two-Body Forces in a Three-Body System”. In: *Physics Letters B* 33.8 (Dec. 21, 1970), pp. 563–564. ISSN: 0370-2693. DOI: 10.1016/0370-2693(70)90349-7 (cit. on p. 71).

[83] Ottó Elíasson. “Magnetometry and Microscopy of Cold Atom Clouds”. PhD thesis. Aarhus University, 2019 (cit. on p. 99).

[84] Ottó Elíasson et al. “Spatial Tomography of Individual Atoms in a Quantum Gas Microscope”. In: *Physical Review A* 102.5 (Nov. 11, 2020), p. 053311. DOI: 10.1103/PhysRevA.102.053311 (cit. on pp. 134, 147).

[85] Manuel Endres et al. “Atom-by-Atom Assembly of Defect-Free One-Dimensional Cold Atom Arrays”. In: *Science* 354.6315 (Nov. 25, 2016), pp. 1024–1027. DOI: 10.1126/science.aah3752 (cit. on p. 2).

[86] Manuel Endres et al. “The ’Higgs’ Amplitude Mode at the Two-Dimensional Superfluid/Mott Insulator Transition”. In: *Nature* 487.7408 (July 2012), pp. 454–458. ISSN: 00280836. DOI: 10.1038/nature11255. pmid: 22837000 (cit. on p. 110).

[87] B. D. Esry, Chris H. Greene, and James P. Burke. “Recombination of Three Atoms in the Ultracold Limit”. In: *Physical Review Letters* 83.9 (Aug. 30, 1999), pp. 1751–1754. ISSN: 0031-9007, 1079-7114. DOI: 10.1103/PhysRevLett.83.1751 (cit. on p. 71).

[88] P. O. Fedichev, M. W. Reynolds, and G. V. Shlyapnikov. “Three-Body Recombination of Ultracold Atoms to a Weakly Bound s Level”. In: *Physical Review Letters* 77.14 (Sept. 30, 1996), pp. 2921–2924. ISSN: 0031-9007, 1079-7114. DOI: 10.1103/PhysRevLett.77.2921 (cit. on p. 71).

[89] D. Rio Fernandes et al. “Sub-Doppler Laser Cooling of Fermionic 40K Atoms in Three-Dimensional Gray Optical Molasses”. In: *Europhysics Letters* 100.6 (Dec. 2012), p. 63001. ISSN: 0295-5075. DOI: 10.1209/0295-5075/100/63001 (cit. on p. 117).

[90] Richard P. Feynman. “Simulating Physics with Computers”. In: *International Journal of Theoretical Physics* 21.6/7 (1982) (cit. on p. 7).

[91] Matthew P.A. Fisher et al. “Boson Localization and the Superfluid-Insulator Transition”. In: *Physical Review B* 40.1 (July 1989), pp. 546–570. ISSN: 01631829. DOI: 10.1103/PhysRevB.40.546 (cit. on p. 94).

[92] S. Flannigan et al. “Propagation of Errors and Quantitative Quantum Simulation with Quantum Advantage”. In: *Quantum Science and Technology* 7.4 (Aug. 2022), p. 045025. ISSN: 2058-9565. DOI: 10.1088/2058-9565/ac88f5 (cit. on p. 8).

[93] Simon Fölling et al. “Formation of Spatial Shell Structure in the Superfluid to Mott Insulator Transition”. In: *Physical Review Letters* 97.6 (Aug. 10, 2006), p. 060403. DOI: 10.1103/PhysRevLett.97.060403 (cit. on pp. 116, 128).

[94] Simon Fölling et al. “Spatial Quantum Noise Interferometry in Expanding Ultracold Atom Clouds”. In: *Nature* 434.7032 (7032 Mar. 2005), pp. 481–484. ISSN: 1476-4687. DOI: 10.1038/nature03500 (cit. on p. 83).

[95] C. J. Foot. *Atomic Physics*. Oxford University Press, 2005. 346 pp. ISBN: 978-0-19-850695-9. Google Books: _CoSDAAAQBAJ (cit. on pp. 11, 23, 37, 94, 134).

[96] W. M. C. Foulkes et al. “Quantum Monte Carlo Simulations of Solids”. In: *Reviews of Modern Physics* 73.1 (Jan. 5, 2001), pp. 33–83. DOI: 10.1103/RevModPhys.73.33 (cit. on p. 8).

[97] Takeshi Fukuhara et al. “Microscopic Observation of Magnon Bound States and Their Dynamics”. In: *Nature* 502.7469 (Sept. 2013), pp. 76–79. ISSN: 00280836. DOI: 10.1038/nature12541. pmid: 24067608 (cit. on p. 110).

[98] Bryce Gadway. “Atom-Optics Approach to Studying Transport Phenomena”. In: *Physical Review A* 92.4 (Oct. 7, 2015), p. 043606. DOI: 10.1103/PhysRevA.92.043606 (cit. on p. 102).

[99] M. W. Gempel et al. “An Adaptable Two-Lens High-Resolution Objective for Single-Site Resolved Imaging of Atoms in Optical Lattices”. In: *Review of Scientific Instruments* 90.5 (May 2019). ISSN: 10897623. DOI: 10.1063/1.5086539. pmid: 31153293 (cit. on pp. 18, 111).

[100] Justin Alan Gerber. “Cavity Quantum Electrodynamics with a Locally Addressable Quantum Gas”. PhD thesis. University of California, Berkeley, 2020 (cit. on p. 26).

[101] Fabrice Gerbier et al. “Interference Pattern and Visibility of a Mott Insulator”. In: *Physical Review A* 72.5 (Nov. 4, 2005), p. 053606. DOI: 10.1103/PhysRevA.72.053606 (cit. on pp. 104, 108).

[102] Fabrice Gerbier et al. “Phase Coherence of an Atomic Mott Insulator”. In: *Physical Review Letters* 95.5 (July 28, 2005), p. 050404. ISSN: 0031-9007, 1079-7114. DOI: 10.1103/PhysRevLett.95.050404 (cit. on pp. 106, 108).

[103] J. I. Gillen et al. “Two-Dimensional Quantum Gas in a Hybrid Surface Trap”. In: *Physical Review A - Atomic, Molecular, and Optical Physics* 80.2 (2009), pp. 1–108. ISSN: 10941622. DOI: 10.1103/PhysRevA.80.021602 (cit. on pp. 116, 145).

[104] Alexey V. Gorshkov et al. “Quantum Magnetism with Polar Alkali-Metal Dimers”. In: *Physical Review A - Atomic, Molecular, and Optical Physics* 84.3 (June 2011). ISSN: 10502947. DOI: 10.1103/PhysRevA.84.033619 (cit. on p. 10).

[105] Alexey V. Gorshkov et al. “Tunable Superfluidity and Quantum Magnetism with Ultracold Polar Molecules”. In: *Physical Review Letters* 107.11 (Sept. 2011), p. 115301. ISSN: 00319007. DOI: 10.1103/PhysRevLett.107.115301 (cit. on p. 9).

[106] Phillip L. Gould, George A. Ruff, and David E. Pritchard. “Diffraction of Atoms by Light: The near-Resonant Kapitza-Dirac Effect”. In: *Physical review letters* 56.8 (1986), p. 827 (cit. on pp. 101, 102).

[107] Philip D. Gregory et al. “Loss of Ultracold Rb 87 Cs 133 Molecules via Optical Excitation of Long-Lived Two-Body Collision Complexes”. In: *Physical Review Letters* 124.16 (Apr. 2020), p. 163402. ISSN: 10797114. DOI: 10.1103/PhysRevLett.124.163402. pmid: 32383932 (cit. on pp. 5, 17, 70).

[108] Philip D. Gregory et al. “Robust Storage Qubits in Ultracold Polar Molecules”. In: *Nature Physics* 17.10 (10 Oct. 2021), pp. 1149–1153. ISSN: 1745-2481. DOI: 10.1038/s41567-021-01328-7 (cit. on p. 19).

[109] Philip D. Gregory et al. *Second-Scale Rotational Coherence and Dipolar Interactions in a Gas of Ultracold Polar Molecules*. Aug. 11, 2023. DOI: 10.48550/arXiv.2306.02991. arXiv: 2306.02991 [cond-mat, physics:physics]. preprint (cit. on p. 19).

[110] Philip David Gregory. “Coherent Control of Ultracold Polar Molecules”. PhD thesis. University of Durham, Mar. 2017 (cit. on pp. 15, 27).

[111] Daniel Greif et al. “Site-Resolved Imaging of a Fermionic Mott Insulator”. In: *Science* 351.6276 (Nov. 2016), pp. 953–957. ISSN: 10959203. DOI: 10.1126/science.aad9041. pmid: 26917766 (cit. on p. 111).

[112] Markus Greiner. “Ultracold quantum gases in three-dimensional optical lattice potentials”. PhD thesis. Ludwig-Maximilians-Universität München, Apr. 29, 2003. URL: https://edoc.ub.uni-muenchen.de/968/ (cit. on pp. 83, 84, 89, 91, 103).

[113] Markus Greiner et al. “Magnetic Transport of Trapped Cold Atoms over a Large Distance”. In: *Physical Review A* 63.3 (Feb. 9, 2001), p. 031401. DOI: 10.1103/PhysRevA.63.031401 (cit. on pp. 41, 42).

[114] Markus Greiner et al. “Quantum Phase Transition from a Superfluid to a Mott Insulator in a Gas of Ultracold Atoms”. In: *Nature* 415.6867 (6867 Jan. 2002), pp. 39–44. ISSN: 1476-4687. DOI: 10.1038/415039a (cit. on pp. 2, 104, 109).

[115] Rudolf Grimm, Matthias Weidemüller, and Yurii B. Ovchinnikov. “Optical Dipole Traps for Neutral Atoms”. In: *Advances in Atomic, Molecular and Optical Physics* 42.C (Feb. 2000), pp. 95–170. ISSN: 1049250X. DOI: 10.1016/S1049-250X(08)60186-X (cit. on pp. 23, 39, 46, 70, 75, 97).

[116] Michael Gröbner et al. “Observation of Interspecies Feshbach Resonances in an Ultracold ^{39}K –^{133} Cs Mixture and Refinement of Interaction Potentials”. In: *Physical Review A* 95.2 (Feb. 28, 2017), p. 022715. DOI: 10.1103/PhysRevA.95.022715 (cit. on p. 72).

[117] Michael Gröbner et al. “Observation of Interspecies Feshbach Resonances in an Ultracold K 39 - Cs 133 Mixture and Refinement of Interaction Potentials”. In: *Physical Review A* 95.2 (Feb. 2017), pp. 46–48. ISSN: 24699934. DOI: 10.1103/PhysRevA.95.022715 (cit. on p. 24).

[118] Christian Gross and Waseem S. Bakr. “Quantum Gas Microscopy for Single Atom and Spin Detection”. In: *Nature Physics* 17.12 (Nov. 2021), pp. 1316–1323. ISSN: 17452481. DOI: 10.1038/s41567-021-01370-5 (cit. on pp. 2, 83, 110).

[119] Christian Gross and Immanuel Bloch. “Quantum Simulations with Ultracold Atoms in Optical Lattices”. In: *Science* 357.6355 (Sept. 2017), pp. 995–1001. ISSN: 10959203. DOI: 10.1126/science.aal3837. pmid: 28883070 (cit. on p. 83).

[120] G. Grynberg et al. “Quantized Motion of Cold Cesium Atoms in Two- and Three-Dimensional Optical Potentials”. In: *Physical Review Letters* 70.15 (Apr. 12, 1993), pp. 2249–2252. DOI: 10.1103/PhysRevLett.70.2249 (cit. on p. 34).

[121] Q. Guan, Simon L. Cornish, and S. Kotochigova. “Magic Conditions for Multiple Rotational States of Bialkali Molecules in Optical Lattices”. In: *Physical Re-*

view A 103.4 (Apr. 7, 2021), p. 043311. DOI: 10.1103/PhysRevA.103.043311 (cit. on p. 20).

[122] Mingyang Guo et al. "Creation of an Ultracold Gas of Ground-State Dipolar $^{23}Na^{87}Rb$ Molecules". In: *Physical Review Letters* 116.20 (May 19, 2016), p. 205303. DOI: 10.1103/PhysRevLett.116.205303 (cit. on p. 12).

[123] T. L. Gustavson et al. "Transport of Bose-Einstein Condensates with Optical Tweezers". In: *Physical Review Letters* 88.2 (Dec. 21, 2001), p. 020401. DOI: 10.1103/PhysRevLett.88.020401 (cit. on pp. 41, 43).

[124] Alexander Guttridge. "Photoassociation of Ultracold CsYb Molecules and Determination of Interspecies Scattering Lengths Photoassociation of Ultracold CsYb Molecules and Determination of Interspecies Scattering Lengths". PhD thesis. University of Durham, 2018 (cit. on pp. 23, 34, 39).

[125] Alexander Guttridge et al. "Observation of Rydberg Blockade Due to the Charge-Dipole Interaction between an Atom and a Polar Molecule". In: *Physical Review Letters* 131.1 (July 7, 2023), p. 013401. DOI: 10.1103/PhysRevLett.131.013401 (cit. on pp. 18, 19, 141).

[126] Z. Hadzibabic et al. "Two-Species Mixture of Quantum Degenerate Bose and Fermi Gases". In: *Physical Review Letters* 88.16 (Apr. 4, 2002), p. 160401. DOI: 10.1103/PhysRevLett.88.160401 (cit. on p. 71).

[127] Elmar Haller et al. "Single-Atom Imaging of Fermions in a Quantum-Gas Microscope". In: *Nature Physics* 11.9 (Sept. 2015), pp. 738–742. ISSN: 17452481. DOI: 10.1038/nphys3403 (cit. on pp. 117, 145).

[128] M. L. Harris, P. Tierney, and S. L. Cornish. "Magnetic Trapping of a Cold Rb–Cs Atomic Mixture". In: *Journal of Physics B: Atomic, Molecular and Optical Physics* 41.3 (Jan. 2008), p. 035303. ISSN: 0953-4075. DOI: 10.1088/0953-4075/41/3/035303 (cit. on p. 32).

[129] Thomas Hartke et al. "Doublon-Hole Correlations and Fluctuation Thermometry in a Fermi-Hubbard Gas". In: *Physical Review Letters* 125.11 (Sept. 9, 2020), p. 113601. DOI: 10.1103/PhysRevLett.125.113601 (cit. on p. 118).

[130] Junyu He et al. “Characterization of the Lowest Electronically Excited-State Ro-Vibrational Level of 23Na87Rb”. In: *New Journal of Physics* 23.11 (Oct. 2021), p. 115003. ISSN: 1367-2630. DOI: 10.1088/1367-2630/ac2dad (cit. on p. 19).

[131] Harald F. Hess. “Evaporative Cooling of Magnetically Trapped and Compressed Spin-Polarized Hydrogen”. In: *Physical Review B* 34.5 (Sept. 1, 1986), pp. 3476–3479. ISSN: 0163-1829. DOI: 10.1103/PhysRevB.34.3476 (cit. on p. 66).

[132] G. T. Hickman and M. Saffman. “Speed, Retention Loss, and Motional Heating of Atoms in an Optical Conveyor Belt”. In: *Physical Review A* 101.6 (2020). ISSN: 24699934. DOI: 10.1103/PhysRevA.101.063411 (cit. on pp. 52, 56, 58).

[133] Timon Hilker. “Spin-Resolved Microscopy of Strongly Correlated Fermionic Many-Body States”. PhD thesis. Ludwig–Maximilians–Universität München, 2017. 1013–1013 (cit. on p. 126).

[134] Sarah Hirthe. “Quantum Gas Microscopy of Fermi-Hubbard Ladders”. PhD thesis. Ludwig-Maximilians-Universität München, 2022 (cit. on p. 121).

[135] Connor M. Holland, Yukai Lu, and Lawrence W. Cheuk. *On-Demand Entanglement of Molecules in a Reconfigurable Optical Tweezer Array*. Oct. 12, 2022. DOI: 10.48550/arXiv.2210.06309. arXiv: 2210.06309 [cond-mat, physics:physics, physics:quant-ph]. preprint (cit. on pp. 9, 18).

[136] J. J. Hudson et al. “Improved Measurement of the Shape of the Electron”. In: *Nature* 473.7348 (7348 May 2011), pp. 493–496. ISSN: 1476-4687. DOI: 10.1038/nature10104 (cit. on p. 4).

[137] Michael Hughes et al. “Robust Entangling Gate for Polar Molecules Using Magnetic and Microwave Fields”. In: *Physical Review A* 101.6 (June 3, 2020), p. 062308. DOI: 10.1103/PhysRevA.101.062308 (cit. on p. 6).

[138] Chen-Lung Hung et al. “Accelerating Evaporative Cooling of Atoms into Bose-Einstein Condensation in Optical Traps”. In: *Physical Review A* 78.1 (July 24, 2008), p. 011604. DOI: 10.1103/PhysRevA.78.011604 (cit. on pp. 69, 77).

[139] B. Hunt. “A Matrix Theory Proof of the Discrete Convolution Theorem”. In: *IEEE Transactions on Audio and Electroacoustics* 19.4 (1971), pp. 285–288 (cit. on p. 126).

[140] Alexander Impertro et al. “An Unsupervised Deep Learning Algorithm for Single-Site Reconstruction in Quantum Gas Microscopes”. In: *Communications Physics* 6.1 (1 July 7, 2023), pp. 1–8. ISSN: 2399-3650. DOI: 10.1038/s42005-023-01287-w (cit. on pp. 82, 96, 114, 126, 127, 142, 148).

[141] Rajibul Islam et al. “Measuring Entanglement Entropy in a Quantum Many-Body System”. In: *Nature* 528.7580 (Dec. 2015), pp. 77–83. ISSN: 14764687. DOI: 10.1038/nature15750 (cit. on p. 111).

[142] D. Jaksch and P. Zoller. “Creation of Effective Magnetic Fields in Optical Lattices: The Hofstadter Butterfly for Cold Neutral Atoms”. In: *New Journal of Physics* 5.1 (May 2003), p. 56. ISSN: 1367-2630. DOI: 10.1088/1367-2630/5/1/356 (cit. on p. 82).

[143] D. Jaksch et al. “Cold Bosonic Atoms in Optical Lattices”. In: *Physical Review Letters* 81.15 (1998), pp. 3108–3111. ISSN: 10797114. DOI: 10.1103/PhysRevLett.81.3108 (cit. on pp. 89, 94).

[144] D. Jaksch et al. “Creation of a Molecular Condensate by Dynamically Melting a Mott Insulator”. In: *Physical Review Letters* 89.4 (2002), pp. 2–5. ISSN: 10797114. DOI: 10.1103/PhysRevLett.89.040402 (cit. on p. 14).

[145] Daniel L Jenkin. “Feshbach Spectroscopy of an Ultracold Rb-Cs Mixture”. In: () (cit. on p. 40).

[146] Kevin M. Jones et al. “Ultracold Photoassociation Spectroscopy: Long-range Molecules and Atomic Scattering”. In: *Reviews of Modern Physics* 78.2 (May 22, 2006), pp. 483–535. DOI: 10.1103/RevModPhys.78.483 (cit. on p. 70).

[147] P. L. Kapitza and P. A. M. Dirac. “The Reflection of Electrons from Standing Light Waves”. In: *Mathematical Proceedings of the Cambridge Philosophical Society* 29.2 (1933), pp. 297–300 (cit. on p. 101).

[148] A. M. Kaufman et al. “Two-Particle Quantum Interference in Tunnel-Coupled Optical Tweezers”. In: *Science* 345.6194 (July 18, 2014), pp. 306–309. DOI: 10.1126/science.1250057 (cit. on p. 2).

[149] Adam M. Kaufman et al. “Quantum Thermalization through Entanglement in an Isolated Many-Body System”. In: *Science* 353.6301 (Aug. 2016), pp. 794–800. ISSN: 10959203. DOI: 10.1126/science.aaf6725 (cit. on p. 111).

[150] Andrew J. Kerman et al. “Beyond Optical Molasses: 3D Raman Sideband Cooling of Atomic Cesium to High Phase-Space Density”. In: *Physical Review Letters* 84.3 (Jan. 17, 2000), pp. 439–442. DOI: 10.1103/PhysRevLett.84.439 (cit. on pp. 24, 34).

[151] Andrew J. Kerman et al. “Determination of Cs–Cs Interaction Parameters Using Feshbach Spectroscopy”. In: *Comptes Rendus de l’Académie des Sciences - Series IV - Physics* 2.4 (June 2001), pp. 633–639. ISSN: 12962147. DOI: 10.1016/S1296-2147(01)01196-9 (cit. on p. 70).

[152] Kerman, Andrew James. “Raman Sideband Cooling and Cold Atomic Collisions in Optical Lattices”. PhD thesis. Stanford University, 2002 (cit. on pp. 32–34, 36, 141).

[153] W. Ketterle, D. S. Durfee, and D. M. Stamper-Kurn. “Making, Probing and Understanding Bose-Einstein Condensates”. In: (1999). ISSN: 0074-784X. URL: http://arxiv.org/abs/cond-mat/9904034 (cit. on pp. 37, 38, 80).

[154] Wolfgang Ketterle. “Nobel Lecture: When Atoms Behave as Waves: Bose-Einstein Condensation and the Atom Laser”. In: *Reviews of Modern Physics* 74.4 (Nov. 20, 2002), pp. 1131–1151. DOI: 10.1103/RevModPhys.74.1131 (cit. on p. 1).

[155] Wolfgang Ketterle et al. “High Densities of Cold Atoms in a Dark Spontaneous-Force Optical Trap”. In: *Physical Review Letters* 70.15 (Apr. 12, 1993), pp. 2253–2256. DOI: 10.1103/PhysRevLett.70.2253 (cit. on pp. 32, 141).

[156] L. Khaykovich et al. “Formation of a Matter-Wave Bright Soliton”. In: *Science* 296.5571 (May 17, 2002), pp. 1290–1293. DOI: 10.1126/science.1071021 (cit. on p. 13).

[157] M. Khudaverdyan et al. “Adiabatic Quantum State Manipulation of Single Trapped Atoms”. In: *Physical Review A* 71.3 (Mar. 23, 2005), p. 031404. DOI: 10.1103/PhysRevA.71.031404 (cit. on p. 129).

[158] Till Klostermann et al. “Fast Long-Distance Transport of Cold Cesium Atoms”. In: (Sept. 2021). URL: http://arxiv.org/abs/2109.03804 (cit. on p. 50).

[159] Till Klostermann et al. “Fast Long-Distance Transport of Cold Cesium Atoms”. In: *Physical Review A* 105.4 (Apr. 26, 2022), p. 043319. DOI: 10.1103/PhysRevA.105.043319 (cit. on pp. 41, 48, 56, 82).

[160] Till Mitja Klostermann. “Construction of a Caesium Quantum Gas Microscope”. PhD thesis. Ludwig-Maximilians-Universität München, Dec. 4, 2021 (cit. on pp. 53, 142).

[161] J. Kobayashi, A. Ogino, and S. Inouye. “Measurement of the Variation of Electron-to-Proton Mass Ratio Using Ultracold Molecules Produced from Laser-Cooled Atoms”. In: *Nature Communications* 10.1 (1 Aug. 21, 2019), p. 3771. ISSN: 2041-1723. DOI: 10.1038/s41467-019-11761-1 (cit. on p. 5).

[162] Joannis Koepsell et al. “Robust Bilayer Charge Pumping for Spin- And Density-Resolved Quantum Gas Microscopy”. In: *Physical Review Letters* 125.1 (July 2020), pp. 97–100. ISSN: 10797114. DOI: 10.1103/PhysRevLett.125.010403. pmid: 32678648 (cit. on pp. 113, 118).

[163] Thorsten Köhler, Krzysztof Góral, and Paul S. Julienne. “Production of Cold Molecules via Magnetically Tunable Feshbach Resonances”. In: *Reviews of Modern Physics* 78.4 (Dec. 1, 2006), pp. 1311–1361. DOI: 10.1103/RevModPhys.78.1311 (cit. on p. 13).

[164] T. Kraemer et al. “Evidence for Efimov Quantum States in an Ultracold Gas of Caesium Atoms”. In: *Nature* 440.7082 (7082 Mar. 2006), pp. 315–318. ISSN: 1476-4687. DOI: 10.1038/nature04626 (cit. on pp. 71, 79, 80).

[165] T. Kraemer et al. “Optimized Production of a Cesium Bose–Einstein Condensate”. In: *Applied Physics B* 79.8 (Dec. 1, 2004), pp. 1013–1019. ISSN: 1432-0649. DOI: 10.1007/s00340-004-1657-5 (cit. on p. 39).

[166] Tobias Kraemer. “Few-body interactions in an ultracold gas of Cesium atoms”. Leopold-Franzens-Universität Innsbruck, 2006 (cit. on p. 71).

[167] G. Kucsko et al. “Critical Thermalization of a Disordered Dipolar Spin System in Diamond”. In: *Physical Review Letters* 121.2 (July 9, 2018), p. 023601. DOI: 10.1103/PhysRevLett.121.023601 (cit. on p. 8).

[168] Kiryang Kwon et al. “Site-Resolved Imaging of a Bosonic Mott Insulator of ^{7}Li Atoms”. In: *Physical Review A* 105.3 (Mar. 31, 2022), p. 033323. DOI: 10.1103/PhysRevA.105.033323 (cit. on p. 147).

[169] Arthur La Rooij et al. “A Comparative Study of Deconvolution Techniques for Quantum-Gas Microscope Images”. In: *New Journal of Physics* (2023). ISSN: 1367-2630. DOI: 10.1088/1367-2630/aced65 (cit. on pp. 114, 123, 126).

[170] Lev Davidovich Landau and Evgenii Mikhailovich Lifshitz. *Statistical Physics: Volume 5*. Vol. 5. Elsevier, 2013. URL: https://books.google.co.uk/books?hl=en&lr=&id=VzgJN-XPTRsC&oi=fnd&pg=PP1&dq=Landau+Lifshitz+Statistical+Physics&ots=8dkQjPjJgB&sig=ZN8D8P-ZV84QwvBeua9J2bXLWY0 (cit. on p. 65).

[171] Tim Langen et al. *Quantum State Manipulation and Science of Ultracold Molecules*. May 22, 2023. arXiv: 2305.13445 [cond-mat, physics:physics, physics:quant-ph]. URL: http://arxiv.org/abs/2305.13445. preprint (cit. on pp. 3, 17).

[172] Julian Léonard et al. “Optical Transport and Manipulation of an Ultracold Atomic Cloud Using Focus-Tunable Lenses”. In: *New Journal of Physics* 16.9 (Sept. 2014), p. 093028. ISSN: 13672630. DOI: 10.1088/1367-2630/16/9/093028 (cit. on p. 43).

[173] A. D. Lercher et al. “Production of a Dual-Species Bose-Einstein Condensate of Rb and Cs Atoms”. In: *European Physical Journal D* 65.1-2 (2011), pp. 3–9. ISSN: 14346060. DOI: 10.1140/epjd/e2011-20015-6 (cit. on pp. 15, 39, 60, 72, 73, 79, 82, 139, 141).

[174] H. J. Lewandowski et al. “Simplified System for Creating a Bose–Einstein Condensate”. In: *Journal of Low Temperature Physics* 132.5 (Sept. 1, 2003), pp. 309–367. ISSN: 1573-7357. DOI: 10.1023/A:1024800600621 (cit. on pp. 41, 42).

[175] Maciej Lewenstein, Anna Sanpera, and Verònica Ahufinger. *Ultracold Atoms in Optical Lattices: Simulating Quantum Many-Body Systems*. Oxford University Press, Mar. 8, 2012. ISBN: 978-0-19-957312-7. DOI: 10.1093/acprof:oso/9780199573127.001.0001 (cit. on pp. 7, 84).

[176] Jun Li et al. “Advances and New Challenges to Bimolecular Reaction Dynamics Theory”. In: *The Journal of Physical Chemistry Letters* 11.20 (Oct. 15, 2020), pp. 8844–8860. DOI: 10.1021/acs.jpclett.0c02501 (cit. on p. 5).

[177] Jun-Ru Li et al. “Tunable Itinerant Spin Dynamics with Polar Molecules”. In: *Nature* 614.7946 (7946 Feb. 2023), pp. 70–74. ISSN: 1476-4687. DOI: 10.1038/s41586-022-05479-2 (cit. on pp. 18, 19).

[178] Jun-Ru Li et al. “Tuning of Dipolar Interactions and Evaporative Cooling in a Three-Dimensional Molecular Quantum Gas”. In: *Nature Physics* 17.10 (Oct. 2021), pp. 1144–1148. ISSN: 1745-2473, 1745-2481. DOI: 10.1038/s41567-021-01329-6 (cit. on p. 143).

[179] Lintao Li et al. “Active Cancellation of Servo-Induced Noise on Stabilized Lasers via Feedforward”. In: *Physical Review Applied* 18.6 (Dec. 2, 2022), p. 064005. DOI: 10.1103/PhysRevApplied.18.064005 (cit. on pp. 16, 141).

[180] Meng-Da Li et al. “High-Powered Optical Superlattice with Robust Phase Stability for Quantum Gas Microscopy”. In: *Optics Express* 29.9 (Apr. 26, 2021), pp. 13876–13886. ISSN: 1094-4087. DOI: 10.1364/OE.423776 (cit. on p. 113).

[181] Meng-Da Li et al. “High-Powered Optical Superlattice with Robust Phase Stability for Quantum Gas Microscopy”. In: *Optics Express* 29.9 (Apr. 2021), p. 13876. ISSN: 1094-4087. DOI: 10.1364/oe.423776. pmid: 33985115 (cit. on p. 147).

[182] Vincent Lienhard et al. “Realization of a Density-Dependent Peierls Phase in a Synthetic, Spin-Orbit Coupled Rydberg System”. In: *Physical Review X* 10.2 (May 2020), pp. 1–11. ISSN: 21603308. DOI: 10.1103/PhysRevX.10.021031 (cit. on p. 10).

[183] Junyu Lin et al. *Microwave Shielding of Bosonic NaRb Molecules*. Apr. 17, 2023. arXiv: 2304.08312 [cond-mat, physics:physics, physics:quant-ph]. URL: http://arxiv.org/abs/2304.08312. preprint (cit. on pp. 17, 70).

[184] Junyu Lin et al. “Seconds-Scale Coherence on Nuclear Spin Transitions of Ultracold Polar Molecules in 3D Optical Lattices”. In: *Physical Review Letters* 128.22 (June 1, 2022), p. 223201. DOI: 10.1103/PhysRevLett.128.223201 (cit. on p. 19).

[185] L. R. Liu et al. “Molecular Assembly of Ground-State Cooled Single Atoms”. In: *Physical Review X* 9.2 (May 24, 2019), p. 021039. ISSN: 2160-3308. DOI: 10.1103/PhysRevX.9.021039 (cit. on pp. 52, 56).

[186] Yu Liu et al. “Photo-Excitation of Long-Lived Transient Intermediates in Ultracold Reactions”. In: *Nature Physics* 16.11 (11 Nov. 2020), pp. 1132–1136. ISSN: 1745-2481. DOI: 10.1038/s41567-020-0968-8 (cit. on pp. 5, 17).

[187] Yu Liu et al. “Precision Test of Statistical Dynamics with State-to-State Ultracold Chemistry”. In: *Nature* 593.7859 (7859 May 2021), pp. 379–384. ISSN: 1476-4687. DOI: 10.1038/s41586-021-03459-6 (cit. on p. 6).

[188] Xiao Jing Lu et al. “Noise Sensitivities for an Atom Shuttled by a Moving Optical Lattice via Shortcuts to Adiabaticity”. In: *Entropy* 22.3 (2020), pp. 1–16. ISSN: 10994300. DOI: 10.3390/e22030262 (cit. on p. 50).

[189] Yukai Lu et al. *Raman Sideband Cooling of Molecules in an Optical Tweezer Array*. June 4, 2023. arXiv: 2306.02455 [cond-mat, physics:physics]. URL: http://arxiv.org/abs/2306.02455. preprint (cit. on p. 18).

[190] O. J. Luiten, M. W. Reynolds, and J. T. M. Walraven. "Kinetic Theory of the Evaporative Cooling of a Trapped Gas". In: *Physical Review A* 53.1 (Jan. 1, 1996), pp. 381–389. ISSN: 1050-2947, 1094-1622. DOI: 10.1103/PhysRevA.53.381 (cit. on pp. 67, 68).

[191] S.H. Madkhaly et al. "Performance-Optimized Components for Quantum Technologies via Additive Manufacturing". In: *PRX Quantum* 2.3 (Aug. 12, 2021), p. 030326. DOI: 10.1103/PRXQuantum.2.030326 (cit. on p. 37).

[192] S. M. Mansfield and G. S. Kino. "Solid Immersion Microscope". In: *Applied Physics Letters* 57.24 (Dec. 10, 1990), pp. 2615–2616. ISSN: 0003-6951. DOI: 10.1063/1.103828 (cit. on p. 115).

[193] M. J. Mark et al. "Precision Measurements on a Tunable Mott Insulator of Ultracold Atoms". In: *Physical Review Letters* 107.17 (Oct. 18, 2011), p. 175301. DOI: 10.1103/PhysRevLett.107.175301 (cit. on p. 109).

[194] Kyle Matsuda et al. "Resonant Collisional Shielding of Reactive Molecules Using Electric Fields". In: *Science* 370.6522 (Sept. 2020), pp. 1324–1327. ISSN: 10959203. DOI: 10.1126/science.abe7370. pmid: 33303614 (cit. on p. 17).

[195] Alex J. Matthies. "Optical Conveyor-Belt Transport for Cs and Rb Atoms". PhD thesis. Durham University, 2023 (cit. on pp. 21, 48, 55, 56).

[196] Alex J. Matthies et al. *Long Distance Optical Conveyor-Belt Transport of Ultracold ^{133}Cs and ^{87}Rb Atoms*. July 25, 2023. DOI: 10.48550/arXiv.2307.13382. arXiv: 2307.13382 [cond-mat, physics:physics]. preprint (cit. on pp. 21, 22).

[197] D. J. McCarron et al. "Dual-Species Bose-Einstein Condensate of Rb 87 and Cs 133". In: *Physical Review A* 84.1 (2011), p. 011603 (cit. on pp. 15, 23, 60, 72, 139).

[198] Daniel J McCarron. "A Quantum Degenerate Mixture of 87Rb and 133Cs". Durham University, 2011 (cit. on pp. 23, 72).

[199] Eric J. Meier et al. “Observation of the Topological Anderson Insulator in Disordered Atomic Wires”. In: *Science* 362.6417 (Nov. 23, 2018), pp. 929–933. DOI: 10.1126/science.aat3406 (cit. on p. 102).

[200] Max Melchner. “Quantum Simulation with an Optical Kagome Lattice”. University of Cambridge. URL: https://www.repository.cam.ac.uk/handle/1810/339053 (cit. on pp. 43, 91).

[201] Carlos R. Menegatti et al. “Trap Loss in a Rubidium Crossed Dipole Trap by Short-Range Photoassociation”. In: *Physical Review A* 87.5 (May 8, 2013), p. 053404. DOI: 10.1103/PhysRevA.87.053404 (cit. on p. 70).

[202] A. Micheli, G. K. Brennen, and P. Zoller. “A Toolbox for Lattice-Spin Models with Polar Molecules”. In: *Nature Physics* 2.5 (May 2006), pp. 341–347. ISSN: 17452481. DOI: 10.1038/nphys287 (cit. on p. 10).

[203] Thomas Middelmann et al. “Long-Range Transport of Ultracold Atoms in a Far-Detuned One-Dimensional Optical Lattice”. In: *New Journal of Physics* 14 (July 2012), pp. 0–13. ISSN: 13672630. DOI: 10.1088/1367-2630/14/7/073020 (cit. on p. 41).

[204] Frederick H. Mies et al. “Estimating Bounds on Collisional Relaxation Rates of Spin-Polarized 87Rb Atoms at Ultracold Temperatures”. In: *Journal of Research of the National Institute of Standards and Technology* 101.4 (1996), pp. 521–535. ISSN: 1044-677X. DOI: 10.6028/jres.101.052. pmid: 27805105 (cit. on p. 70).

[205] J. D. Miller, R. A. Cline, and D. J. Heinzen. “Photoassociation Spectrum of Ultracold Rb Atoms”. In: *Physical Review Letters* 71.14 (Oct. 4, 1993), pp. 2204–2207. DOI: 10.1103/PhysRevLett.71.2204 (cit. on p. 70).

[206] Martin Miranda et al. “Site-Resolved Imaging of a Bosonic Mott Insulator Using Ytterbium Atoms”. In: *Physical Review A* 96.4 (Oct. 2017), p. 043626. ISSN: 24699934. DOI: 10.1103/PhysRevA.96.043626 (cit. on p. 118).

[207] Martin Miranda et al. “Site-Resolved Imaging of Ytterbium Atoms in a Two-Dimensional Optical Lattice”. In: *Physical Review A* 91.6 (June 19, 2015), p. 063414. DOI: 10.1103/PhysRevA.91.063414 (cit. on pp. 113, 146).

[208] S. I. Mistakidis et al. *Cold Atoms in Low Dimensions – a Laboratory for Quantum Dynamics*. Feb. 22, 2022. DOI: 10.48550/arXiv.2202.11071. arXiv: 2202.11071 [cond-mat, physics:physics, physics:quant-ph]. preprint (cit. on p. 116).

[209] Debayan Mitra et al. "Phase Separation and Pair Condensation in a Spin-Imbalanced 2D Fermi Gas". In: *Physical Review Letters* 117.9 (Aug. 24, 2016), p. 093601. DOI: 10.1103/PhysRevLett.117.093601 (cit. on p. 116).

[210] G. Modugno et al. "Bose-Einstein Condensation of Potassium Atoms by Sympathetic Cooling". In: *Science* 294.5545 (Nov. 2001), pp. 1320–1322. ISSN: 00368075. DOI: 10.1126/science.1066687. pmid: 11641466 (cit. on p. 71).

[211] Peter K. Molony. "Creation of Ultracold Polar Ground-State RbCs Molecules". Durham University, 2016, p. 9322282. URL: http://etheses.dur.ac.uk/11781/ (cit. on p. 23).

[212] Peter K. Molony et al. "Creation of Ultracold Rb 87 Cs 133 Molecules in the Rovibrational Ground State". In: *Physical Review Letters* 113.25 (Dec. 2014), p. 255301. ISSN: 10797114. DOI: 10.1103/PhysRevLett.113.255301 (cit. on pp. 12, 15, 141).

[213] Peter K. Molony et al. "Production of Ultracold 87Rb133Cs in the Absolute Ground State: Complete Characterisation of the Stimulated Raman Adiabatic Passage Transfer". In: *ChemPhysChem* 17.22 (2016), pp. 3811–3817. ISSN: 1439-7641. DOI: 10.1002/cphc.201600501 (cit. on p. 16).

[214] Jirayu Mongkolkiattichai et al. *Quantum Gas Microscopy of a Geometrically Frustrated Hubbard System*. Oct. 26, 2022. DOI: 10.48550/arXiv.2210.14895. arXiv: 2210.14895 [cond-mat, physics:physics]. preprint (cit. on p. 147).

[215] F. L. Moore et al. "Atom Optics Realization of the Quantum δ-Kicked Rotor". In: *Physical Review Letters* 75.25 (Dec. 18, 1995), pp. 4598–4601. DOI: 10.1103/PhysRevLett.75.4598 (cit. on p. 102).

[216] Steven A. Moses et al. “Creation of a Low-Entropy Quantum Gas of Polar Molecules in an Optical Lattice”. In: *Science* 350.6261 (Nov. 2015), pp. 659–662. ISSN: 10959203. DOI: 10.1126/science.aac6400. pmid: 26542566 (cit. on p. 14).

[217] Bijit Mukherjee and Jeremy M. Hutson. *Controlling Collisional Loss and Scattering Lengths of Ultracold Dipolar Molecules with Static Electric Fields*. Nov. 14, 2023. arXiv: 2311.08301 [cond-mat, physics:quant-ph]. URL: http://arxiv.org/abs/2311.08301. preprint (cit. on pp. 142, 143).

[218] Karl D. Nelson, Xiao Li, and David S. Weiss. “Imaging Single Atoms in a Three-Dimensional Array”. In: *Nature Physics* 3.8 (8 Aug. 2007), pp. 556–560. ISSN: 1745-2481. DOI: 10.1038/nphys645 (cit. on p. 110).

[219] B. Neyenhuis et al. “Anisotropic Polarizability of Ultracold Polar K40Rb87 Molecules”. In: *Physical Review Letters* 109.23 (Dec. 2012), p. 230403. ISSN: 00319007. DOI: 10.1103/PhysRevLett.109.230403 (cit. on p. 19).

[220] K. K. Ni et al. “A High Phase-Space-Density Gas of Polar Molecules”. In: *Science* 322.5899 (Oct. 2008), pp. 231–235. ISSN: 00368075. DOI: 10.1126/science.1163861 (cit. on p. 12).

[221] Kang Kuen Ni, Till Rosenband, and David D. Grimes. “Dipolar Exchange Quantum Logic Gate with Polar Molecules”. In: *Chemical Science* 9.33 (Aug. 2018), pp. 6830–6838. ISSN: 20416539. DOI: 10.1039/c8sc02355g (cit. on p. 6).

[222] Ahmed Omran. “A Microscope for Fermi Gases”. PhD thesis. Ludwig–Maximilians–Universität München, 2016 (cit. on p. 118).

[223] Ahmed Omran et al. “Microscopic Observation of Pauli Blocking in Degenerate Fermionic Lattice Gases”. In: *Physical Review Letters* 115.26 (Oct. 2015), pp. 1–8. ISSN: 10797114. DOI: 10.1103/PhysRevLett.115.263001. pmid: 26764988 (cit. on pp. 112, 118, 146).

[224] François Orieux, Jean-François Giovannelli, and Thomas Rodet. “Bayesian Estimation of Regularization and Point Spread Function Parameters for Wiener–Hunt Deconvolution”. In: *JOSA A* 27.7 (July 1, 2010), pp. 1593–1607. ISSN: 1520-8532. DOI: 10.1364/JOSAA.27.001593 (cit. on p. 126).

[225] S. Ospelkaus et al. “Quantum-State Controlled Chemical Reactions of Ultracold Potassium-Rubidium Molecules”. In: *Science (New York, N.Y.)* 327.5967 (Feb. 12, 2010), pp. 853–857. ISSN: 1095-9203. DOI: 10.1126/science.1184121. pmid: 20150499 (cit. on p. 6).

[226] Scott B Papp. “Experiments with a Two-Species Bose-Einstein Condensate Utilizing Widely Tunable Interparticle Interactions”. PhD thesis. University of Colorado, 2001 (cit. on p. 29).

[227] Jee Woo Park, Sebastian A. Will, and Martin W. Zwierlein. “Ultracold Dipolar Gas of Fermionic $^{23}Na^{40}K$ Molecules in Their Absolute Ground State”. In: *Physical Review Letters* 114.20 (May 18, 2015), p. 205302. DOI: 10.1103/PhysRevLett.114.205302 (cit. on p. 12).

[228] Jee Woo Park et al. “Second-Scale Nuclear Spin Coherence Time of Ultracold 23Na40K Molecules”. In: *Science* 357.6349 (July 2017), pp. 1–5. ISSN: 10959203. DOI: 10.1126/science.aal5066. pmid: 28751602 (cit. on p. 19).

[229] Juliana J. Park et al. “Spectrum of Feshbach Resonances in NaLi + Na Collisions”. In: *Physical Review X* 13.3 (Aug. 14, 2023), p. 031018. DOI: 10.1103/PhysRevX.13.031018 (cit. on p. 17).

[230] Maxwell F. Parsons et al. “Site-Resolved Imaging of Fermionic Li 6 in an Optical Lattice”. In: *Physical Review Letters* 114.21 (May 2015), p. 213002. ISSN: 10797114. DOI: 10.1103/PhysRevLett.114.213002. pmid: 26066433 (cit. on pp. 118, 146).

[231] David Peter et al. “Topological Bands with a Chern Number C = 2 by Dipolar Exchange Interactions”. In: *Physical Review A - Atomic, Molecular, and Optical Physics* 91.5 (May 2015), p. 53617. ISSN: 10941622. DOI: 10.1103/PhysRevA.91.053617 (cit. on p. 10).

[232] Gregory A. Phelps et al. *Sub-Second Production of a Quantum Degenerate Gas*. 2020. URL: http://arxiv.org/abs/2007.10807 (cit. on p. 69).

[233] William D. Phillips. "Nobel Lecture: Laser Cooling and Trapping of Neutral Atoms". In: *Reviews of Modern Physics* 70.3 (July 1, 1998), pp. 721–741. DOI: 10.1103/RevModPhys.70.721 (cit. on p. 1).

[234] Lewis R.B. Picard et al. "Deep Learning-Assisted Classification of Site-Resolved Quantum Gas Microscope Images". In: *Measurement Science and Technology* 31.2 (Nov. 2020), p. 025201. ISSN: 13616501. DOI: 10.1088/1361-6501/ab44d8 (cit. on pp. 126, 127).

[235] Philipp M. Preiss et al. "Quantum Gas Microscopy with Spin, Atom-Number, and Multilayer Readout". In: *Physical Review A - Atomic, Molecular, and Optical Physics* 91.4 (Apr. 2015), p. 041602. ISSN: 10941622. DOI: 10.1103/PhysRevA.91.041602 (cit. on p. 118).

[236] Philipp M. Preiss et al. "Strongly Correlated Quantum Walks in Optical Lattices". In: *Science* 347.6227 (Mar. 13, 2015), pp. 1229–1233. DOI: 10.1126/science.1260364 (cit. on p. 110).

[237] Adarsh P. Raghuram et al. "A Motorized Rotation Mount for the Switching of an Optical Beam Path in under 20 ms Using Polarization Control". In: *Review of Scientific Instruments* 94.6 (June 1, 2023), p. 063201. ISSN: 0034-6748. DOI: 10.1063/5.0139647 (cit. on pp. 21, 22, 48, 54).

[238] Apichayaporn Ratkata et al. "Measurement of the Tune-out Wavelength for ^{133}Cs at 880 nm". In: *Physical Review A* 104.5 (Nov. 22, 2021), p. 052813. DOI: 10.1103/PhysRevA.104.052813 (cit. on pp. 21–23, 73).

[239] Lukas Reichsöllner et al. "Quantum Engineering of a Low-Entropy Gas of Heteronuclear Bosonic Molecules in an Optical Lattice". In: *Physical Review Letters* 118.7 (Feb. 2017), pp. 1–10. ISSN: 10797114. DOI: 10.1103/PhysRevLett.118.073201. pmid: 28256882 (cit. on pp. 15, 72, 109, 141).

[240] Lukas K Reichsöllner. “A General Quantum-Engineering Technique for Efficient Production of Ultracold Dipolar Molecules”. PhD thesis. Leopold-Franzens-Universität Innsbruck, 2017. URL: https://diglib.uibk.ac.at/ulbtirolhs/download/pdf/2268740?originalFilename=true (cit. on pp. 14, 140).

[241] Helmut Ritsch et al. “Cold Atoms in Cavity-Generated Dynamical Optical Potentials”. In: *Reviews of Modern Physics* 85.2 (Apr. 2, 2013), pp. 553–601. DOI: 10.1103/RevModPhys.85.553 (cit. on p. 3).

[242] Jacob Lyman Roberts. “The First Experiments with 85Rb BECs”. PhD thesis. University of Colorado, 2001 (cit. on p. 29).

[243] Jason S. Rosenberg et al. “Observation of the Hanbury Brown–Twiss Effect with Ultracold Molecules”. In: *Nature Physics* 18.9 (9 Sept. 2022), pp. 1062–1066. ISSN: 1745-2481. DOI: 10.1038/s41567-022-01695-9 (cit. on pp. 18, 111, 131, 148).

[244] Tanya S. Roussy et al. “An Improved Bound on the Electron’s Electric Dipole Moment”. In: *Science* 381.6653 (July 7, 2023), pp. 46–50. DOI: 10.1126/science.adg4084 (cit. on p. 4).

[245] Richard Roy et al. “Rapid Cooling to Quantum Degeneracy in Dynamically Shaped Atom Traps”. In: *Physical Review A* 93.4 (Apr. 4, 2016), p. 043403. ISSN: 2469-9926, 2469-9934. DOI: 10.1103/PhysRevA.93.043403 (cit. on p. 69).

[246] Richard J Roy. “Ytterbium and Lithium Quantum Gases: Heteronuclear Molecules and Bose-Fermi Superfluid Mixtures”. PhD thesis. University of Washington, 2017 (cit. on p. 68).

[247] Daniel K. Ruttley et al. “Formation of Ultracold Molecules by Merging Optical Tweezers”. In: *Physical Review Letters* 130.22 (May 31, 2023), p. 223401. DOI: 10.1103/PhysRevLett.130.223401 (cit. on p. 15).

[248] Timur M. Rvachov et al. “Long-Lived Ultracold Molecules with Electric and Magnetic Dipole Moments”. In: *Physical Review Letters* 119.14 (Oct. 2, 2017), p. 143001. DOI: 10.1103/PhysRevLett.119.143001 (cit. on p. 12).

[249] S. Sachdev. *Quantum Phase Transitions*. Cambridge University Press, 2011. ISBN: 978-0-511-97376-5 (cit. on pp. 93, 103).

[250] Subir Sachdev. "Boson Hubbard Model". In: *Quantum Phase Transitions*. 2011, pp. 117–132. ISBN: 9780511973765 (cit. on p. 94).

[251] A. Safavi-Naini, M. L. Wall, and A. M. Rey. "Role of Interspecies Interactions in the Preparation of a Low-Entropy Gas of Polar Molecules in a Lattice". In: *Physical Review A - Atomic, Molecular, and Optical Physics* 92.6 (2015). ISSN: 10941622. DOI: 10.1103/PhysRevA.92.063416 (cit. on p. 14).

[252] M. S. Safronova et al. "Search for New Physics with Atoms and Molecules". In: *Reviews of Modern Physics* 90.2 (June 29, 2018), p. 025008. DOI: 10.1103/RevModPhys.90.025008 (cit. on p. 4).

[253] J. E. Sansonetti. "Wavelengths, Transition Probabilities, and Energy Levels for the Spectra of Cesium (CsI–CsLV)". In: *Journal of Physical and Chemical Reference Data* 38.4 (Oct. 29, 2009), pp. 761–923. ISSN: 0047-2689. DOI: 10.1063/1.3132702 (cit. on p. 76).

[254] Martin Santiago Miranda. "Quantum Gas Microscope for Ytterbium Atoms". PhD thesis. Tokyo Institute of Technology, 2016. URL: http://www.kozuma.phys.titech.ac.jp/miranda_thesis.pdf (cit. on p. 54).

[255] Simon Saunders. "On the Explanation for Quantum Statistics". In: *Studies in History and Philosophy of Science Part B: Studies in History and Philosophy of Modern Physics* 37.1 (2006), pp. 192–211. DOI: 10.1016/j.shpsb.2005.11.002 (cit. on p. 63).

[256] T. A. Savard, K. M. O'Hara, and J. E. Thomas. *Laser-Noise-Induced Heating in Far-off Resonance Optical Traps*. 2. 1997, R1095–R1098. DOI: 10.1103/PhysRevA.56.R1095 (cit. on p. 50).

[257] Peter Schauß. "High-Resolution Imaging of Ordering in Rydberg Many-Body Systems". PhD thesis. LMU, 2015. 1–214 (cit. on p. 90).

[258] Andreas Schindewolf. “Quantum Engineering of a Low-Entropy Sample of RbCs Molecules in an Optical Lattice”. PhD thesis. University of Innsbruck. URL: https://diglib.uibk.ac.at/ulbtirolhs/download/pdf/2880207?originalFilename=true (cit. on p. 109).

[259] Andreas Schindewolf et al. “Evaporation of Microwave-Shielded Polar Molecules to Quantum Degeneracy”. In: *Nature* 607.7920 (7920 July 2022), pp. 677–681. ISSN: 1476-4687. DOI: 10.1038/s41586-022-04900-0 (cit. on pp. 17, 70).

[260] Stefan Schmid et al. “Long Distance Transport of Ultracold Atoms Using a 1D Optical Lattice”. In: *New Journal of Physics* 8 (2006). ISSN: 13672630. DOI: 10.1088/1367-2630/8/8/159 (cit. on pp. 41, 43, 48).

[261] Ulrich Schneider. “Interacting Fermionic Atoms in Optical Lattices - A Quantum Simulator for Condensed Matter Physics”. PhD thesis. Johannes Gutenberg-Universität Mainz, 2011. DOI: 10.25358/OPENSCIENCE-3169 (cit. on p. 84).

[262] D. Schrader et al. “An Optical Conveyor Belt for Single Neutral Atoms”. In: *Applied Physics B* 73.8 (Dec. 1, 2001), pp. 819–824. ISSN: 1432-0649. DOI: 10.1007/s003400100722 (cit. on p. 56).

[263] Frauke Seeßelberg et al. “Extending Rotational Coherence of Interacting Polar Molecules in a Spin-Decoupled Magic Trap”. In: *Physical Review Letters* 121.25 (Dec. 19, 2018), p. 253401. DOI: 10.1103/PhysRevLett.121.253401 (cit. on p. 19).

[264] Adam L. Shaw et al. *Benchmarking Highly Entangled States on a 60-Atom Analog Quantum Simulator*. Aug. 15, 2023. arXiv: 2308.07914 [physics, physics:quant-ph]. URL: http://arxiv.org/abs/2308.07914. preprint (cit. on p. 8).

[265] Jacob F. Sherson et al. “Single-Atom-Resolved Fluorescence Imaging of an Atomic Mott Insulator”. In: *Nature* 467.7311 (Sept. 2010), pp. 68–72. ISSN: 00280836. DOI: 10.1038/nature09378 (cit. on pp. 2, 96, 102, 110, 112–114, 145).

[266] M. D. Shotter. “Large-Photon-Number Extraction from Individual Atoms Trapped in an Optical Lattice”. In: *Physical Review A* 83.3 (Mar. 25, 2011), p. 033420. DOI: 10.1103/PhysRevA.83.033420 (cit. on p. 133).

[267] Jonathan Simon et al. “Quantum Simulation of Antiferromagnetic Spin Chains in an Optical Lattice”. In: *Nature* 472.7343 (Apr. 2011), pp. 307–312. ISSN: 00280836. DOI: 10.1038/nature09994 (cit. on p. 110).

[268] C. Simonelli et al. “Realization of a High Power Optical Trapping Setup Free from Thermal Lensing Effects”. In: *Optics Express* 27.19 (Apr. 2019), p. 27215. ISSN: 1094-4087. DOI: 10.1364/oe.27.027215. pmid: 31674587 (cit. on p. 54).

[269] R. G. Smith. “Optical Power Handling Capacity of Low Loss Optical Fibers as Determined by Stimulated Raman and Brillouin Scattering”. In: *Applied Optics* 11.11 (Nov. 1972), p. 2489. ISSN: 0003-6935. DOI: 10.1364/ao.11.002489 (cit. on p. 99).

[270] J. Söding et al. “Giant Spin Relaxation of an Ultracold Cesium Gas”. In: *Physical Review Letters* 80.9 (Mar. 2, 1998), pp. 1869–1872. DOI: 10.1103/PhysRevLett.80.1869 (cit. on p. 70).

[271] J. Söding et al. “Three-Body Decay of a Rubidium Bose–Einstein Condensate”. In: *Applied Physics B* 69.4 (Oct. 1, 1999), pp. 257–261. ISSN: 1432-0649. DOI: 10.1007/s003400050805 (cit. on pp. 71, 80).

[272] Maximilian Sohmen et al. *A Ship-in-a-Bottle Quantum Gas Microscope for Magnetic Mixtures*. June 8, 2023. DOI: 10.48550/arXiv.2306.05404. arXiv: 2306.05404 [cond-mat]. preprint (cit. on p. 115).

[273] Stefan Spence. “Assembling Single RbCs Molecules with Optical Tweezers [Dataset]”. PhD thesis. Durham University, 2022, p. 61197618. URL: http://collections.durham.ac.uk/files/r2xs55mc11s (cit. on p. 27).

[274] D. M. Stamper-Kurn et al. “Reversible Formation of a Bose-Einstein Condensate”. In: *Physical Review Letters* 81.11 (Sept. 1998), pp. 2194–2197. ISSN: 10797114. DOI: 10.1103/PhysRevLett.81.2194 (cit. on pp. 65, 69).

[275] Ian Stevenson et al. “Ultracold Gas of Dipolar NaCs Ground State Molecules”. In: *Physical Review Letters* 130.11 (Mar. 16, 2023), p. 113002. DOI: 10.1103/PhysRevLett.130.113002 (cit. on p. 12).

[276] Kevin E. Strecker et al. “Formation and Propagation of Matter-Wave Soliton Trains”. In: *Nature* 417.6885 (6885 May 2002), pp. 150–153. ISSN: 1476-4687. DOI: 10.1038/nature747 (cit. on p. 2).

[277] Lin Su et al. *Dipolar Quantum Solids Emerging in a Hubbard Quantum Simulator*. June 1, 2023. arXiv: 2306.00888 [cond-mat]. URL: http://arxiv.org/abs/2306.00888. preprint (cit. on pp. 9, 11, 113, 115, 118, 148).

[278] Bhuvanesh Sundar, Bryce Gadway, and Kaden R.A. Hazzard. “Synthetic Dimensions in Ultracold Polar Molecules”. In: *Scientific Reports* 8.1 (Dec. 2018), pp. 1–7. ISSN: 20452322. DOI: 10.1038/s41598-018-21699-x. pmid: 29467482 (cit. on p. 10).

[279] Sergey V. Syzranov et al. “Spin-Orbital Dynamics in a System of Polar Molecules”. In: *Nature Communications* 5 (2014). ISSN: 20411723. DOI: 10.1038/ncomms6391 (cit. on p. 10).

[280] Tetsu Takekoshi et al. “Ultracold Dense Samples of Dipolar RbCs Molecules in the Rovibrational and Hyperfine Ground State”. In: *Physical Review Letters* 113.20 (Nov. 12, 2014), p. 205301. DOI: 10.1103/PhysRevLett.113.205301 (cit. on pp. 12, 15).

[281] Naaman Tammuz et al. “Can a Bose Gas Be Saturated?” In: *Physical Review Letters* 106.23 (June 6, 2011), p. 230401. ISSN: 0031-9007, 1079-7114. DOI: 10.1103/PhysRevLett.106.230401. arXiv: 1103.2896 [cond-mat, physics:physics, physics:quant-ph] (cit. on p. 64).

[282] L. Tanzi et al. “Observation of a Dipolar Quantum Gas with Metastable Supersolid Properties”. In: *Physical Review Letters* 122.13 (Apr. 3, 2019), p. 130405. DOI: 10.1103/PhysRevLett.122.130405 (cit. on p. 13).

[283] Steven J . Thomson. “The Effects of Disorder in Strongly Interacting Quantum Systems”. PhD thesis. University of St Andrews, 2016 (cit. on p. 94).

[284] Tobias G. Tiecke. “Feshbach Resonances in Ultracold Mixtures of the Fermionic Quantum Gases 6Li and 40K”. Dec. 15, 2009. URL: https://pure.uva.nl/ws/files/748585/71425_thesis.pdf (cit. on p. 43).

[285] Jan Trautmann. “The Magnetic Quadrupole Transition in Neutral Strontium”. PhD thesis. Ludwig-Maximilians-Universität München, 2022 (cit. on p. 46).

[286] Jonathan Trisnadi et al. “Design and Construction of a Quantum Matter Synthesizer”. In: *Review of Scientific Instruments* 93.8 (Aug. 24, 2022), p. 083203. ISSN: 0034-6748. DOI: 10.1063/5.0100088 (cit. on pp. 2, 41, 144, 148).

[287] Matthias Troyer and Uwe-Jens Wiese. “Computational Complexity and Fundamental Limitations to Fermionic Quantum Monte Carlo Simulations”. In: *Physical Review Letters* 94.17 (May 4, 2005), p. 170201. DOI: 10.1103/PhysRevLett.94.170201 (cit. on p. 8).

[288] G. Unnikrishnan et al. “Long Distance Optical Transport of Ultracold Atoms: A Compact Setup Using a Moiré Lens”. In: *Review of Scientific Instruments* 92.6 (Mar. 2021), p. 063205. ISSN: 10897623. DOI: 10.1063/5.0049320. pmid: 34243520 (cit. on p. 43).

[289] Alban Urvoy et al. “Direct Laser Cooling to Bose-Einstein Condensation in a Dipole Trap”. In: *Physical Review Letters* 122.20 (May 24, 2019), p. 203202. DOI: 10.1103/PhysRevLett.122.203202 (cit. on p. 66).

[290] Giacomo Valtolina et al. “Dipolar Evaporation of Reactive Molecules to below the Fermi Temperature”. In: *Nature* 588.7837 (July 2020), pp. 239–243. ISSN: 14764687. DOI: 10.1038/s41586-020-2980-7. pmid: 33299192 (cit. on pp. 17, 70).

[291] Stéfan Van Der Walt et al. “Scikit-Image: Image Processing in Python”. In: *PeerJ* 2014.1 (June 2014), pp. 1–18. ISSN: 21678359. DOI: 10.7717/peerj.453 (cit. on pp. 123, 126).

[292] Guifré Vidal. “Efficient Simulation of One-Dimensional Quantum Many-Body Systems”. In: *Physical Review Letters* 93.4 (July 19, 2004), p. 040502. DOI: 10.1103/PhysRevLett.93.040502 (cit. on p. 8).

[293] Konrad Viebahn. “Quasicrystalline Optical Lattices for Ultracold Atoms”. PhD thesis. University of Cambridge, 2018 (cit. on p. 84).

[294] Konrad Viebahn et al. “Matter-Wave Diffraction from a Quasicrystalline Optical Lattice”. In: *Physical Review Letters* 122.11 (July 2019), pp. 1–10. ISSN: 10797114. DOI: 10.1103/PhysRevLett.122.110404. pmid: 30951352 (cit. on p. 102).

[295] Nathaniel B. Vilas et al. “Magneto-Optical Trapping and Sub-Doppler Cooling of a Polyatomic Molecule”. In: *Nature* 606.7912 (7912 June 2022), pp. 70–74. ISSN: 1476-4687. DOI: 10.1038/s41586-022-04620-5 (cit. on p. 12).

[296] J. L. Ville et al. “Loading and Compression of a Single Two-Dimensional Bose Gas in an Optical Accordion”. In: *Physical Review A* 95.1 (Jan. 27, 2017), p. 013632. ISSN: 2469-9926, 2469-9934. DOI: 10.1103/PhysRevA.95.013632 (cit. on p. 116).

[297] Kai K. Voges et al. “Ultracold Gas of Bosonic $^{23}Na^{39}K$ Ground-State Molecules”. In: *Physical Review Letters* 125.8 (Aug. 21, 2020), p. 083401. DOI: 10.1103/PhysRevLett.125.083401 (cit. on p. 12).

[298] Hendrik Paul Carsten von Raven. “A new Caesium quantum gas microscope with precise magnetic field control”. PhD thesis. Ludwig-Maximilians-Universität München, 2022 (cit. on p. 82).

[299] Vladan Vuletic et al. “Degenerate Raman Sideband Cooling of Trapped Cesium Atoms at Very High Atomic Densities”. In: *Physical Review Letters* 81.26 (Dec. 1998), pp. 5768–5771. ISSN: 10797114. DOI: 10.1103/PhysRevLett.81.5768 (cit. on p. 24).

[300] Kenneth Wang et al. “Enriching the Quantum Toolbox of Ultracold Molecules with Rydberg Atoms”. In: *PRX Quantum* 3.3 (Sept. 16, 2022), p. 030339. DOI: 10.1103/PRXQuantum.3.030339 (cit. on p. 18).

[301] Tino Weber et al. “Bose-Einstein Condensation of Cesium”. In: *Science* 299.5604 (Jan. 2003), pp. 232–235. ISSN: 00368075. DOI: 10.1126/science.1079699. pmid: 12471267 (cit. on pp. 13, 39, 69, 73, 79).

[302] G. L. Weissler and R. W. Carlson. *Vacuum Physics and Technology*. Methods of Experimental Physics ; v. 14. New York ; Academic Press, 1979. 619 pp. ISBN: 978-1-282-28745-7 (cit. on p. 26).

[303] Christoph Weitenberg. "Single-Atom Resolved Imaging and Manipulation in an Atomic Mott Insulator". PhD thesis. Ludwig-Maximilians-Universität München, 2011. URL: papers : / / fe3c0465 - e0d0 - 4e90 - a74d - 7e674c71995a/Paper/p5181 (cit. on pp. 43, 101, 116, 117, 123, 125, 128, 133, 134).

[304] Julian F. Wienand et al. *Emergence of Fluctuating Hydrodynamics in Chaotic Quantum Systems*. June 20, 2023. arXiv: 2306.11457 [cond-mat, physics:quant-ph]. URL: http://arxiv.org/abs/2306.11457. preprint (cit. on p. 113).

[305] Sebastian Will. "Interacting Bosons and Fermions in Three-Dimensional Optical Lattice Potentials". PhD thesis. LMU, 2011 (cit. on pp. 87, 89, 97, 104).

[306] Ryuta Yamamoto. "A Quantum Gas Microscope of Two-electron Atoms with Fluorescence and Faraday Imaging". PhD thesis. Kyoto, 2016. DOI: https://japanlinkcenter.org/jalc/linkSakiAnnaiOto/mRRidirect/index?doi=10.14989/doctor.k20044 (cit. on pp. 117, 146).

[307] Ryuta Yamamoto et al. "Single-Site-Resolved Imaging of Ultracold Atoms in a Triangular Optical Lattice". In: *New Journal of Physics* 22.12 (Oct. 2020). ISSN: 13672630. DOI: 10.1088/1367-2630/abcdc8 (cit. on pp. 113, 147).

[308] Bo Yan et al. "Observation of Dipolar Spin-Exchange Interactions with Lattice-Confined Polar Molecules". In: *Nature* 501.7468 (7468 Sept. 2013), pp. 521–525. ISSN: 1476-4687. DOI: 10.1038/nature12483 (cit. on p. 18).

[309] Zoe Z. Yan et al. "Resonant Dipolar Collisions of Ultracold Molecules Induced by Microwave Dressing". In: *Physical Review Letters* 125.6 (Aug. 2020), p. 063401. ISSN: 10797114. DOI: 10.1103/PhysRevLett.125.063401. pmid: 32845680 (cit. on p. 17).

[310] Zoe Z. Yan et al. “Two-Dimensional Programmable Tweezer Arrays of Fermions”. In: *Physical Review Letters* 129.12 (Sept. 14, 2022), p. 123201. DOI: 10.1103/PhysRevLett.129.123201 (cit. on p. 2).

[311] C. N. Yang. “Concept of Off-Diagonal Long-Range Order and the Quantum Phases of Liquid He and of Superconductors”. In: *Reviews of Modern Physics* 34.4 (Oct. 1, 1962), pp. 694–704. DOI: 10.1103/RevModPhys.34.694 (cit. on pp. 93, 104).

[312] Huan Yang et al. “Creation of an Ultracold Gas of Triatomic Molecules from an Atom–Diatomic Molecule Mixture”. In: *Science* 378.6623 (Dec. 2, 2022), pp. 1009–1013. DOI: 10.1126/science.ade6307 (cit. on p. 17).

[313] Huan Yang et al. “Observation of Magnetically Tunable Feshbach Resonances in Ultracold 23 Na 40 K + 40 K Collisions”. In: *Science* 363.6424 (2019), pp. 261–264. ISSN: 10959203. DOI: 10.1126/science.aau5322. pmid: 30655438 (cit. on p. 17).

[314] Jin Yang et al. “Site-Resolved Imaging of Ultracold Fermions in a Triangular-Lattice Quantum Gas Microscope”. In: *PRX Quantum* 2.2 (June 21, 2021), p. 020344. DOI: 10.1103/PRXQuantum.2.020344 (cit. on pp. 113, 147).

[315] N. Y. Yao et al. “Many-Body Localization in Dipolar Systems”. In: *Physical Review Letters* 113.24 (Dec. 11, 2014), p. 243002. DOI: 10.1103/PhysRevLett.113.243002 (cit. on p. 10).

[316] Aaron W. Young et al. “Tweezer-Programmable 2D Quantum Walks in a Hubbard-regime Lattice”. In: *Science* 377.6608 (Aug. 19, 2022), pp. 885–889. DOI: 10.1126/science.abo0608 (cit. on pp. 2, 144, 149).

[317] T. Zelevinsky, S. Kotochigova, and Jun Ye. “Precision Test of Mass-Ratio Variations with Lattice-Confined Ultracold Molecules”. In: *Physical Review Letters* 100.4 (Jan. 29, 2008), p. 043201. DOI: 10.1103/PhysRevLett.100.043201 (cit. on p. 5).

[318] Chi Zhang and M. R. Tarbutt. “Quantum Computation in a Hybrid Array of Molecules and Rydberg Atoms”. In: *PRX Quantum* 3.3 (2022), p. 030340 (cit. on p. 18).

[319] Grace H. Zhang et al. “Note: Fast Compact Laser Shutter Using a Direct Current Motor and Three-Dimensional Printing”. In: *Review of Scientific Instruments* 86.12 (Dec. 14, 2015), p. 126105. ISSN: 0034-6748. DOI: 10.1063/1.4937614 (cit. on p. 37).

[320] Jessie T. Zhang et al. “An Optical Tweezer Array of Ground-State Polar Molecules”. In: *Quantum Science and Technology* 7.3 (May 2022), p. 035006. ISSN: 2058-9565. DOI: 10.1088/2058-9565/ac676c (cit. on p. 18).

[321] Wilhelm Zwerger. “Mott–Hubbard Transition of Cold Atoms in Optical Lattices”. In: *Journal of Optics B: Quantum and Semiclassical Optics* 5.2 (Apr. 2003), S9. ISSN: 1464-4266. DOI: 10.1088/1464-4266/5/2/352 (cit. on p. 92).